Identification, Compensation and Estimation of Joint Friction of Robotic Manipulators

岩谷, 正義

https://doi.org/10.15017/1807023

Identification, Compensation and Estimation of Joint Friction of Robotic Manipulators

by

Masayoshi Iwatani

Acknowledgements

Firstly, I would like to thank my supervisor, Dr. Ryo Kikuuwe, for his advices, instructions and patience. Without his devotion of huge amount of effort and time, writing my dissertation cannot be completed. Furthermore, his words have encouraged me and have provided me new viewpoints about research and work, which must help me to survive the future of life.

I also would like to sincerely thank Dr. Motoji Yamamoto for his support in my research work. His guidelines, advices and encouragements have helped my research work.

I also would like to thank Dr. Takahiro Kondou and Dr. Ryo Kurazume, who are the members of my dissertation supervisory committee, for their review and comments for this dissertation.

I wish to express my thanks to Dr. Svinin Mikhail, Dr. Kenji Tahara, Dr. Takeshi Ikeda and Dr. Yasutaka Nakashima for their suggestions and comments, which have been great support in academic and personal life.

I want to thank previous Ph.D. students of Control Engineering, Dr. Shanhai Jin, Dr. Xiaogang Xiong and Dr. Aung Myo Than Sin for their advises and constructive discussions especially about friction, noise reduction filters and force control schemes.

Special thanks go to Mr. Kouki Shinya for his contributions in developing experimental setups we have used and in maintenance of laboratory's safety and cleanliness.

Throughout my laboratory life, I have been helped by many laboratory members. I would like to thank Ms. Midori Tateyama, Ms. Ayako Kashiwagi and Ms. Mizuho Nagatomi for their kind help in various forms. I am also grateful to all previous and current student members, especially Dr. Yuki Matsutani, Dr. Aung Myo Thant Sin, Dr. Noriyasu Iwamoto, Dr. Akihiro Morinaga, Mr. Seunghyun Choi, Mr. Gyuho Byun, Mr. Masahiro Kadosaki,

Mr. Soichiro Kanda, Mr. Yang Bai, Mr. Yuuki Nozawa, Mr. Tomofumi Watari, who have been helpful and encouraging in my laboratory life.

Finally, I am deeply thankful to my family for their moral and financial support throughout my Ph.D. research.

Contents

List of figures

List of tables

Chapter 1

Introduction

1.1 Joint Friction in Robotic Systems

Friction is a common phenomenon that occurs between contacting objects. In particular, in robotic systems, friction takes place between contacting components, for example, teeth in gear boxes, bearings, ball screws. Friction hampers the relative motion and it is generally problematic. Joint friction in robotic systems degrades the accuracy of control and deteriorates the backdrivability. In position control systems, joint friction causes large tracking error, which may result in low frequency oscillation such as the stick-slip phenomenon and the limit cycles. In force control systems, joint friction leads to the error between the desired force and the actual force.

In order to mitigate problems mentioned above, it is required to estimate and compensate the joint friction, i.e., calculate the magnitude of the friction and cancel the friction by generating the actuator force. For these purposes, the first important thing is modeling and identification of the friction, i.e., to investigate the properties of the friction phenomena and represent them by appropriate equations. Friction is usually represented by a function of which the output is determined uniquely with respect to the input velocity. In the neighborhood of zero-velocity, however, we can observe many friction properties that cannot be modeled by such a function. Therefore, more developed models are needed. Identification is also not always easy problem. Because the relation between the motion and the force

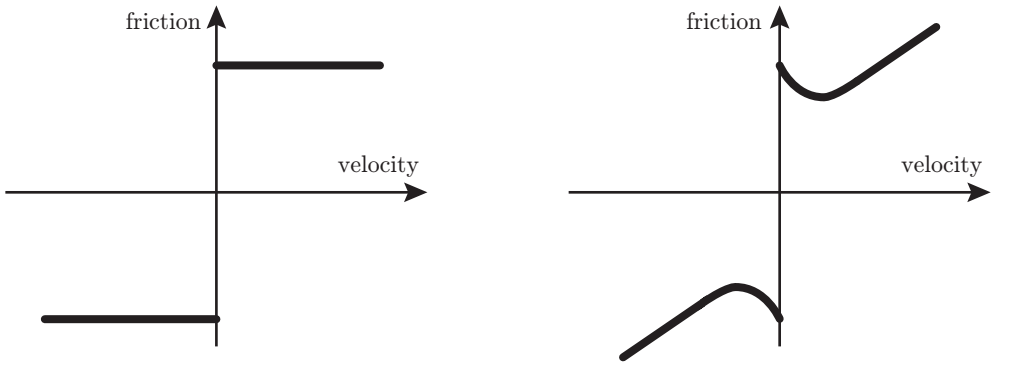

(a) Coulomb friction

(b) Coulomb friction with viscous friction and Stribeck effect

Figure 1.1: Friction model represented by a function of which the output is determined uniquely with respect to the input velocity.

is affected by complicated factors such as inertia, Coriolis, centrifugal, gravity and friction forces, it is difficult to extract only the relation between the motion and the friction force. Moreover in the case of assembled robots, the motion is limited by the joints' mechanical limitation or the environment.

Even when we obtain an appropriate friction model, friction compensation is not still trivial problem, because we may not be able to estimate the friction state due to the limitation of the hardware such as the low resolution of the position sensors. There is possibility that the friction compensation based on the friction model is not sufficient, so a compensator that softens this problem is required.

One application of friction force estimation is external force estimation in which external force on a robot is estimated based on the equation of motion including a friction term. In this scheme, the accuracy of the external force estimation depends on the accuracy of the friction force estimation. Admittance control, which is one of force control schemes, is a further application of the friction (and external) force estimation.

1.2 Modeling of Friction

Many friction models have been proposed so far. One of simplest friction models is Coulomb friction model [8, 31], which is usually represented by a function of which the output is de-

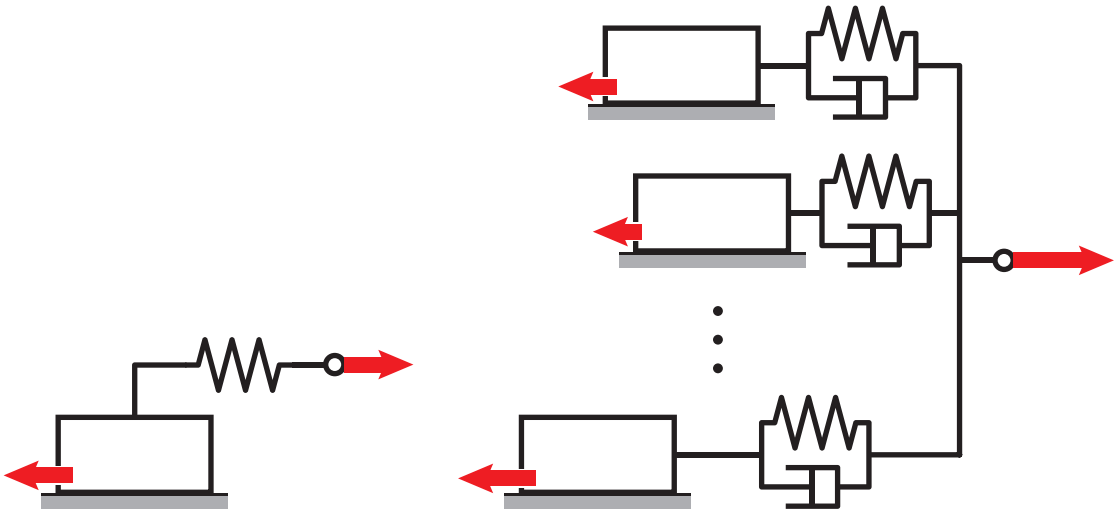

(a) Elastoplastic friction model

(b) Parallel connection of friction element with spring and damper

Figure 1.2: Friction models containing presliding property.

termined uniquely with respect to the input velocity as Figure 1.1(a). This model has been combined with viscous friction, which increases with increasing velocity, and Stribeck effect, which is friction property where the friction force decreases with increasing velocity. These models capture the properties in the kinetic friction region well, but they cannot capture properties in the static friction region, which is the neighborhood of zero-velocity where the models have the discontinuity.

Motivated by observation of small elastic displacement even in the static friction region, Dahl [16] has proposed a friction model that is schematically illustrated as Figure 1.2(a). This model is a serial connection of a Coulomb friction element and an elastic component that corresponds to the elasticity of the contacting objects. The observed 'presliding displacement' is interpreted as the displacement by the elongation of the elastic element. At this time, the Coulomb friction element is stuck, so this region is called presliding region. On the other hand, the region where the friction element is slipping is called sliding region. Dahl has formulated this friction model by differential equations, and thus it can be regarded as 'dynamic' friction model.

After Dahl model, many dynamic friction models have been proposed. Canudas de Wit

et al. [10] have proposed LuGre model, which is a friction model that combines the Stribeck effect with Dahl model. This model captures friction phenomena such as stick-slip motion, friction lag and varying break-away force. Swevers et al. [87] have presented Leuven model, which is an extension of LuGre model and has an arbitrary function for representing hysteresis in the presliding region. Leuven model has been modified by Lampaert et al. [57] where the hysteresis function is implemented by a parallel connection of friction elements [26,36,45]. This formulation of friction is organized by Al-Bender et al. [1,58], and is named the Generalized Maxwell Slip (GMS) model, which is illustrated as Figure 1.2(b). The GMS model is one of the most famous friction models for its ability to capture many friction phenomena. Boegli et al. [6,7] have improved the GMS model by smoothening the behavior of the model.

Other researchers also have been inspired by Dahl model. Hayward and Armstrong [32] have proposed an elastoplastic friction model that is composed of a Coulomb friction element and an elastic element. The discretized algorithm of this model is derived by the geometric relation of the input position and the friction element's position. Dupont et al. [21] have proposed a single state elastoplastic friction model with refined static friction behavior. Kikuuwe et al. [55] have considered the discrete time representation of an elastoplastic friction model, and they [56] have proposed discrete-time algorithms of visco-elastoplastic friction model, which is a generalization of Hayward and Armstrong's elastoplastic friction model with non-zero viscosity. This discretization is an approximation of continuous-time representation of differential inclusion (i.e., differential equation including discontinuity) based on the backward Euler method. Xiong et al. [97] have derived a continuous differential equation of visco-elastoplastic friction model from the original differential inclusion. Xiong et al. [96] also have extended the single-state friction model to a multi-state one. Advantages of models of Kikuuwe et al. [55, 56] and Xiong et al. [96, 97] are the continuous output friction force by excluding any discontinuous part.

1.3 Identification of Joint Friction

1.3.1 Sliding region and presliding region

In order to deal with joint friction in mechanical systems, it is necessary to identify the property and the magnitude of the friction. As mentioned above, friction phenomena have been formulated in the both of the sliding region and the presliding region by functions of which the output is determined uniquely with respect to the input or differential equations, and thus an identification method appropriate to each regime is necessary.

The relation between velocity and friction in sliding region is one of most remarkable properties from the viewpoint of control. Canudas de Wit and Lischinsky [9] have obtained velocity-friction curve of joints of a robot by observing the signal of the velocity and the actuator torque through tests commanding constant velocities, which has been used by other researchers [24, 34, 50]. Other schemes are based on sinusoidal [51] or saw-teeth [94] form force input. When methods mentioned above are applied to an assembled robot, there is possibility that the motion of the robot reaches the limitation by the configuration or environment, so we must consider the motion trajectory explicitly.

Identifying manipulator's parameters such as inertia, gravity and friction simultaneously is an interesting challenge for its potential to reduce the required time. Gautier et al. [67, 68, 83] have proposed identification methods based on an inverse dynamic model and least square regression. In such methods, the equation of motion of a manipulator is linearized with respect to the vector that contains the dynamical parameters, and the parameters are identified by solving the linearized equation of which the components come from experimental data. In order to achieve efficient and successful identification, the parameters to be identified is reduced by eliminating parameters that have no effect on the dynamic model and by regrouping the parameters [25], and the trajectory of robot has been considered to excite the properties such as inertia, gravity and friction [67, 68, 95]. Because these methods usually are targeted to many parameters, the formulation of friction term must be simple for low computational cost, which sacrifices the versatility of friction identification.

For further precise control, modeling and identification of joint friction in presliding region is required. Canudas de Wit and Lischinsky [9] have identified nominal parameters

(stiffness and viscosity in presliding region) of LuGre model for a DC motor mechanism using a numerical optimization method based on the system model, and applied it to adaptive friction estimation and compensation. Rizos and Fassois [77, 78] have identified presliding friction of an actuator system based on Maxwell Slip model, i.e. a parallel connection of elastoplastic elements, by means of inverse dynamic model and least square regression. A similar method has been used for a harmonic drive transmission [89]. Iwatani et al. [42] have identified elastic coefficients of parallel visco-elastoplastic friction model for manipulator joints in which harmonic drives are embedded by physical interpretation between the model and experimental data. Because the frictional behavior is different between in the sliding region and in the presliding region, the identification also should be performed separately by appropriate ways for such regions.

1.3.2 On-line method

As with the identification methods mentioned above, friction identification should be accomplished in advance in a basic sense. In the field of control, however, the identification is sometimes performed on-line, i.e., at the same time as a robot is doing its tasks, where the parameters are adjusted by adaptive methods. Canudas de Wit and Lischinsky [9] have proposed an adaptive friction estimation method based on nominal LuGre model with an additional parameter adjusting the output friction force. Tan and Kanellakopoulos [88] have extended Canudas de Wit and Lischinsky's method [9] using multiple adaptive parameters. Grami and Aissaoui [27] have proposed an on-line identification method for parameters of the GMS model. Ljung [63] have proposed a method to estimate parameters of a system on-line by recursive least square algorithm. Ruderman [79] have found a parameter set of friction of robotic joints based on the recursive least square method with the initial parameter set is determined in advance by a least square method.

Although adaptive methods have ability in adjustment, the accuracy of parameters identified in advance is still important, because the initial parameters may be set as the pre-identified one.

1.4 Compensation of Joint Friction

Joint friction in robotic systems deteriorates the performance of the control. One straightforward way to deal with such problem is friction compensation, i.e., making the effect of the friction smaller by generating the actuator force canceling the friction force.

A conventional proportional-integral-differential (PID) position controller has ability to suppress the effect of the friction with high stiffness by high gains. In unstructured environment such as human workspace, however, high stiffness position control is not preferable because a system that includes such a controller does not have compliance and causes injury when it collides with human. Other control methods suppressing the effect of the friction have been proposed such as nonlinear PID position controllers [2, 80, 82] or sliding mode controllers [46, 85, 92, 93]. Such methods assume the desired position. It means that the controllers are connected with the controlled objects strongly and lack universal use.

The methodology of friction compensation on which this dissertation focuses is different from that of the controllers mentioned above. Friction compensation based on a friction model is advantageous because it does not need any desired value. Moreover, it has potential possibility to make joints free from friction. Such compensators are easy to superpose on any other controllers, and for situations where joint friction hampers the control, the compensators break through problems. This dissertation focuses on the advantage of the friction compensation based on a friction model.

1.4.1 Model-based compensation

In model-based friction compensation schemes, force estimated by a friction model is generated by the actuator to cancel the friction force. Coulomb friction model with viscous friction and Stribeck effect has been used for compensation of friction in the sliding region [50, 84]. For compensating friction in presliding region for robotic joints, LuGre model has been utilized [9, 23, 35, 74]. Tjahjowidodo et al. [90, 91] have utilized the GMS model for friction compensation control of a belt-driven DC motor system. Mahvash and Okamura [66] have used Hayward and Armstrong's [32] elastoplastic friction model for friction compensation of tendon-driven joints. Iwatani et al. [42] have used a model composed of

parallel connection of Kikuuwe et al.'s [56] visco-elastoplastic friction model for friction compensation of harmonic drive gearings.

Some researchers have combined model-based friction compensation methods with other methods. Lee and Tomizuka [60] have proposed a friction compensation method based on Coulomb friction model and a disturbance observer for a position control system. Canudas de Wit et al. [9] have presented an adaptive friction compensation method based on LuGre model for variation of friction of a position-controlled robotic system. In this method, the magnitude of the compensation force varies according to the position error. Lampaert et al. [59] have combined the GMS model and a disturbance observer using Kalman filter. Choi et al. [14] have developed a combination of a sliding mode controller and an extended LuGre model improved for pre-sliding hysteresis property. Maeda et al. [64, 65] enhances initial response of a disturbance observer by including bang-bang control or friction model-based compensation. Jamaludin et al. [43, 44] have combined a feed forward friction compensator based on the GMS model and a disturbance observer for control of a linear-drive feed table. Zschäck et al. [101] have proposed a friction compensation method based on GMS model adaptive for position-dependent friction.

1.4.2 Dither

For robotic joints with friction, some researchers [4, 29, 75] have focused on effectiveness of dither, i.e. high frequency oscillatory force by actuators. Dither is originally intended to improves the system smoothness by making the system in the kinetic friction state, where it is assumed that the friction force is smaller than in the static friction state. Stolt et al. [86] have used dither for improving performance of external force estimation of a manipulator. For robotic joints with high presliding stiffness, Aung et al. [5] have proposed a new dither friction compensator, which is intended to make the system on the verge of the static friction state and sensitive to applied force. Aung et al. [5] have combined the dither and model-based friction compensation, and this method has successfully compensated the friction in the presliding region, where only model-based method cannot compensate. Impulsive control [3] is a similar method where small impulsive force is repetitively applied to the system to produce positional modification in micro scale.

1.5 Estimation of Joint Friction Force

Estimating joint friction force, not compensating the friction, is also important. Friction force estimation requires only position sensors such as encoders, and in some scenes, only estimation of friction is sufficient. One of application of friction force estimation is external force estimation in which the external force acting on a robot is estimated based on the equation of motion that includes a friction term. External force estimators eliminate the need for force sensors, and the estimated force can be used for arbitrary controllers to maintain the safety of the system or to control the interaction force with the environment. Further application is admittance control, which is one of force control schemes.

One approach to estimate joint friction is a friction model, and another approach is usage of disturbance observers [30, 49, 62, 70, 73, 81], which is a method to estimate disturbance including friction. The fundamental concept is estimating unknown disturbance to a system by difference between the input and the output of the system. Chen et al. [11, 12] have proposed disturbance observers that contain nonlinear term. Nikoobin and Haghighi [71] have proposed a nonlinear disturbance observer for a multi-link manipulator. Generally, disturbance observers contain noise reduction filters such as Butterworth low-pass filter, so their outputs usually include delay. Moreover, disturbance observers are based on the system model except disturbance, so the accuracy of the observers depends on the accuracy of the system model. Straightforward model-based friction estimation is advantageous, because a model-based method requires only a friction model and basically does not require any filter.

1.5.1 External force estimation

This section discusses external force estimation as an application of friction force estimation. There have been many approaches of external force estimation of robots. A conventional structure of external force estimation is illustrated in Figure 1.3, where the estimated value is obtained based on inverse dynamics model including inertia, Coriolis, centrifugal, gravity and friction term. Some researchers [48, 72] have proposed external force estimation methods based on disturbance observers, which regard the external force as the output of disturbance observers subtracted with friction force. Li et al. [61] have applied an external

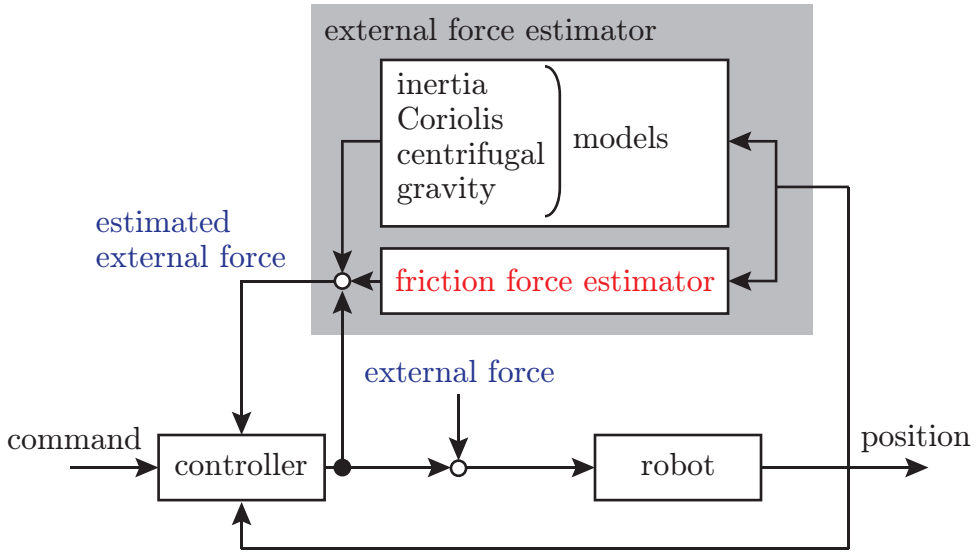

Figure 1.3: Robotic system including friction force estimator.

force estimator based on a disturbance observer to a teleoperated invasive surgical forceps manipulator to send the contact force back to the user. De Luca et al. [18, 19, 28] have developed a method to detect collision between an industrial manipulator and the environment based on the momentum of the manipulator, where the collision is detected as estimated external force, and they have utilized the detection method to make manipulators produce safe reaction to soft objects and human bodies. An external force estimation method using joint torque sensors has been proposed by Phong et al. [76]. Colome et al. [15] have developed an external force estimator of a compliant joint robotic manipulator, which employ a function mapping the relation between the state (position and velocity) and the external force obtained by a learning technique. Daly and Wang [17] have used an external force estimator for control of a bilateral teleoperation manipulator system.

Researchers have dealt friction terms in external force estimators by using simple friction models or employing other estimation methods despite of existence of many analytical friction models. There is a potential possibility to improve the performance of external force estimators by explicitly considering the friction terms.

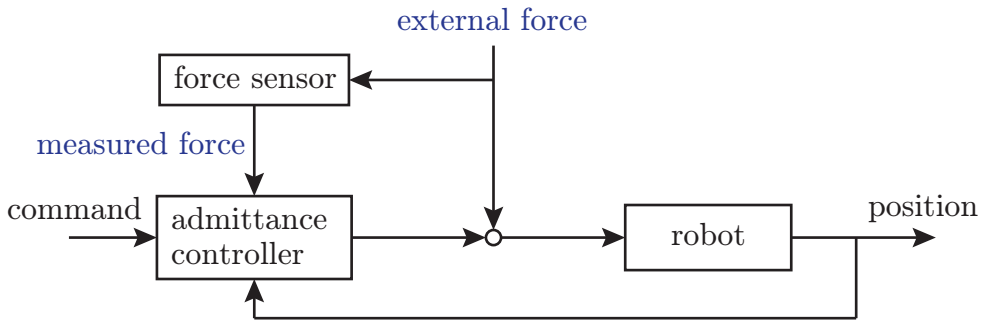

(a) With a force sensor

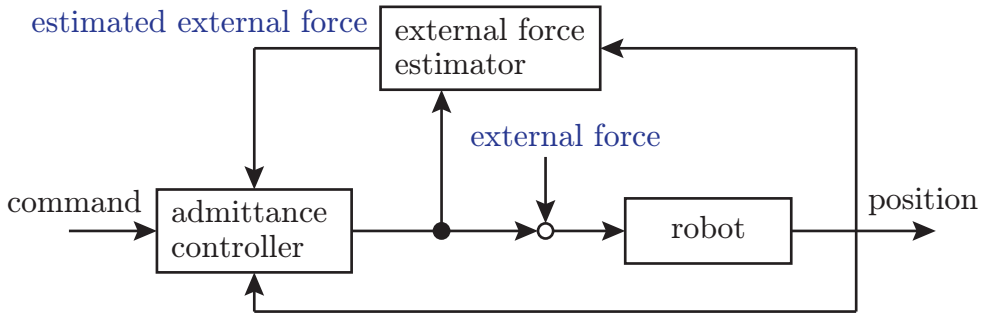

(b) With an external force estimator

Figure 1.4: Robotic system including admittance controller.

1.5.2 Sensorless admittance control

Admittance control [33] is one of force control schemes that intend to produce robot motion achieving a desired admittance, where the word admittance means the relation between the input force and the output velocity. This is also one of applications of friction (external) force estimation techniques. In admittance control systems, the external force is usually measured by force sensors as shown in Figure 1.4(a). Such methods are utilized for exoskeleton robots [99], humanoid robots [100] and electric power steerings [98]. The use of friction (external) force estimators allows us to eliminate the need for force sensors, which have fragileness, high cost, and small sensible parts. The structure of sensorless admittance control system is shown in Figure 1.4(b). External force estimation based on disturbance observers has been used in force control of a multi degree of freedom manipulator [69] and an

injection molding machine [72]. Erden and Tomiyama [22] have proposed a sensorless admittance controller with an external force estimator for a robotic manipulator. In sensorless admittance control, the behavior of the controlled system strongly depends on the accuracy of the force estimation, which also depends on the treatment of the internal friction term.

1.6 Major Achievements

This dissertation is a contribution to handling friction of robotic manipulators by developing an identification procedure, a compensator and an estimator of friction. The major achievements are as follows:

- **Identification procedure for rate-dependent friction law (Chapter 2)**

  This dissertation proposes a procedure for identifying rate-dependent friction of robotic manipulators of which the motion is limited due to the configuration or the environment. The procedure is characterized by the following three features: (i) the rate dependency is represented by line sections connecting sampled velocity-force pairs, (ii) the robot is position-controlled to track desired trajectories that are some cycles of sinusoidal motion with different frequencies, and (iii) each velocity-force pair is sampled from one cycle of the motion with subtracting the effects of the gravity and the inertia. The procedure was tested with a six-axis industrial robotic manipulator Yaskawa MOTOMAN-HP3J, of which the joints are equipped with harmonic-drive transmissions. The experimental results show that the identification is achieved with a sufficient accuracy with the 20 degrees of motion of each joint. In addition, the results were utilized for friction compensation, successfully reducing the effect of the friction by 60 to 80 percent.

- **New elastoplastic friction compensator (Chapter 3)**

  Mahvash and Okamura's elastoplastic friction compensator is one of successful friction compensators for robotic joints with compliant transmissions. A limitation of the scheme is that, in the static friction state, the compensator continues commanding non-zero output force, which hampers the system's reaction to external forces. This dissertation presents an improved version of the elastoplastic friction compensator with an additional

term, which makes the output force decay exponentially in the static friction state. The proposed method was tested using a linear actuator system with a ball screw and a timing belt and an industrial manipulator Yaskawa MOTOMAN-HP3J. The experimental results show that the proposed method reduces external force required to move the device. Further improvement of the compensator is also presented for 'hand-drivabilization.'

• **New elastoplastic friction estimator (Chapter 4)**

This dissertation proposes an elastoplastic friction estimator with improved static friction behavior for the applications of external force estimation and sensorless admittance control. Hayward and Armstrong's elastoplastic friction model is one of the simplest model representing friction phenomena with compliance. This model however produces non-zero output force in the static friction state, which results in steady-state error in external force estimation. This chapter proposes a friction force estimator with the output force being reduced in the static friction state. The proposed estimator was tested through experiments with an actuator system comprised of a ball screw and a timing belt, and an industrial manipulator MOTOMAN-HP3J, Yaskawa Electric Corporation. The experimental results show that the estimation accuracy is improved by the proposed estimator. The friction fore estimator is further improved for admittance controller with the estimator.

1.7 Organization

The connection between each chapters in this dissertation is illustrated as shown in Figure 1.5. The rest of this dissertation is organized as follows. Chapter 2 proposes a new identification procedure for rate-dependent friction in manipulator joints. Chapter 3 proposes a new friction compensator. Chapter 4 proposes a new friction force estimator. Note that joint friction in setups used in Chapter 3 and 4 was identified by the procedure of Chapter 2. Finally, Chapter 5 provides a concluding remarks.

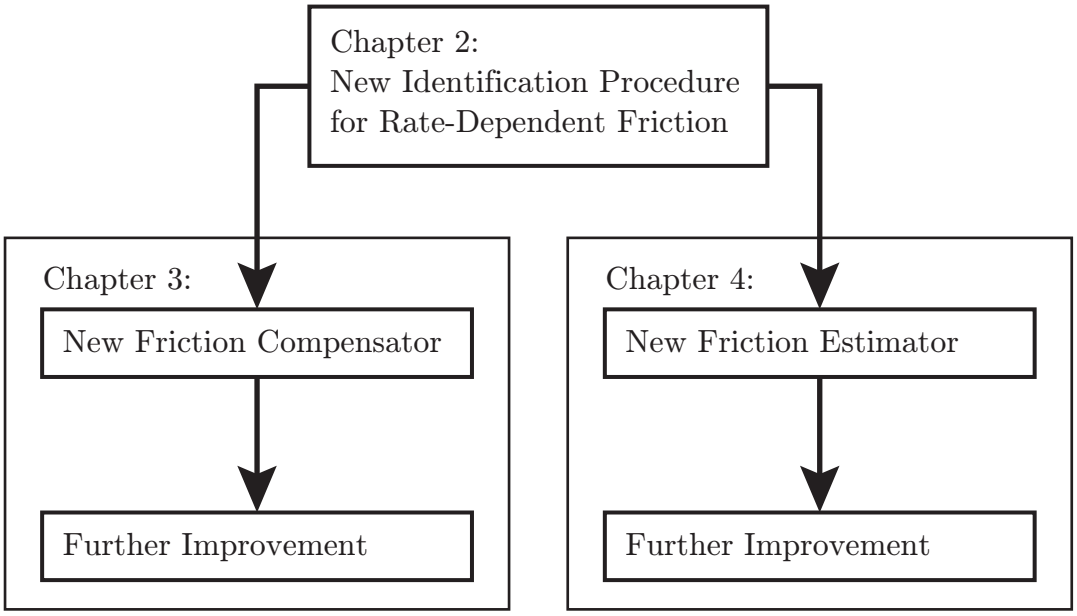

Figure 1.5: Interconnection among chapters.

Chapter 2

Identification of Joint Friction: Identification Procedure for Robotic Joints with Limited Motion Ranges

2.1 Introduction

For the control of robotic manipulators, friction in the joints is one of major disturbances that degrade the accuracy and the precision of control. One straightforward idea to deal with this problem is to calibrate the friction properties of the robot in advance and to compensate the friction force by producing the actuator forces that cancel the friction forces. It is however usually difficult to find appropriate models of the friction phenomena and, even if an appropriate model is available, it is also difficult to clarify how the values of the parameters should be chosen.

Many friction models have been proposed so far, and they vary in the treatment of the discontinuity around the zero velocity and the microscopic elastic displacement in the static friction. A common point shared by various friction models is that they employ a user-defined function of velocity that represents the rate-dependent friction law. That is, for any

★ The content of this chapter is partially published in [40], namely, M. Iwatani and R. Kikuuwe. An Identification Procedure for Rate-Dependency of Friction in Robotic Joints With Limited Motion Ranges. *Mechatronics*, 36:36–44, 2016.

kinds of friction models, the magnitude of the friction force as a function of the velocity must be identified experimentally.

Experimental identification of the rate dependency of the friction force is not always an easy task. Problems such as the limited motion range and the effects of the gravity and the inertia make the identification complicated. The motion of an assembled robotic manipulator is generally limited by the configuration or the environment. Appropriate procedures are needed to measure the friction force at high velocities in a limited motion range, and the identification results need to be insensitive to the effects of inertia and gravity.

This chapter presents a systematic procedure to identify the velocity-friction force relation of devices with limited motion range. The procedure was validated with an industrial six-joint manipulator Yaskawa MOTOMAN-HP3J. It is shown that the identification with a sufficient accuracy was achieved with 20 degrees of motion of the joints. This chapter also shows the application of identified results to friction compensation.

The remainder of this chapter is organized as follows. Section 2.2 overviews previous studies on identification of rate-dependent friction. Section 2.3 proposes the new procedure. Section 2.4 and 2.5 show experimental results obtained with a six-axis manipulator. Section 2.6 provides concluding remarks.

2.2 Related Work

Many friction models have been proposed for the purpose of control. They have realized friction property such as rate-dependency in the kinetic friction [4], elastic displacement in the static friction [16], hysteresis in the velocity-friction relation, stick slip motion [10], non-drifting [1, 87], and smoothness of the output force [96]. Discrete-time models have also been considered [32, 56]. There have been applications of the models to friction compensation [50, 87], and harmonic drive transmissions especially have been the target of applications of modeling studies [5, 20, 42, 91]. One common feature shared by many models including dynamic friction models is that they employ functions of velocity for representing the rate-dependent friction force in the kinetic friction region. It means that the velocity-friction relation must be calibrated in advance for using any kinds of existing models in-

cluding dynamic friction models.

Rate-dependent friction of manipulators can be identified by maintaining a constant velocity for a certain period of time [24, 50]. In such methods, constant velocity commands are sent to the devices, and the resultant actuator torque to maintain the velocity is observed. One drawback of such methods is that maintaining high velocity is generally difficult within a limited range of motion. Another kind of approach is to apply sinusoidal or saw-tooth torque signals to devices to be identified [51, 94]. Such torque command, resulting reciprocating motion, requires a certain level of carefulness in choosing the torque amplitudes so that the trajectory of motion is bounded to a limited range. As mentioned above, the limitation of motion in joints is problematic for identification of rate-dependent friction, so we need a method explicitly handling the limitation of motion.

The gravity and the inertia affect the accuracy of the identified results. A straightforward idea to deal with these factors is to incorporate a system model including the gravity and the inertia into the identification procedure [13,50,51,94]. Major drawbacks of this approach are that the identification of the system model is usually a hard task, and that the identification accuracy of the friction depends on the accuracy of the whole system model.

2.3 Procedure

2.3.1 Overview

This section describes a new identification procedure for rate-dependent friction laws. The procedure is to obtain a set of N velocity-force pairs

$$\mathcal{S} \triangleq \{[V_1, F_1], \cdots, [V_N, F_N]\}, \tag{2.1}$$

which describes the relation between the velocity and the friction force as shown in Figure 2.1. The joint to be identified is controlled to follow sinusoidal trajectories with N different frequencies with a high-gain PID position controller. One cycle of motion is performed for each frequency. The pair $[V_n, F_n]$ is chosen so that the effects of inertia and gravity are small. The identification on each joint is performed on a one-by-one basis, with

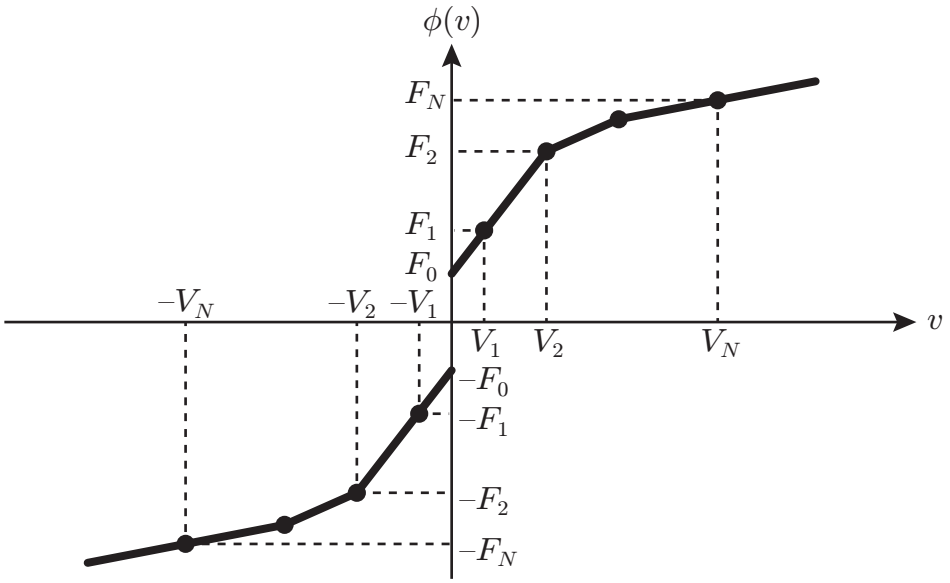

Figure 2.1: Fitted curve $\phi(v)$ defined by (2.8).

the other joints being locked by local position controllers.

2.3.2 Details

The input to the procedure is the following three parameters:

- V : The maximum desired velocity
- A : The amplitude of the sinusoidal motion
- N : The number of sampled velocities

The maximum velocity V should be chosen so that it includes the range of velocity in which the friction force should be identified. The amplitude A should be chosen small enough to match the hardware limitation, and should be smaller to save the time needed for the identification procedure. Its lower bound is determined by the capacity of the actuator because, with a fixed V value, the desired acceleration command is inversely proportional to the A value, as will be shown later. The number N of sampled velocities should be chosen considering the trade-off between the precision of the fitted curve and the time needed for the identification.

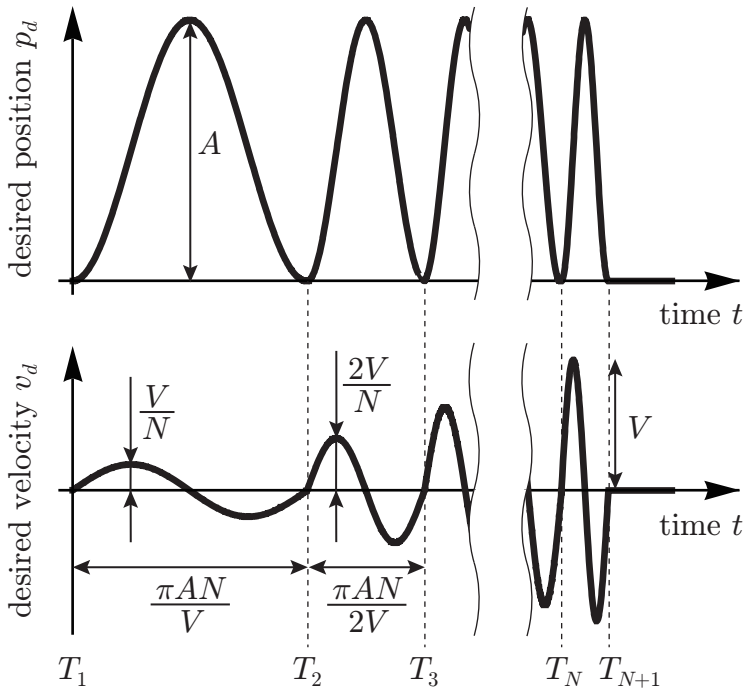

Figure 2.2: Desired trajectory $p_d(t)$ and its derivative $v_d(t)$ for the proposed identification procedure.

As one of the simplest position trajectories to obtain the set $\mathcal{S}$ of velocity-force pairs, the following desired position trajectory has been chosen:

$$p_d(t) \triangleq \frac{A}{2}\left(1 - \cos\left(\frac{2\nu(t)V}{AN}(t - T_{\nu(t)})\right)\right) \tag{2.2}$$

where

$$T_n \triangleq \sum_{j=1}^{n-1} \frac{\pi AN}{jV} \tag{2.3a}$$

$$\nu(t) \triangleq n \text{ s.t. } t \in \mathcal{T}_n \triangleq [T_n, T_{n+1}). \tag{2.3b}$$

This position trajectory $p_d(t)$ is based on the following velocity trajectory:

$$v_d(t) \triangleq \frac{\nu(t)V}{N} \sin\left(\frac{2\nu(t)V}{AN}(t - T_{\nu(t)})\right). \tag{2.4}$$

These trajectories $p_d(t)$ and $v_d(t)$ are illustrated in Figure 2.2. Here, it can be seen that $p_d(t)$ is composed of N times of sinusoidal movements with N different frequencies. The amplitude of the desired position p_d is fixed to A, and the maximum velocity of the nth cycle is nV/N. It should be noted that the amplitude of $\dot{v}_d$ is proportional to V^2/A, and thus the choice of the A value is lower-bounded by the capacity of the actuator. If the chosen A value is too small, the manipulator will not be able to track the resultant desired trajectory, but it will not cause any damage on the hardware and will need only a retry of the procedure with a larger A value. This feature is in contrast to torque-based [51, 94] or velocity-based [24, 50] identification schemes, in which inappropriate parameter design may result in the hardware damage.

Once the joint is position-controlled to track the aforementioned desired trajectory, the data as shown in Figure 2.3 is expected to be obtained. Here, it is advisable that the gains of the position controller should be set as high as possible. The control accuracy however only needs to be enough to realize the velocity above the maximum desired velocity V, which is given as a parameter of the procedure. This is because what is important here is the relation between the applied force f and the actual velocity v, which describes the physical property of the joint, and is not the relation between v and the desired velocity v_d. With a sampling interval Δt, the measured velocity v_i and the applied force f_i are obtained at the time t_i where $i \in \{1, \cdots, I\}$ and

$$I \triangleq T_{N+1}/(\Delta t). \tag{2.5}$$

Consequently, an experiment in the presented procedure provides the following sets of data:

$$\begin{aligned} \mathcal{T}_{\text{all}} &= \{t_1, t_2, \cdots, t_I\} \\ \mathcal{V}_{\text{all}} &= \{v_1, v_2, \cdots, v_I\} \\ \mathcal{F}_{\text{all}} &= \{f_1, f_2, \cdots, f_I\}. \end{aligned} \tag{2.6}$$

The data $\{\mathcal{T}_{\text{all}}, \mathcal{V}_{\text{all}}, \mathcal{F}_{\text{all}}\}$ can be utilized to obtain the set $\mathcal{S}$ through the following function:

$$\text{FunctionA}(\mathcal{T}_{\text{all}}, \mathcal{V}_{\text{all}}, \mathcal{F}_{\text{all}}) \tag{2.7a}$$

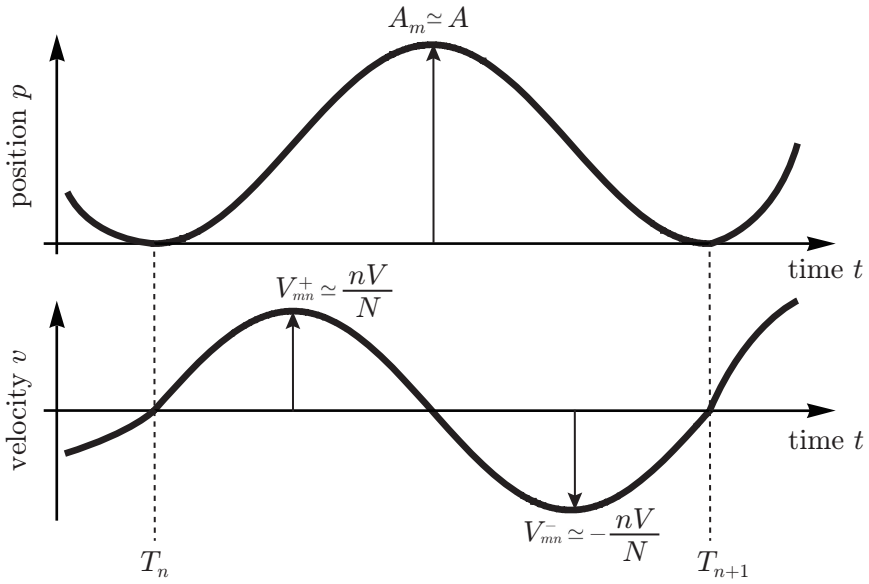

(a) One part of waveform of position p and velocity v

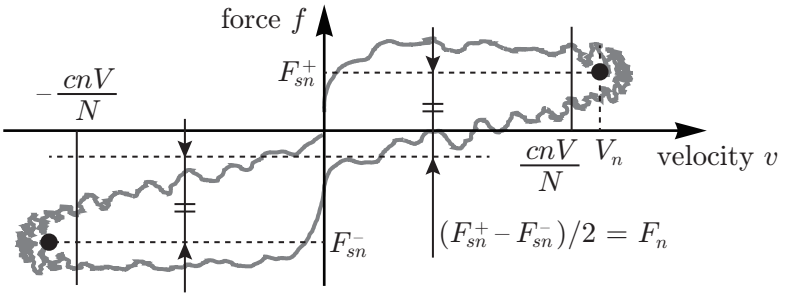

(b) Relation between velocity v and force f

Figure 2.3: Schematic illustration of data that could be obtained from the procedure.

$$\text{for } n := 1 \text{ to } N \tag{2.7b}$$

$$\mathcal{V}_n := \{v_i \in \mathcal{V}_{\text{all}} \mid t_i \in \mathcal{T}_n \wedge v_i \geq cnV/N\} \tag{2.7c}$$

$$\mathcal{F}^+_n := \{f_i \in \mathcal{F}_{\text{all}} \mid t_i \in \mathcal{T}_n \wedge v_i \geq cnV/N\} \tag{2.7d}$$

$$\mathcal{F}^-_n := \{f_i \in \mathcal{F}_{\text{all}} \mid t_i \in \mathcal{T}_n \wedge v_i \leq -cnV/N\} \tag{2.7e}$$

$$V_n := \text{Average}(\mathcal{V}_n) \tag{2.7f}$$

$$F^+_{sn} := \text{Average}(\mathcal{F}^+_n) \tag{2.7g}$$

$$F^-_{sn} := \text{Average}(\mathcal{F}^-_n) \tag{2.7h}$$

$$F_n := (F_{sn}^+ - F_{sn}^-)/2 \tag{2.7i}$$

$$\text{end for} \tag{2.7j}$$

$$\mathcal{S} := \{[V_1, F_1], \cdots, [V_N, F_N]\} \tag{2.7k}$$

$$\text{Return } \mathcal{S}. \tag{2.7l}$$

Figure 2.3(b) illustrates the relations among some variables that appear in this procedure. Here, Average($\mathcal{X}$) is a function that returns the average value of the elements of input set $\mathcal{X}$. The ratio $c \in [0, 1)$ determines the boundaries of the range of the sampled data used for the identification, by multiplying the maximum desired velocity nV/N in each cycle as can be seen in (2.7c)-(2.7e) and Figure 2.3. The ratio is set at $c = 0.8$ in this chapter.

Now, the set $\mathcal{S}$ is obtained through algorithm (2.7). Based on the set $\mathcal{S}$, the rate-dependent friction is defined as the following function $\phi(v)$:

$$f = \phi(v) \triangleq \text{sgn}(v)\big(B_{n(v)}(|v| - V_{n(v)}) + F_{n(v)}\big) \tag{2.8}$$

where

$$B_n \triangleq (F_{n+1} - F_n)/(V_{n+1} - V_n) \ (n \in \{1, \cdots, N-1\}) \tag{2.9a}$$

$$B_0 \triangleq B_1 \tag{2.9b}$$

$$B_N \triangleq B_{N-1} \tag{2.9c}$$

$$V_0 \triangleq 0 \tag{2.9d}$$

$$V_{N+1} \triangleq +\infty \tag{2.9e}$$

$$F_0 \triangleq F_1 - B_0 V_1 \tag{2.9f}$$

$$n(v) \triangleq n \text{ s.t. } V_n \leq v < V_{n+1}. \tag{2.9g}$$

The function is illustrated in Figure 2.1. It is a combination of line sections connecting the elements of the set $\mathcal{S}$, and is symmetric with respect to $v = 0$. Note that all parameters $\{B_n, V_n, F_n\}$ are derived from the set $\mathcal{S}$.

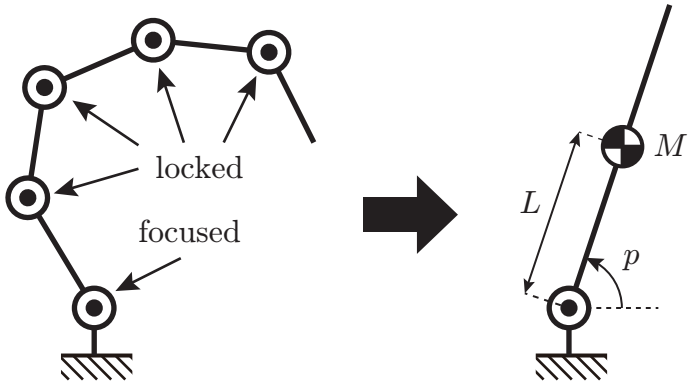

Figure 2.4: Schematic illustration of robot regarded as a 1-link manipulator.

2.3.3 Analysis on the influence of inertia and gravity

The algorithm in this chapter uses only the data near the velocity peaks, and estimates the friction force by taking the semi-amplitude of the force values at the velocity peaks. This is based on the intention to minimize the effects of the inertia and the gravity to the estimated friction force F_n as explained by the following.

Let us regard the robot as a 1-link rotational manipulator because the joints except the focused one are locked as shown in Figure 4. Then, the actuator force f can be represented as follows:

$$f = f_f(\dot{p}) + I\ddot{p} + MLg\cos(p) \tag{2.10}$$

where $f_f(v)$ is the rate-dependent friction force, I is the moment of inertia around the joint, M is the total mass, L is the length from the joint to the center of mass (COM), p is the angle between the horizontal surface and the line passing through the joint and the COM, and g is the gravity acceleration.

As has been explained in Section 2.3.2, the angle p can be given as a sinusoidal function of time t as follows:

$$p = p_0 + A\cos(\omega t) \tag{2.11}$$

where A and ω are the amplitude and the angular frequency of the motion and p_0 is a con-

stant, respectively. Then, (2.10) can be rewritten as follows:

$$f = f_f\left(A\omega\sin(\omega t)\right) - IA\omega^2\cos(\omega t) + MLg\cos\left(p_0 + A\cos(\omega t)\right) \tag{2.12}$$

The force values F_{sn}^{+} and F_{sn}^{-} at the velocity peaks can be written by (2.12) with $t = \pi/(2\omega)$ and $3\pi/(2\omega)$ as follows:

$$F_{sn}^{+} = f_f\left(A\omega\right) + MLg\cos\left(p_0\right) \tag{2.13a}$$

$$F_{sn}^{-} = f_f\left(-A\omega\right) + MLg\cos\left(p_0\right) \tag{2.13b}$$

Substituting (2.13a) and (2.13b) for (2.7i) yields the following equation:

$$F_n = \left(f_f\left(A\omega\right) - f_f\left(-A\omega\right)\right)/2 \simeq f_f\left(A\omega\right) \tag{2.14}$$

because of the assumption that the rate-dependent friction force is symmetric with respect to $v = 0$, that is, $f_f\left(-A\omega\right) \simeq -f_f\left(A\omega\right)$.

What (2.14) implies is that F_n does not depend on the inertia term $I\ddot{p}$ or the gravity term $MLg\cos(p_0)$. This can be explained by the fact that the acceleration is close to zero at the velocity peaks and the angle joint at the two velocity peaks are close to each other.

2.4 Experiment: Identification

2.4.1 Experimental setup

The proposed identification procedure was experimentally tested with a six-axis robotic manipulator Yaskawa MOTOMAN-HP3J shown in Figure 2.5. A harmonic drive transmission is embedded to each joint. Table 2.1 shows the specification of each joint. A force sensor NITTA IFS-50M31A25-I25 is attached at the end-effector to measure the external force in experiments of friction compensation to which the identified results are applied.

The experimental comparison with methods in literature is not included in this chapter. The proposed method is based on the position control, which is intrinsically capable

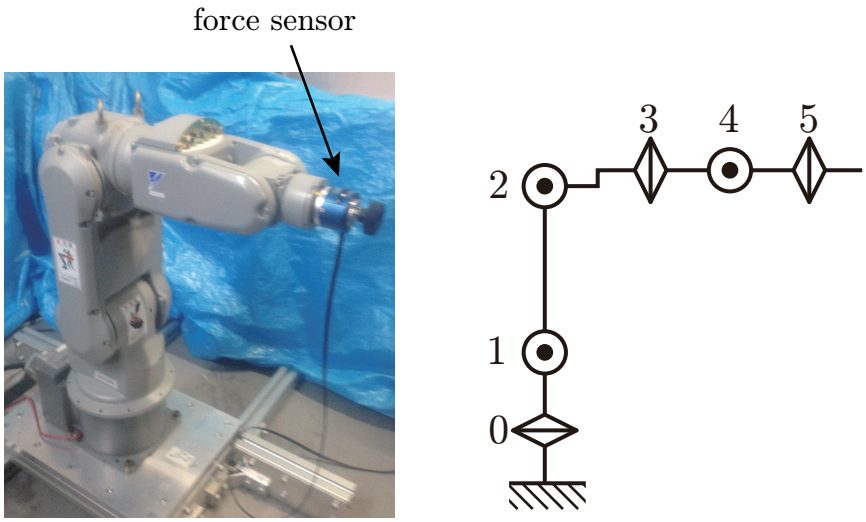

(a) MOTOMAN-HP3J (b) Configuration

Figure 2.5: Experimental setup.

Table 2.1: Specification of the experimental setup.

Joint number [-]	0	1	2	3	4	5
Reduction ratio [-]	100	224	120	120	100	81.5
Maximum velocity [deg/s]	200	135	190	250	300	360
Maximum torque [Nm]	95.1	213.1	114.1	34.2	28.5	23.3

of limiting the joint motion within the mechanical limitations. In contrast, other methods are based on torque command [51, 94] or velocity command [13, 24, 50], and thus there is the possibility that the motion of the joint arrives in the mechanical limitation. Therefore, experiments under the same condition cannot be performed. Previous methods focused on, for example, identification in low velocity range [50], position-dependent friction [24], dynamic friction models [51], nonlinear optimization problem [94], or identification using transfer functions [13].

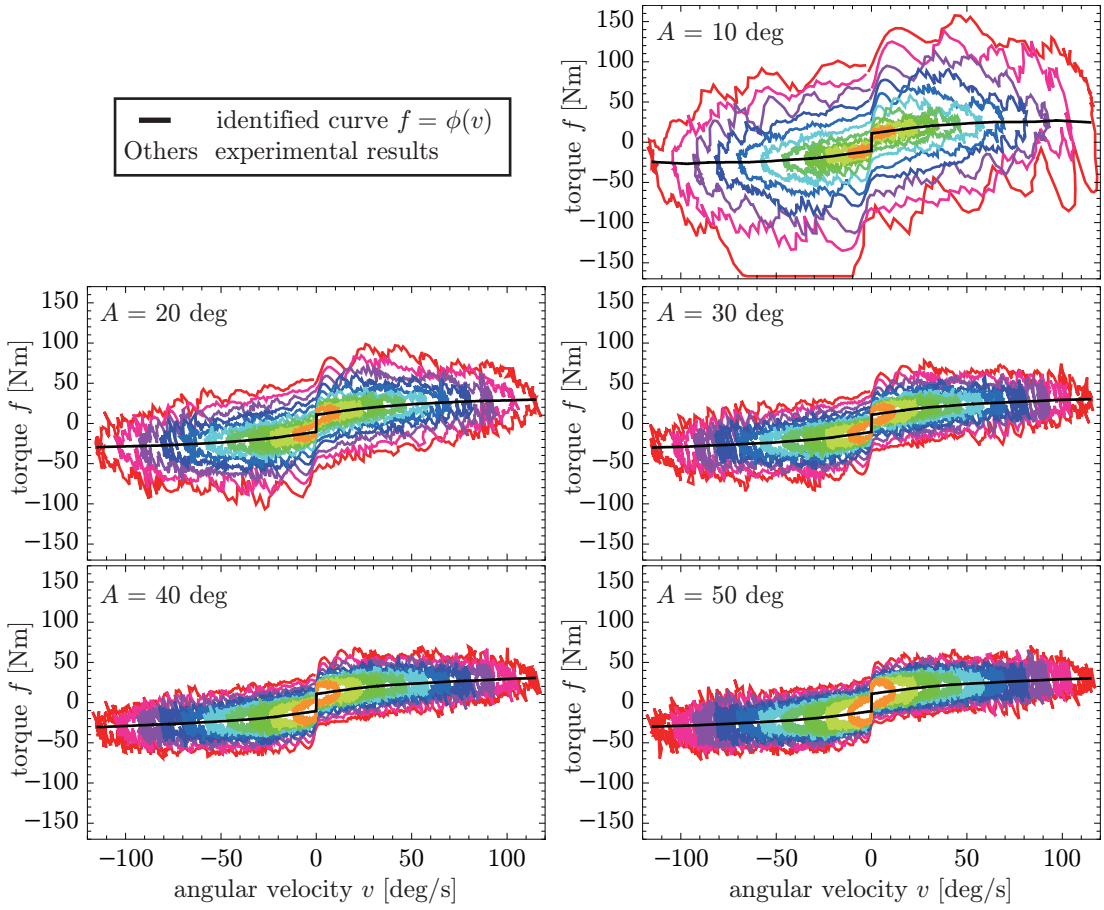

Figure 2.6: Experimental results and the identified curves in the cases of various A at Joint 1. Experimental results are unbiased.

2.4.2 Sensitivity to the choice of A

It is desirable to set A as small as possible for reducing the time needed for the identification, because the time required for tracking the trajectory (2.2) is proportional to A as shown in the following equation:

$$T_{N+1} = \frac{\pi A N}{V} \sum_{j=1}^{N} \frac{1}{j}, \tag{2.15}$$

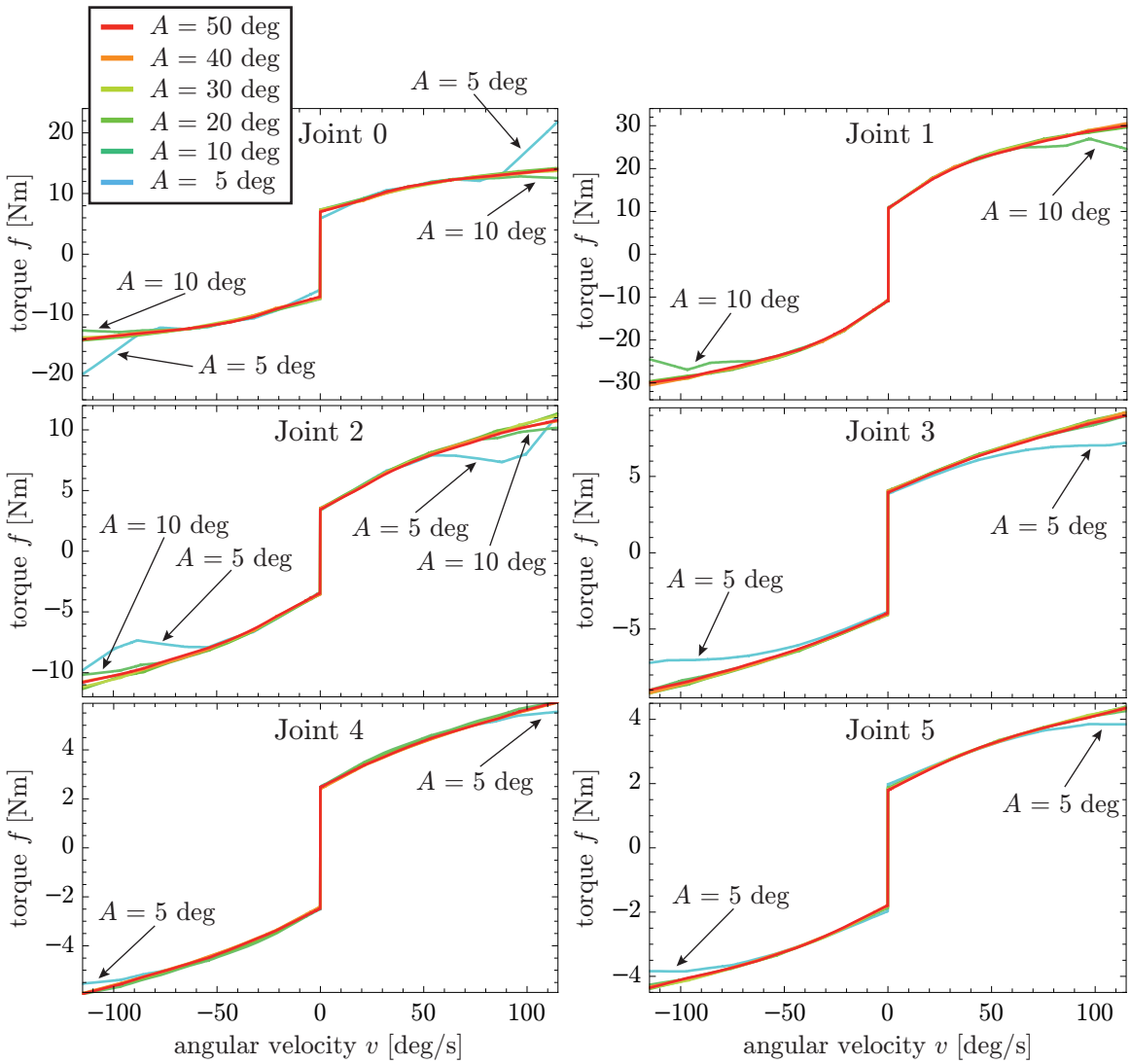

Figure 2.7: Identification results of each joint in various cases of A under $V = 115$ deg/s (2.0 rad/s) and $N = 10$. The result in the case of $A = 5$ deg at Joint 1 was not obtained due to the limit of the servo controller.

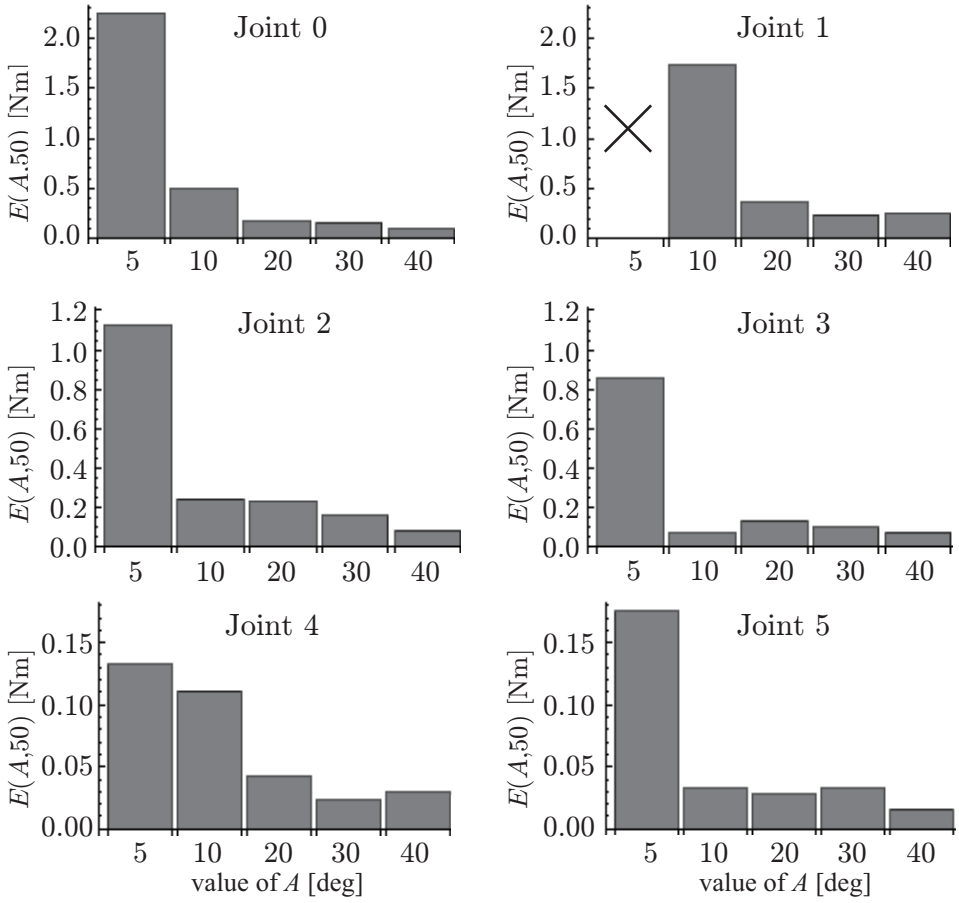

Figure 2.8: Difference between each curve and the curve of $A = 50$ deg based on (2.16) under $V = 115$ deg/s (2.0 rad/s) and $N = 10$. The symbol $\times$ means that the result was not obtained due to the limit of the servo controller.

which can be seen in (2.3) and Figure 2.2. Figure 2.6 shows experimental results and identified curves with various values of A, under $V = 115$ deg/s (2.0 rad/s) and $N = 10$. Figure 2.6 is the result of Joint 1, where the effect of the gravity and the inertia is the largest among all joints. The bias of each experimental result is removed to make it comparable to the fitted curve $\phi(v)$ obtained by the proposed procedure. It can be seen that smaller A, resulting larger effect of inertia, broadens the width of the curves and also perturbs the fitted curve $\phi(v)$. Therefore, it can be concluded that too small A deteriorates the accuracy of the identification. The following shows how small A can be at each joint.

Figure 2.7 is the identified results with various A at each joint. In this figure, one can see

that the curves of A larger than 10 deg are almost overlapping. Thus, it can be said that the amplitude of trajectory $A = 20$ deg is enough to identify the friction curve appropriately. Moreover, it is clear that the slope of the identified curves in the high velocity range is different from that in low velocity range. This indicates that the high velocity range should also be identified experimentally, not only by extrapolation.

In order to validate the results quantitatively, we use the following distance metric:

$$E(A_1, A_2) = \sqrt{\frac{1}{V}\int_0^V (\phi_{A_1}(v) - \phi_{A_2}(v))^2 dv}. \tag{2.16}$$

This metric represents the difference between the curves $\phi_{A_1}(v)$ and $\phi_{A_2}(v)$ that are obtained with $A = A_1$ and A_2 respectively. Figure 2.8 shows the quantitative difference between each curve and the curve of $A = 50$ deg at each joint. It is shown that the differences are large when $A = 5$ or 10 deg. These results correspond to Figure 2.7, quantitatively indicating that the trajectory amplitude of $A = 10$ or 20 deg is the minimum necessary value for appropriate identification, under the condition of the range of velocity $V = 115$ deg/s (2.0 rad/s) in the device MOTOMAN-HP3J.

One limitation of the scheme is that the identified curve is always a continuous function of velocity except the zero velocity. This issue however should not be viewed as a critical problem for many lubricated actuators because, in such mechanisms, the static friction state and the kinetic friction states are continuously connected through the Stribeck effect.

2.4.3 Sensitivity to the posture

Another set of experiments were carried out to show the effects of inertia and gravity on the identification results. The identification was performed on Joint 1 with five different postures shown in Figure 2.9(a) under the condition of $A = 20$ deg, $V = 115$ deg/s (2.0 rad/s) and $N = 10$. The different postures yield the different inertia and gravity force with respect to the joint. Figure 2.9(b) is the identification results, which show that the curves are almost

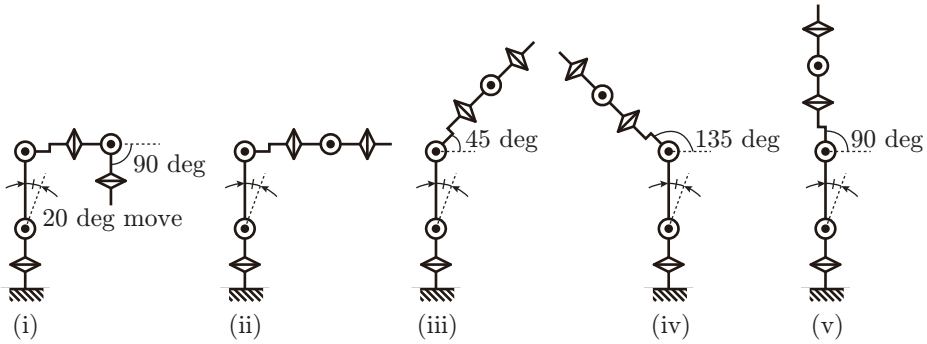

(a) Conditions of the posture

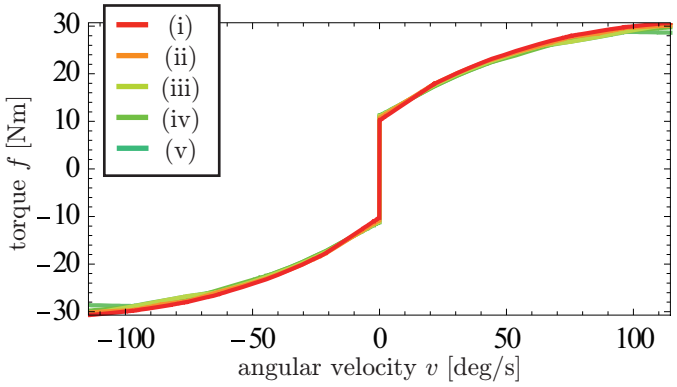

(b) Identified curves

Figure 2.9: Identification results with various postures of Joint 1 under the condition of $A = 20$ deg, $V = 115$ deg/s (2.0 rad/s) and $N = 10$. The effect of inertia is largest in Posture (v) and smallest in Posture (i). The effect of gravity is largest in Posture (ii) and smallest in (v).

overlapping. For quantitative validation, the following criterion is used:

$$E_p(P_1, P_2) = \frac{\sqrt{\frac{1}{V}\int_0^V \left(\phi_{P_1}(v) - \phi_{P_2}(v)\right)^2 dv}}{\sqrt{\frac{1}{V}\int_0^V \left(\phi_{P_2}(v)\right)^2 dv}}, \tag{2.17}$$

which is the ratio of the difference between two curves with Posture P_1 and P_2 to the magnitude of $\phi_{P_2}(v)$, where $P1,\ P2 \in \{(\mathrm{i}),\ (\mathrm{ii}),\ (\mathrm{iii}),\ (\mathrm{iv}),\ (\mathrm{v})\}$. Table 2.2 shows the difference (2.17) under $P_2 = (\mathrm{i})$. In this table, we can see that the differences are below 4%. This result shows that the identified curves are close to each other. Therefore, It can be said that

Table 2.2: Difference between each curve and the curve of Posture (i) based on (2.17).

P_1	(ii)	(iii)	(iv)	(v)
$E_p(P_1, (\mathrm{i}))$ [%]	1.28	2.82	3.09	3.95

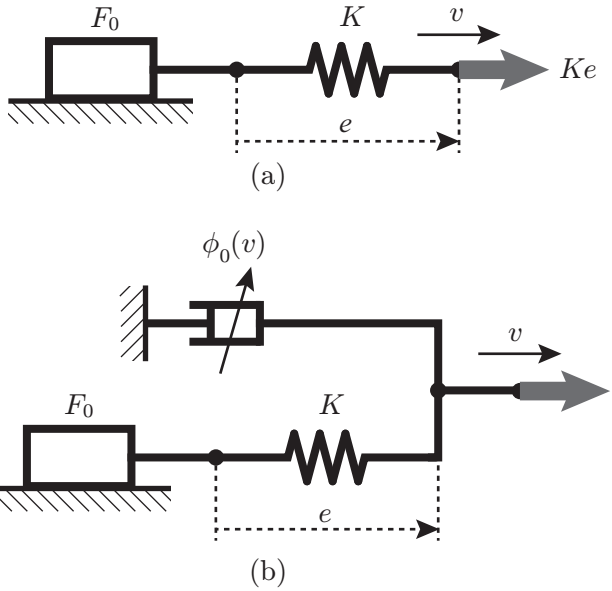

Figure 2.10: Friction models for compensation: (a) elasoplastic friction model, (b) the model in this chapter.

the dependency of identification results on the posture is small. This indicates that using only the data near the velocity peaks (lines (2.7c)-(2.7e)), and taking the semi-amplitude of the force (line (2.7i)) are effective enough to remove the effects of the inertia and the gravity.

2.5 Experiment: Friction Compensation

The identified results were validated through experiments of friction compensation. Here, the identified curve is combined with a dynamic friction model of Hayward and Armstrong [32] and employed for friction compensation in the similar manner as the method presented by Mahvash and Okamura [66]. In the technique presented in [66], the friction force is modeled as a serial connection of a spring and a Coulomb friction element, as illus-

trated in Figure 2.10(a). In the same light, we used a model illustrated in Figure 2.10(b), in which a nonlinear viscosity is connected in parallel with a Coulomb friction-spring element. The algorithm of the model in Figure 2.10(b) can be described as follows:

$$e_k := \frac{F_0}{K}\mathrm{sat}\left(\frac{K}{F_0}\left(\Delta t v_k + e_{k-1}\right)\right) \tag{2.18a}$$

$$f_{o,k} := Ke_k + \phi_0(v_k) \tag{2.18b}$$

where

$$\phi_0(v_k) \triangleq \phi(v_k) - F_0\mathrm{sgn}(v_k), \tag{2.19}$$

k denotes the index of the discrete time, and function sat(x) is defined as follows:

$$\mathrm{sat}(x) \triangleq \begin{cases} x/|x| & \text{if } |x| > 1 \\ x & \text{if } |x| \leq 1. \end{cases} \tag{2.20}$$

Here, e_k is the displacement of the spring, and (2.18a) comes from the fact that the Coulomb friction force $F_0\mathrm{sat}\left(\frac{K}{F_0}\left(\Delta t v_k + e_{k-1}\right)\right)$ balances the spring force Ke_k. The output is force $f_{o,k}$. By noting the relation between $\phi(v_k)$ and F_0 illustrated in Figure 2.1, we can easily see that $\phi_0(v_k)$ is a continuous function. The K value was chosen as 175 Nm/deg (10000 Nm/rad) through preliminary experiments. Higher K values resulted in oscillation and lower K values resulted in insufficient compensation.

Another important point is that, in order to ensure the stability, the actuator force f_k used for the friction compensation should be slightly smaller than the actual friction force. Thus, the actuator force f_k should be determined as follows:

$$f_k := Rf_{o,k} \tag{2.21}$$

where R is an appropriate positive constant that is slightly smaller than 1. We used $R = 0.9$ in the experiments reported in this chapter.

In conclusion, a discrete-time algorithm to obtain the actuator force f_k for friction com-

pensation is obtained as follows:

$$e_k := \frac{F_0}{K}\mathrm{sat}\left(\frac{K}{F_0}\left(\Delta t v_k + e_{k-1}\right)\right) \tag{2.22a}$$

$$f_{o,k} := Ke_k + \phi_0(v_k) \tag{2.22b}$$

$$f_k := Rf_{o,k}. \tag{2.22c}$$

The algorithm (2.22) exemplifies the combined application of the identified curve $\phi_0(v_k)$ and dynamic friction models.

2.5.1 Manual moving

In this experiment, the experimenter grasped the end-effector of the manipulator and moved it cyclically in both cases without friction compensation and with compensation. The external torque f_s to move the manipulator was derived from the output values of the force sensor attached at the end-effector and the length of the moment arm. All joints except the focused joint were locked by local position controller with as high gain as possible. Gravity compensation, of which the parameters were calibrated in advance, was applied to each joint. The experimenter intended to move the end-effector by hand at the frequency of 0.5 Hz, being paced by a metronome.

Figure 2.11 shows the experimental results of friction compensation. Data of the Joint 3 and 5 were not obtained due to the limitation of the force sensor, of which the rated torque is smaller than the necessary torque to move these joints. Figure 2.11 shows that, while the velocity v does not exhibit significant difference between the two cases, the measured torque f does exhibit distinct difference, which are the lowered magnitudes and the forward-shifted phase in the case with the compensation. Such features cannot be created by the experimenter's intention and can be solely attributed to the reduction of the friction force due to the friction compensation. One can infer that the phase shift is also a consequence of the reduction of the friction force, which results in the inertia being dominant.

The measured velocity and the measured external torque were evaluated quantitatively

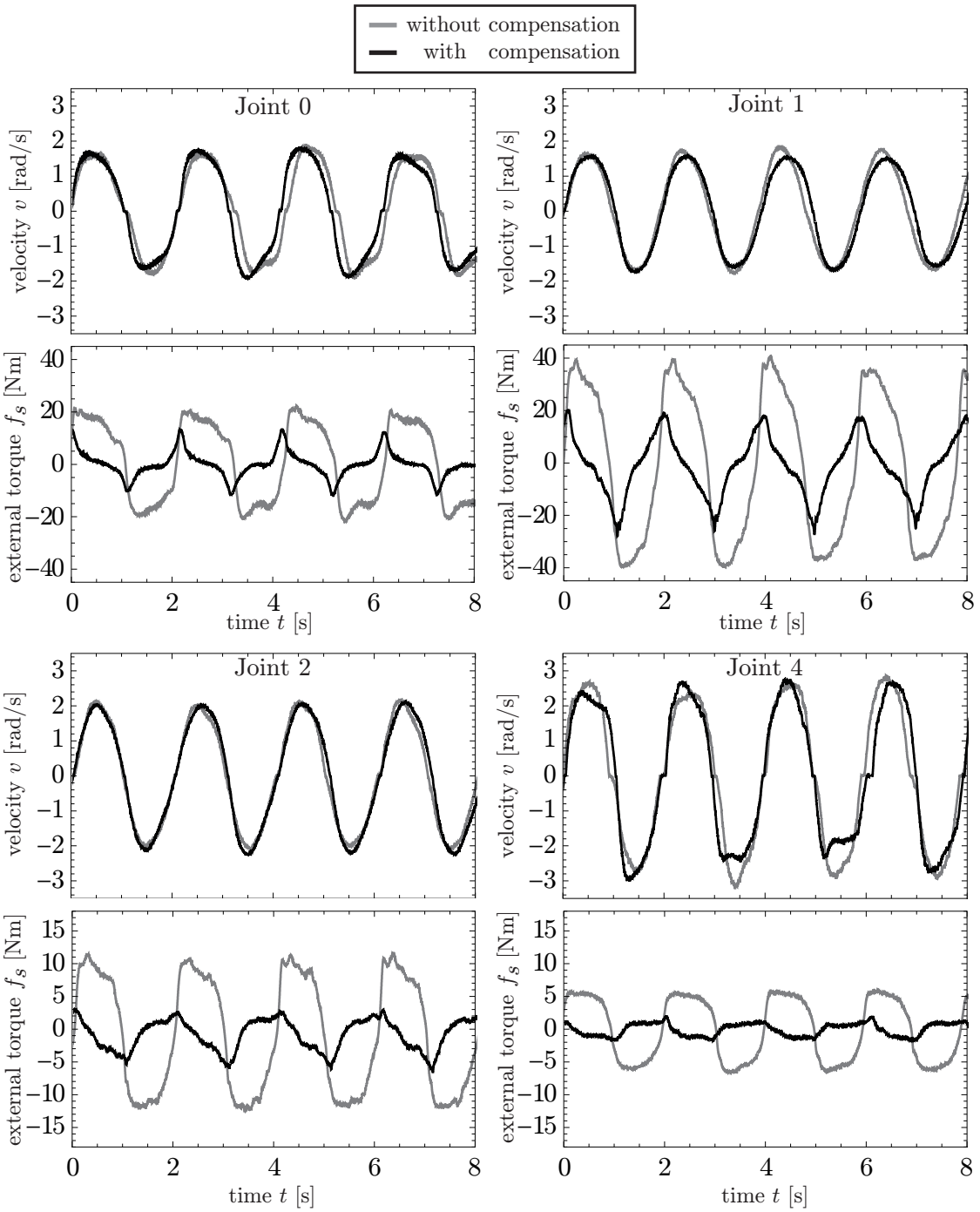

Figure 2.11: Experimental result of friction compensation. Data were not obtained from Joint 3 and 5 due to the limitation of the force sensor.

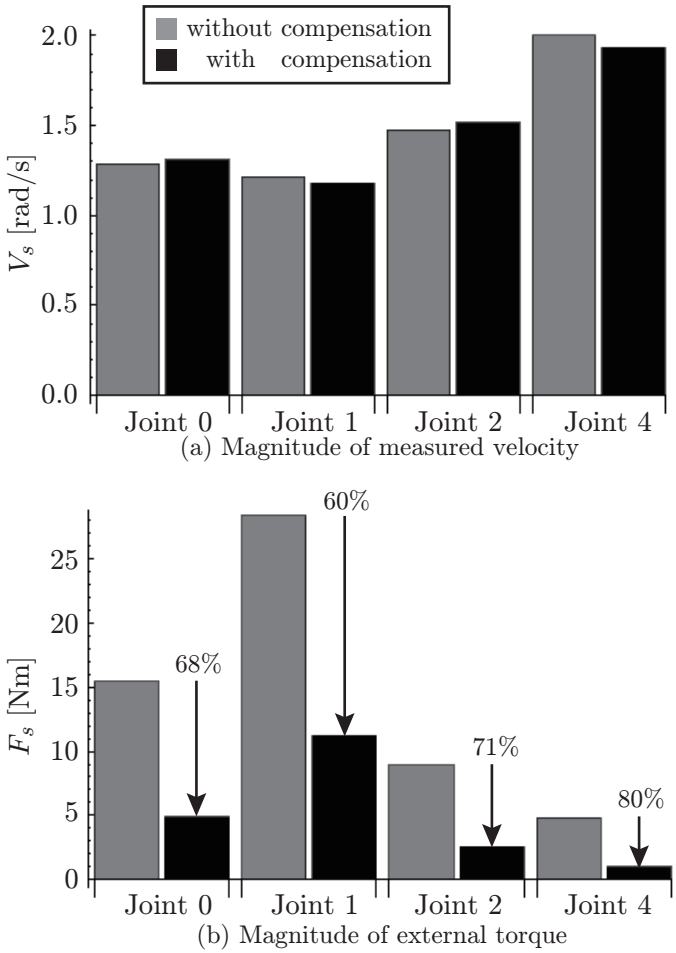

Figure 2.12: Average magnitudes (2.23) of measured velocity and external torque. Data were not obtained from Joint 3 and 5 due to the limitation of the force sensor.

by using the following criteria:

$$V_s = \sqrt{\frac{1}{T_e}\int_0^{T_e} v_s^2\, dt}, \quad F_s = \sqrt{\frac{1}{T_e}\int_0^{T_e} f_s^2\, dt} \tag{2.23}$$

where T_e is the time period of an experiment. The results are shown in Fig 2.12. This figure shows that, although the magnitude of the measured velocity is almost equal between the two cases, the magnitude of the measured torque is smaller by 60 to 80 percent in the case with the friction compensation. It means that the friction compensation decreases the

magnitude of torque required to realize given velocities. These results indicate that the function identified by the proposed procedure is effective in the friction compensation.

2.5.2 Feedback position tracking

In this experiment, a low-gain PD position controller for a saw-teeth desired trajectory was applied to each joint one-by-one in the four cases as follows: no compensation (NC), compensation by the model of Mahvash and Okamura [66] (MO), MO and linear viscosity compensation (MOL), MO and compensation using functions identified by the proposed procedure (MOP). As is the case with Section 2.5.1, all joints except the focused one were locked and the gravity compensation was applied to each joint. In the case of MO, the following equation was used instead of (2.22b):

$$f_{o,k} := Ke_k \tag{2.24}$$

and in the case of MOL, the following equation was used:

$$f_{o,k} := Ke_k + B_c v_k \tag{2.25}$$

where B_c is a constant coefficient for the linear viscosity compensation.

Figure 2.13 shows the results, which show that the tracking accuracy is overall highest with MOP. Figure 2.14 shows a quantitative comparison of the tracking errors with the following criterion:

$$E_s = \sqrt{\frac{1}{T_e}\int_0^{T_e} (p_d - p_s)^2 \, dt}. \tag{2.26}$$

Figure 2.14 also shows that MOP provides smaller tracking error than MOL, MO, and NC. These results indicates that the friction compensation significantly reduces the tracking error of position control, and also indicates that using the rate-dependent friction law, which is obtained by the proposed method, is more effective than simple Coulomb friction law or Coulomb plus linear viscous friction law. The results also support the effectiveness of the

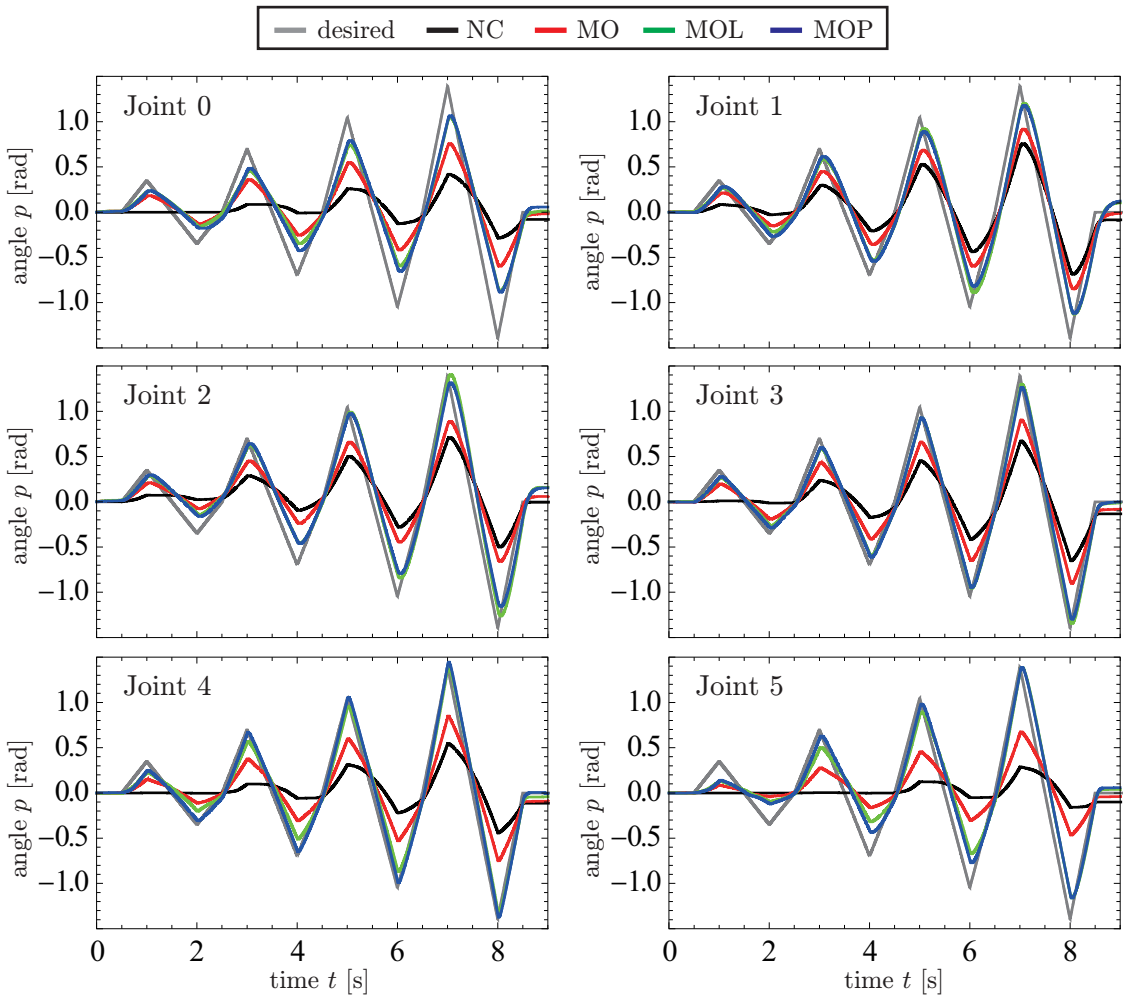

Figure 2.13: Experimental result of friction compensation in the four cases as follows: no compensation (NC), compensation by (2.24) (MO), MO and linear viscosity compensation (MOL), MO and compensation using functions identified by the proposed procedure (MOP).

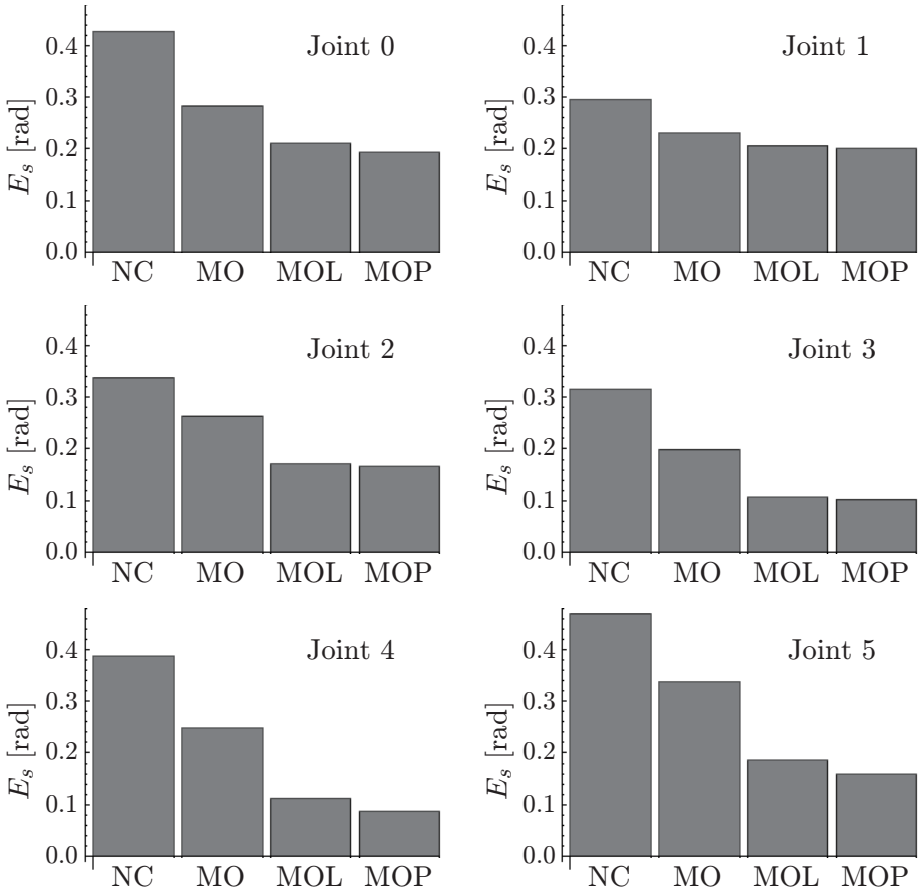

Figure 2.14: Average magnitudes (2.26) of measured position tracking error.

method combining the identified curve and dynamic friction models.

2.6 Summary

This chapter has presented an identification procedure for rate-dependent friction of manipulators of which the motion is limited. The procedure has the following characteristic features: (i) the function representing the rate dependency is defined by line sections connecting sampled velocity-force pairs, (ii) each joint is controlled as it tracks desired position trajectories consisting of some cycles of sinusoidal motion with different frequencies, and (iii) each velocity-force pair is sampled from each cycle of the motion with subtracting the

effects of the gravity and the inertia. The procedure was applied to a Yaskawa MOTOMAN-HP3J, which is a six-joint robotic manipulator with harmonic-drive transmissions. It has been shown that the identification up to the velocity of 115 deg/s (2.0 rad/s) was achieved with a 20-deg sinusoidal motion. Experimental results have also shown that the friction of the manipulator was reduced by 60 to 80 percent by the compensation using the identified function.

Chapter 3

Compensation of Joint Friction: New Elastoplastic Friction Compensator

3.1 Introduction

Joint friction of mechanical systems is one of major causes deteriorating the accuracy of control and the backdrivability. One idea to deal with this problem is to generate actuator forces canceling the friction force, i.e., friction compensation. It is however not always a trivial problem to find an appropriate compensator. One major factor of the difficulty is that the friction force is generally formulated as a discontinuous function of sliding velocity. inappropriate treatment of the discontinuities causes high frequency oscillation in the actuator force in the neighborhood of the zero velocity.

One of simplest friction models is perhaps Hayward and Armstrong's model [32]. Their friction model can be seen as an elastoplastic friction model, which is composed of a serial connection of elastic component and Coulomb friction component. Many of other friction models can be seen as extensions of Hayward and Armstrong's model. For example, Dupont et al.'s model [21] is a single state elastoplastic friction model with a sophisticated presliding behavior. Kikuuwe et al. [56] have proposed a visco-elastoplastic model, which is a general-

★ The content of this chapter is partially published in [38], namely, M. Iwatani and R. Kikuuwe. An Elastoplastic Friction Compensator With Improved Static Friction Behavior. In *Proceedings of SICE Annual Conference 2016*, pages 1091–1097, 2016.

ization of Hayward and Armstrong's model with non-zero viscosity. Xiong et al. [96] have presented a multi-state friction model, which is a parallel connection of visco-elastoplastic elements.

The originally intended application of Hayward and Armstrong's elastoplastic friction model [32] is haptic rendering, in which artificial friction forces are generated by actuators, as opposed to friction compensation, in which the real friction forces are canceled by actuator forces. Mahvash and Okamura [66], however, employed their model for the purpose of friction compensation of tendon-driven mechanism, in which the compliance of the elastoplastic friction model corresponds to the compliance of the tendon. A similar idea has been employed by Iwatani et al. [42], in which a multi-state visco-elastoplastic friction model has been used for friction compensation of a harmonic drive transmission. Tjahjowidodo et al. [91] have also developed a friction compensator for a harmonic drive based on a multi-state friction model [1].

This chapter focuses on a flaw of friction compensators employing conventional elastoplastic friction models, which has not been pointed out in previous studies. The flaw is that, in the static friction state, such a compensator continues producing non-zero actuator force caused by the estimated elastic displacement of the joint. This 'unnecessary' compensation force hampers the sensitivity of the joint against the external force. Motivated by this observation, this chapter proposes an improved elastoplastic friction compensator, which includes an additional term that makes the compensation force exponentially decay in the static friction state.

The proposed method also includes a sinusoidal dither-like actuation in the static friction state, which further enhances the sensitivity of the system against the external forces. Moreover, this chapter presents an additional algorithm for the compensator, with which the decay rate of the output force is adjusted in real time to realize a better behavior of the system both kinetic and static friction state. The proposed method was validated with a linear actuator system with a ball screw and a six-axis industrial manipulator. It is shown that the proposed method enhances the backdrivability of the system.

The rest of this chapter is organized as follows. Section 3.2 shows the property of the experimental setup. Section 3.3 overviews Mahvash and Okamura's elastoplastic friction

compensator. Section 3.4 explains the proposed elastoplastic friction compensator. Section 3.5 shows experimental validation of the proposed method. Section 3.6 presents the additional algorithm for the online adjustment of the decay rate, and also shows some experimental results. Section 3.7 provides concluding remarks.

3.2 Experimental Setup

3.2.1 Overview

This section provides an overview of robotic devices used in this chapter, which are shown in Figure 3.1. The Setup A, shown in Figure 3.1(a), consists of the following components: an AC servomotor in which an optical encoder is embedded, linear guides, a ball screw, a timing belt and pulleys. The end-effector and the actuator are connected through a compliant transmission i.e., the timing belt. The Setup B, shown in Figure 3.1(b), is a six-axis industrial manipulator MOTOMAN-HP3J, Yaskawa Electric Corporation. Each joint of this setup has an AC servomotor, an optical encoder and a harmonic drive transmission, which has compliance.

In each of the setups, the friction mostly exists on the end-effector's side, not on the actuator and the optical encoder's side. This feature raises a difficulty in the friction compensation because the end-effector's velocity cannot be measured directly with the optical encoder.

The mechanism structures of the setups can be schematically illustrated as Figure 3.2. Here, p and q_c are the position of the motor and the end-effector, respectively, K_c is the elasticity of the compliant transmission, f_f is the friction force on the side of the end-effector, f is the force of the actuator, and f_e is external forces acting on the end-effector. The configuration of the friction and the compliance is the same as that of Mahvash and Okamura [66], where a tendon-driven joint is modeled in the same way as Figure 3.2.

As for Setup A, the rated power of the motor is 200 W, the lead of the ball screw is 0.02 m, and the resolution of the encoder is 4000 counts per rotation. As for Setup B, the industrial manipulator, only the three joints from the base are used in this chapter. In these three joints (Joints 0, 1 and 2), all the actuators' rated power is 80W, all the encoders'

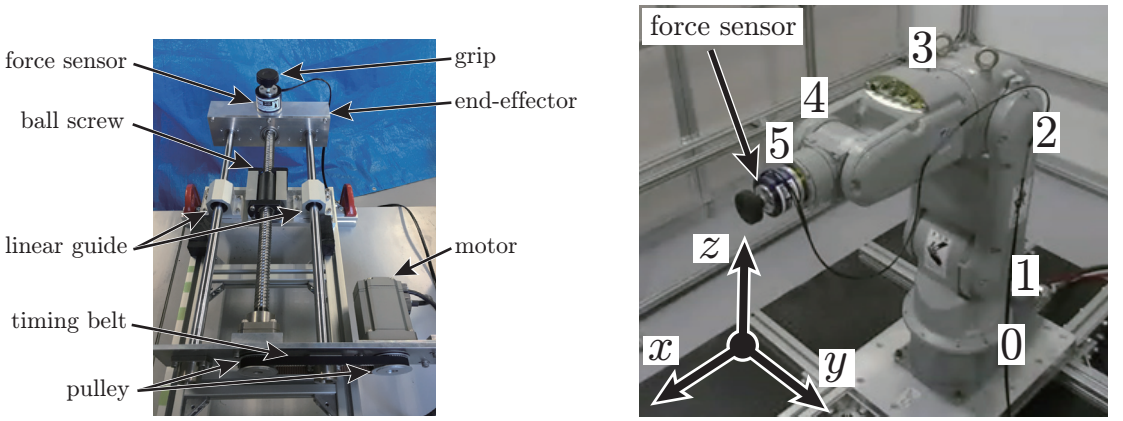

(a) Setup A: Linear Actuator (b) Setup B: Yaskawa MOTOMAN-HP3J

Figure 3.1: Experimental setups.

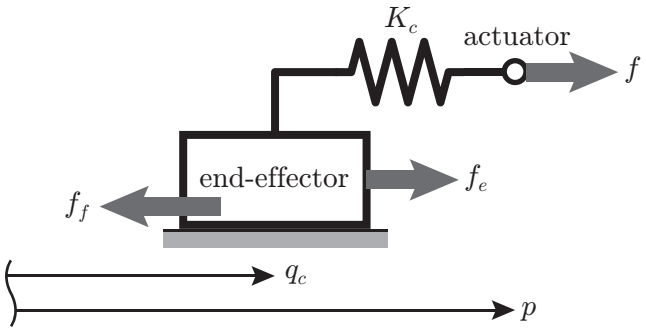

Figure 3.2: Schematic illustration of the setups.

resolution is 65,536 counts per rotation, and the reduction ratios of the transmissions are 100, 224 and 120, respectively. A force sensor NITTA IFS-50M31A25-I25 is attached to the end-effector of each setup to measure the external force in experiments.

3.2.2 Presliding behavior

Preliminary experiments were performed to clarify the presliding behavior of the setups. In these experiments, ramp-type force input was applied to the joints by the actuators. Figure 3.3 shows the results. Figure 3.3(a) shows that the measured displacement of Setup A is zero as long as the actuator force is smaller than 6 N. On the other hand, in Figure 3.3(b),

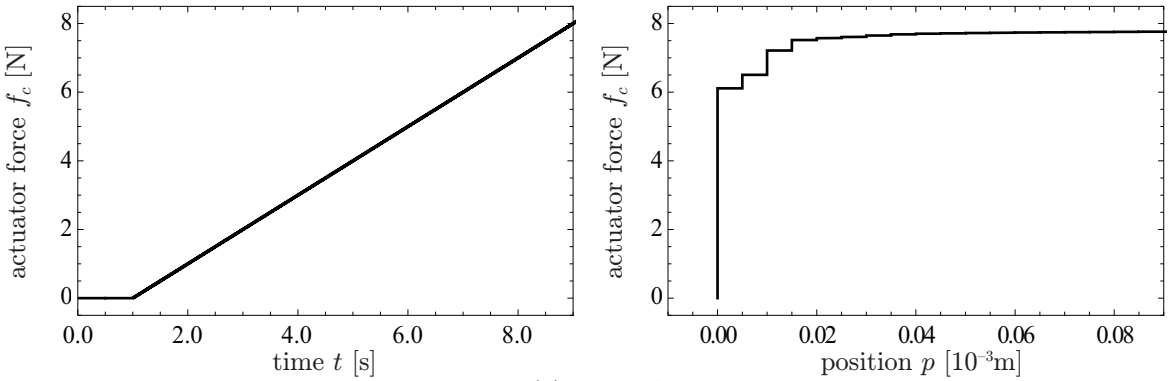

(a) Setup A

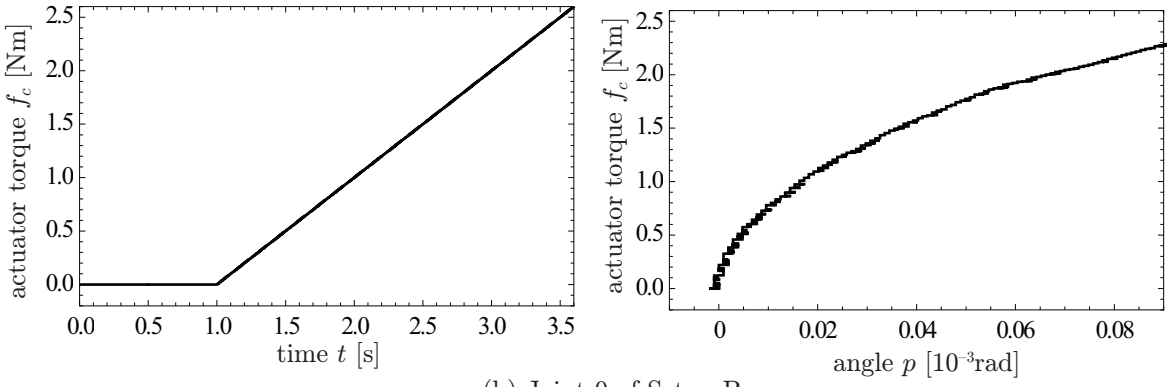

(b) Joint 0 of Setup B

Figure 3.3: Presliding displacement.

Joint 0 of Setup B exhibits significant presliding displacement under small actuator torque.

The difference of presliding behavior in the two setups comes from the differences in the stiffness of the transmissions and the resolution of the encoders. In Setup A, the elongation of the timing belt was smaller than displacement for one count of the encoder step due to the high stiffness of the belt. On the other hand in Setup B, the resolution of the encoder is high enough to measure small displacement with small torque.

3.2.3 Rate-dependent friction

In order to investigate the relation between the velocity and the friction force in the setups, this chapter used the identification procedure proposed in Chapter 2 (and also [37]). The

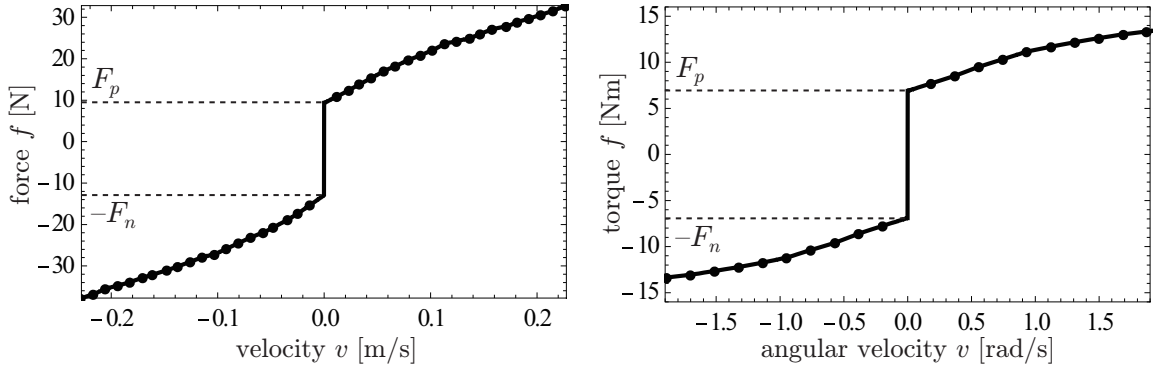

(a) Setup A (b) Joint 0 of Setup B

Figure 3.4: Identification result of rate-dependent friction.

procedure was slightly modified to deal with different magnitudes of friction in different directions. Figure 3.4 shows the obtained data and curves from the procedure. The curves are described in the following form:

$$f \in \mathrm{gsgn}(-F_n, v, F_p) + \Phi(v) \tag{3.1}$$

where v is the velocity, F_p and F_n are positive constants, $\Phi(\cdot)$ is a continuous function that satisfies $\Phi(0) = 0$, and gsgn is the generalized signum function defined as follows:

$$\mathrm{gsgn}(A, x, B) \triangleq \begin{cases} B & \text{if } x > 0 \\ [A, B] & \text{if } x = 0 \\ A & \text{if } x < 0. \end{cases} \tag{3.2}$$

The function $\Phi(\cdot)$ and the constants F_p and F_n are obtained by the linear interpolation and extrapolation of the sampled velocity-friction force pairs. Figure 3.4(a) shows that, in Setup A, the magnitudes of friction are different in different directions, i.e., $F_p \neq F_n$, and the curve of the rate-dependent friction is almost straight. Figure 3.4(b) shows that, in Setup B, the magnitude of friction is almost symmetric with respect to velocity $v = 0$. This chapter uses the identified F_p, F_n and $\Phi(\cdot)$ in the proposed compensator.

3.3 Conventional Elastoplastic Friction Model

3.3.1 Details

Mahvash and Okamura [66] have utilized Hayward and Armstrong's elastoplastic friction model [32] for friction compensation of a tendon-driven joint. Kikuuwe et al. [56] have presented a visco-elastoplastic friction model, which is a generalization of Hayward and Armstrong's model with non-zero viscosity, and they have derived the discrete-time algorithm from the continuous-time representation. Hayward and Armstrong's elastoplastic friction model can be written in Kikuuwe et al.'s manner [56] as follows:

$$K(p-q) \in F\mathrm{sgn}(\dot{q}) \tag{3.3a}$$

$$f = K(p-q) \tag{3.3b}$$

where p is the input position, q is the internal state variable representing the position of the Coulomb friction element, K is the compliance, and F is the magnitude of Coulomb friction force. The output f is the force balancing with the spring force $K(p-q)$. Here, function $\mathrm{sgn}(x)$ is the set-valued function defined as follows:

$$\mathrm{sgn}(x) \triangleq \begin{cases} x/|x| & \text{if } x \neq 0 \\ [-1,1] & \text{if } x = 0 \end{cases} \tag{3.4}$$

where the function sgn(·) possesses the following property:

$$\mathrm{sgn}(\kappa x) = \mathrm{sgn}(x) \quad \forall \kappa > 0. \tag{3.5}$$

By using the backward Euler method, (3.3a) is discretized as follows:

$$K(p_k - q_k) \in F\mathrm{sgn}\left(\frac{q_k - q_{k-1}}{T}\right) \tag{3.6}$$

where k denotes the discrete-time index, and T is the sampling interval. The solution of

(3.6) with respect to q_k can be obtained through the following relation:

$$y \in \mathrm{sgn}(x-y) \Leftrightarrow y = \mathrm{sat}(x) \tag{3.7}$$

where the function $\mathrm{sat}(x)$ is defined as follows:

$$\mathrm{sat}(x) \triangleq \begin{cases} x/|x| & \text{if } |x| > 1 \\ x & \text{if } |x| \leq 1. \end{cases} \tag{3.8}$$

The proof of the relation (3.7) is provided as follows [52, 54, 96]:

$$\begin{aligned} & y \in \mathrm{sgn}(x-y) \Leftrightarrow (y = (x-y)/|x-y| \wedge x \neq y) \vee (y = x \wedge |y| \leq 1) \\ & \Leftrightarrow (y = x/(1+|x-y|) \wedge x \neq y \wedge |y| = 1) \vee (y = x \wedge |x| \leq 1) \\ & \Leftrightarrow (y = x/(1+|x-y|) \wedge |x| = 1 + |x-y| > 1) \vee (y = x \wedge |x| \leq 1) \\ & \Leftrightarrow (y = x/|x| \wedge |x| > 1) \vee (y = x \wedge |x| \leq 1) \Leftrightarrow y = \mathrm{sat}(x) \qquad \square \end{aligned} \tag{3.9}$$

The derivation process to solve (3.6) is shown as follows:

$$K(p_k - q_k) \in F\mathrm{sgn}\left(\frac{q_k - q_{k-1}}{T}\right) \tag{3.10a}$$

$$\Leftrightarrow \frac{K}{F}(p_k - q_k) \in \mathrm{sgn}\left(\frac{K}{F}(p_k - q_{k-1}) - \frac{K}{F}(p_k - q_k)\right) \tag{3.10b}$$

$$\Leftrightarrow \frac{K}{F}(p_k - q_k) = \mathrm{sat}\left(\frac{K}{F}(p_k - q_{k-1})\right) \tag{3.10c}$$

$$\Leftrightarrow q_k = p_k - \frac{F}{K}\mathrm{sat}\left(\frac{K}{F}(p_k - q_{k-1})\right) \tag{3.10d}$$

In conclusion, a discrete-time algorithm to obtain the output force of model (3.3) is represented as follows:

$$q_k = p_k - \frac{F}{K}\mathrm{sat}\left(\frac{K}{F}(p_k - q_{k-1})\right) \tag{3.11a}$$

$$f_k = K(p_k - q_k). \tag{3.11b}$$

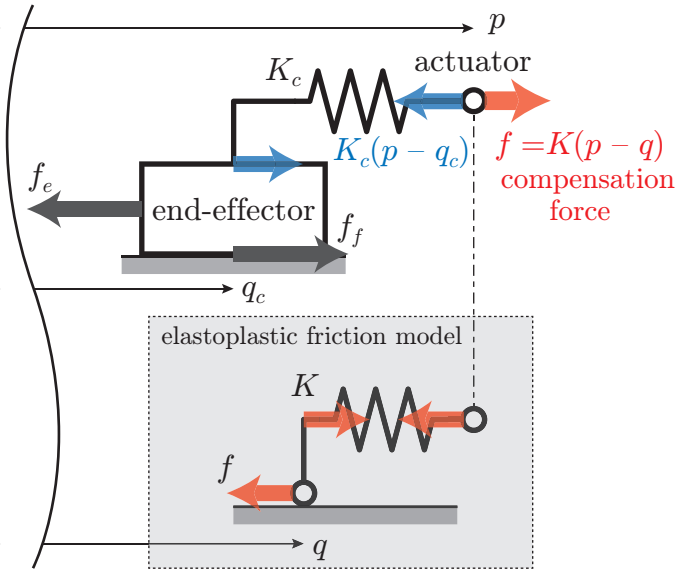

Figure 3.5: Diagram of an elastic joint and elastoplastic friction model.

Mahvash and Okamura [66] have utilized the above model as a friction compensator for an elastic tendon-driven joint.

3.3.2 Problem in the application to friction compensation

The friction model utilized in the compensator (3.11) is a *stictional* friction model, which has the static friction state. A system including such a compensator reaches an equilibrium where the both of the controlled object and the internal model are in the static friction state at different positions. This indicates that the compensator produces non-zero force in the static friction state.

An actuator system with the elastoplastic friction compensator can be illustrated as Figure 3.5. The equilibrium mentioned above can be considered in Figure 3.5 to be the situation where the position q does not overlap p in the static friction state. This positional relation is not desirable because an external force f_e above the original static friction f_f is required to break away the static friction.

3.4 Proposed Friction Compensator

3.4.1 Main modification: exponentially decaying output force

Here this section presents a new friction compensator that avoids the problem explained in Section 3.3.2. The source of the problem is the dislocated equilibrium between p and q, which results in the continuing non-zero output force f in the static friction. In order to prevent this, we propose a modified version of (3.3) as follows:

$$K(p-q) \in F\mathrm{sgn}\left(\dot{q} + \alpha\left(q-p\right)\right) \tag{3.12a}$$

$$f = K(p-q) \tag{3.12b}$$

where α is a positive constant.

In the compensator (3.12), the additional term $+\alpha(q-p)$ has the effect of preventing the equilibrium at $q - p \neq 0$. Equation (3.12a) can be equivalently rewritten as follows:

$$\begin{aligned}
&((K(p-q) = F) \wedge (\dot{q} + \alpha(q-p) > 0)) \\
&\vee ((|K(p-q)| < F) \wedge (\dot{q} + \alpha(q-p) = 0)) \\
&\vee ((K(p-q) = -F) \wedge (\dot{q} + \alpha(q-p) < 0))\,,
\end{aligned} \tag{3.13}$$

which can be further rewritten as follows:

$$\begin{aligned}
&((\dot{q} > \alpha F/K) \wedge (K(p-q) = F)) \\
&\vee ((\dot{q} = -\alpha(q-p)) \wedge (|K(p-q)| < F)) \\
&\vee ((\dot{q} < -\alpha F/K) \wedge (K(p-q) = -F))\,.
\end{aligned} \tag{3.14}$$

This implies that, when $K(p-q) = f \in (-F, F)$, i.e., when the compensator is in the static friction state, q exponentially converges to p and the parameter α determines the rate of convergence. Meanwhile, when $K(p-q) = f$ is either $+F$ or $-F$, i.e., when the compensator is in the kinetic friction state, the velocity $\dot{q}$ is larger than $\alpha F/K$. That is, the parameter α determines the threshold value $\alpha F/K$ above which the compensator produces

a constant force. The former effect indeed prevents the dislocated equilibrium at $p \neq q$ although the latter effect is not what we exactly intended.

Here the algorithm of the compensator is derived based on the simultaneous differential equations (3.12). The backward Euler discretization of (3.12a) can be written as follows:

$$K(p_k - q_k) \in F\mathrm{sgn}\left(\frac{q_k - q_{k-1}}{T} + \alpha\left(q_k - p_k\right)\right), \tag{3.15}$$

which is equivalent to

$$\frac{K}{F}(p_k - q_k) \in \mathrm{sgn}\left(\frac{K\left(p_k - q_{k-1}\right)}{F\left(1 + T\alpha\right)} - \frac{K}{F}(p_k - q_k)\right). \tag{3.16}$$

By the application of the relation (3.7), one can see that (3.16) is equivalent to the following:

$$\frac{K}{F}(p_k - q_k) = \mathrm{sat}\left(\frac{K\left(p_k - q_{k-1}\right)}{F\left(1 + T\alpha\right)}\right), \tag{3.17}$$

which is equivalent to

$$q_k = p_k - \frac{F}{K}\mathrm{sat}\left(\frac{K\left(p_k - q_{k-1}\right)}{F\left(1 + T\alpha\right)}\right). \tag{3.18}$$

Consequently, the discrete-time algorithm of the proposed friction compensator is written as follows:

$$q_k := p_k - \frac{F}{K}\mathrm{sat}\left(\frac{K\left(p_k - q_{k-1}\right)}{F\left(1 + T\alpha\right)}\right) \tag{3.19a}$$

$$f_k := K(p_k - q_k). \tag{3.19b}$$

3.4.2 Additional modification 1: sinusoidal dither for static friction

Equation (3.12) is not targeted to facilitate breaking away the static friction as seen in the fact that the proposed compensator decays the output force in the static friction state. In order to improve the backdrivability of the system, this chapter employs dither-like sinusoidal signal

represented as follows:

$$f_d(t) = F_d \sin(\omega t) \tag{3.20}$$

where t is time, F_d and ω are the magnitude and the angular frequency of the dither, respectively.

Dither has been originally used to maintain the system in the kinetic friction state under the assumption that the kinetic friction force is smaller than the static friction force. The conventional dither signals are usually high-frequency signals that are slightly greater in magnitude than the static friction force [4]. On the other hand in this chapter, the dither-like signal of which the magnitude is smaller than the static friction force is used to maintain the system on the verge of the static friction state and to make the system sensitive to external force. A similar idea has been presented by Aung et al. [5]. They used a more sophisticated dither-like signal, where the oscillation caused by the dither is only a few counts of the encoder steps in the both of the positive and negative direction.

In the case of Setup A, a sinusoidal dither actuation such as the top of Figure 3.6 causes the displacement in two counts of the encoder steps in each direction as shown in the bottom of Figure 3.6. This oscillation makes the system on the verge of the static friction and sensitive to external force.

3.4.3 Additional modification 2: direction-dependent Coulomb friction force and rate-dependent friction force

The compensator (3.19) is built on the assumption that the device friction is the pure Coulomb friction, that is, $f = F\mathrm{sgn}(v)$. For cases where the friction force is direction- and rate-dependent as in (3.1) and Figure 3.4, the compensator (3.12) should be slightly generalized as follows:

$$q_k = p_k - \frac{1}{K}\mathrm{gsat}\left(-F_n, \frac{K(p_k - q_{k-1})}{1 + T\alpha}, F_p\right) \tag{3.21a}$$

$$f = K(p_k - q_k) + \Phi\left(\frac{q_k - q_{k-1}}{T}\right) \tag{3.21b}$$

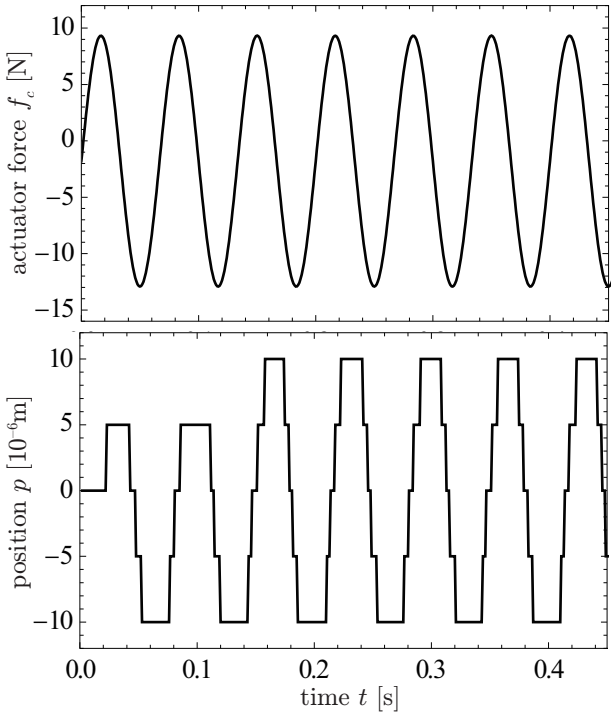

Figure 3.6: Displacement caused by a sinusoidal dither actuation.

where F_p and F_n are the magnitudes of Coulomb friction force with respect to the direction defined in Section 3.2.3, and the function gsat is defined as follows:

$$\mathrm{gsat}(A, x, B) \triangleq \begin{cases} B & \text{if } x > B \\ x & \text{if } x \in [A, B] \\ A & \text{if } x < A. \end{cases} \tag{3.22}$$

Equation (3.21a) is obtained by solving

$$K(p - q) \in \mathrm{gsgn}\left(-F_n, \dot{q} + \alpha\,(q - p)\,, F_p\right) \tag{3.23}$$

using the following relations:

$$\mathrm{gsgn}(A, \kappa x, B) = \mathrm{gsgn}(A, x, B) \quad \forall \kappa > 0 \tag{3.24}$$

$$y \in \mathrm{gsgn}(A, x - y, B) \Leftrightarrow y = \mathrm{gsat}(A, x, B) \tag{3.25}$$

in a process with discretization similar to that to obtain (3.19). Moreover, in order to handle the different magnitudes of Coulomb friction, the dither friction compensator (3.20) has been modified as follows:

$$f_d(t) = R_d \left(\frac{F_p + F_n}{2} \sin(\omega t) + \frac{F_p - F_n}{2} \right) \tag{3.26}$$

where R_d is a constant for adjusting the magnitude of the dither.

The performance of the algorithm (3.21) cannot be very sensitive to the choice of the time-step size T because both functions gsat and Φ are continuous and therefore the algorithm does not include any discontinuities. The parameter α should be selected according to the required convergence rate of the compensation force. Note that α is not a model parameter of the controlled object, but a design parameter that should be selected according to the purpose of applications.

3.4.4 Algorithm

In order to deal with the property that can be seen in Figure 3.3 and 3.4, the proposed compensator has been combined with the dither friction compensator and the function of the rate-dependent friction. While dither helps breaking away the static friction, it disturbs the motion or causes oscillation in the kinetic friction state, so that dither should be turned off in such a state.

Taking account of the mentioned above, the algorithm of the friction compensator is constructed as follows:

$$\text{Function } \mathbf{algFC}(p_k, \alpha) \tag{3.27a}$$

$$f_m^* := \frac{K(p_k - q_{k-1})}{1 + T\alpha} \tag{3.27b}$$

$$q_k := p_k - \frac{1}{K}\mathrm{gsat}(-F_n, f_m^*, F_p) \tag{3.27c}$$
$$f_m := K(p_k - q_k) \tag{3.27d}$$
$$\text{If } -F_n < f_m^* < F_p \tag{3.27e}$$
$$f_d := R_d\left(\frac{F_p + F_n}{2}\sin(\Omega_d t) + \frac{F_p - F_n}{2}\right) \tag{3.27f}$$
$$\text{Else} \tag{3.27g}$$
$$f_d := 0 \tag{3.27h}$$
$$\text{Endif} \tag{3.27i}$$
$$f := f_m + f_d + \Phi((q_k - q_{k-1})/T) \tag{3.27j}$$
$$\text{Return } f. \tag{3.27k}$$

3.5 Experiments

The proposed method was tested with Setup A and Setup B, which are shown in Figure 3.1. In these experiments, the following five cases were compared:

- **NC**: no compensation,
- **C**: the compensator **algFC** in (3.27) with $\alpha = 0$ without dither (i.e., $R_d = 0$). It is a trivial extension of the conventional Mahvash and Okamura's compensator.
- **CD**: **C** with dither.
- **P**: the compensator **algFC** in (3.27) with $R_d = 0$, i.e., the proposed method without dither.
- **PD**: the proposed compensator **algFC** in (3.27).

Throughout all experiments in this chapter, the sampling interval was set as $T = 0.001$ s.

3.5.1 Setup A

In this experiment, the experimenter grasped the grip attached on the tip of the force sensor of Setup A and moved the end-effector with the above five cases. Marks were put on the setup so that the experimenter moves the end-effector with as close displacement as

possible in all the cases. The experimenter tried to move the end-effector as the position trajectory draws square wave-like form with 30 cycles, being paced by a metronome with the frequency 0.667 Hz.

The parameters F_p and F_n and the function $\Phi(\cdot)$ were identified as shown in Section 3.2.3. Other parameters were determined as follows. The compliance K was set as $K = 1.2 \times 10^6$ N/m, which is close to the elasticity of the setup that can be obtained through a close observation of the graph of Figure 3.3. The constant α was set as $\alpha = 20.0$ s^{-1}, which is selected so that the convergence of q_k to p_k is reasonably quick. The frequency of dither ω was chosen as $\omega = 15.0 \times 2\pi$ rad/s, which is larger than the frequency of human motion, assuming that external force is applied by a human hand. The constant R_d was set to be 1.0.

Most part of the experimental results is shown in Figure 3.7(a). In this figure, it seems that the peak values of the external force are smaller in the case with **PD** through this experiment. To observe in detail, one part of the experimental results is focused as shown in Figure 3.7(b). It can be seen that the peaks of measured external force are smallest in the case of **PD**. Note that the measured force magnitudes are different with respect to the direction of motion. This can be considered to be due to the difference of the device friction and the compensation force with respect to the direction.

In the cases of **C** and **CD**, the force peaks appear at each velocity reversal, where the actuator produces the compensation force opposite to the direction in which experimenter applied force. One can also see that the velocity peaks in the case of **C** is larger than the cases of **CD**, **P** and **PD**. It can be considered that the large velocity peaks were caused by the drastic reversal of the direction of the compensation force.

The measured external force in the five cases was quantitatively validated by taking averages and standard deviations of the peak values with respect to the direction of motion in each case. Each peak value was taken from a range with a constant interval 1.5 s as shown by the dashed lines in the bottom of Figure 3.7(b). Figure 3.8 shows the result. This figure displays that the average value is smallest in the case of **PD** where the proposed compensator (3.21) and the dither (3.26) worked. It can be seen that the force is smaller in the case with dither by comparing the cases between **P** and **PD**, or **C** and **CD**. Note that the

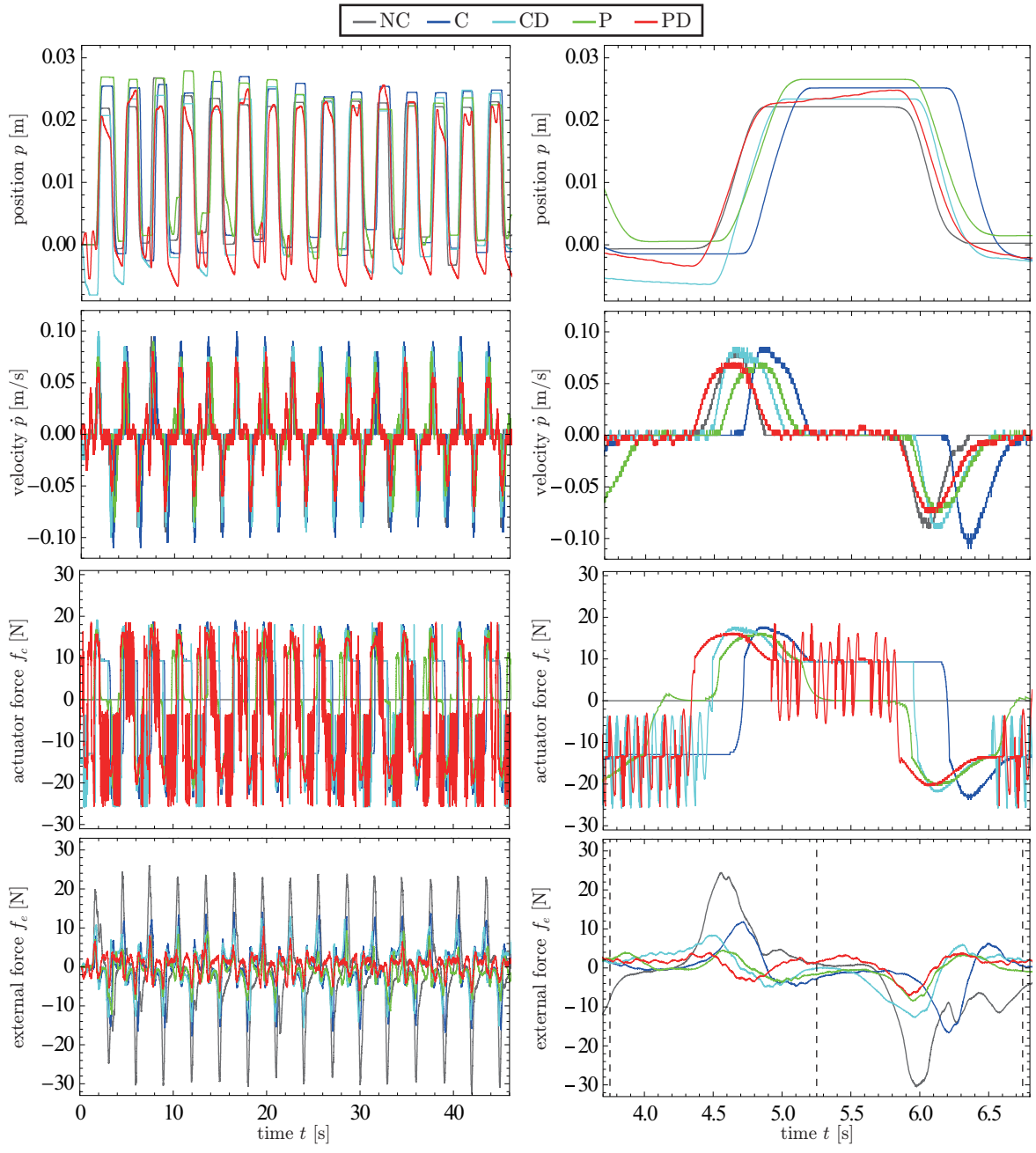

(a) Most part (b) One part

Figure 3.7: Experimental results, Setup A.

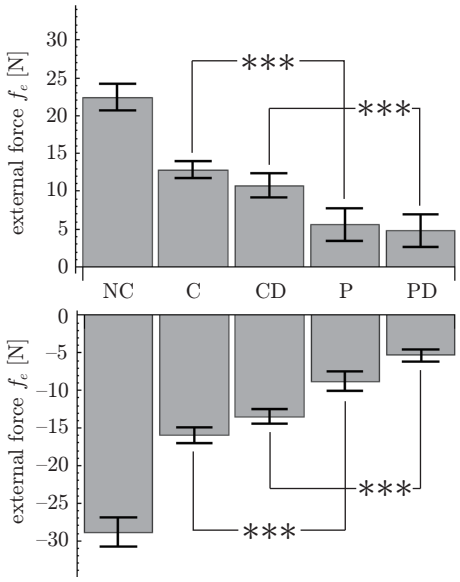

Figure 3.8: Averages and standard deviations of the peak values of the measured external force, Setup A. The triple asterisk ('***') stands for the significant difference at $p < 0.1\%$ according to Student's t-test.

average values and the standard deviations of the force peaks are different in each direction due to the difference of the friction and compensation force.

3.5.2 Setup B

In the experiment using Setup B, the experimenter grasped the grip on the force sensor and intended to cyclically move it in a square-shaped trajectory in the x-y plane, being paced by a metronome with the frequency 0.667 Hz. The parameters were chosen as: $K = 50000$ Nm/rad, $F_p = F_n = 6.85, 9.56, 3.15$ Nm for each joint, $\alpha = 20$ s^{-1}, $\Omega_d = 30\pi$ rad/s and $R_d = 0.3$.

Figure 3.9 and 3.10 show the results. As a whole, these figures show the same features as the results from Setup A; the average value is smallest in the case **PD** where the proposed compensator (3.27) with the dither was used.

From the above results, we can say that the external force required for moving the end-effector is smallest in the case of **PD**. In conclusion, it can be said that the proposed method

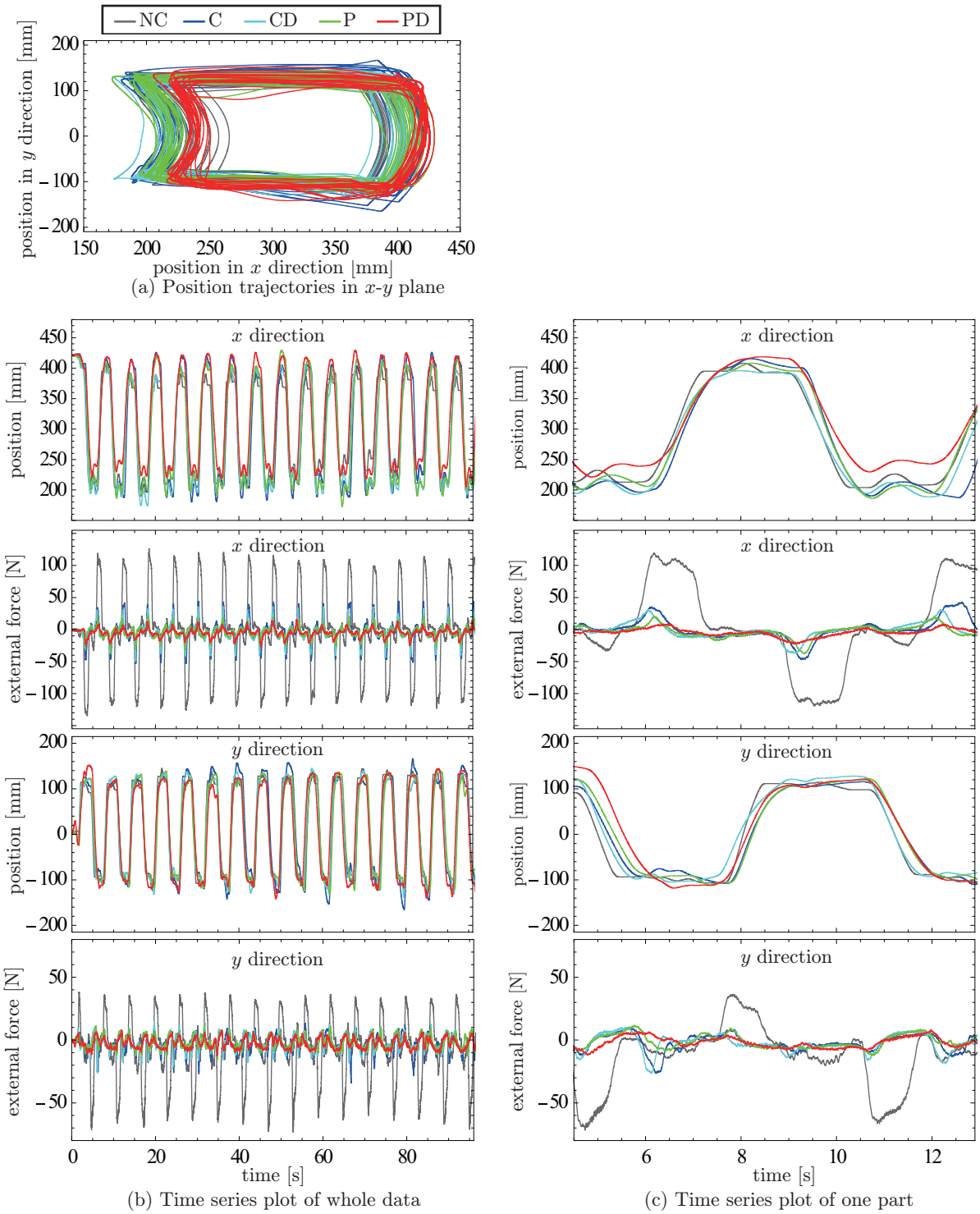

(a) Position trajectories in x-y plane

(b) Time series plot of whole data

(c) Time series plot of one part

Figure 3.9: Experimental results, Setup B.

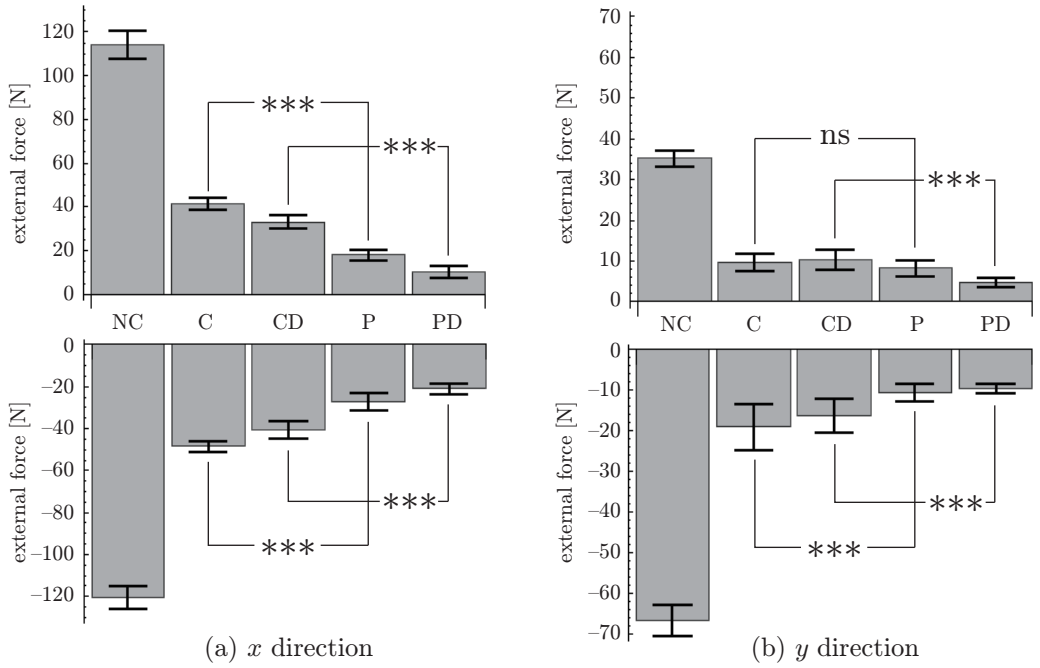

(a) x direction (b) y direction

Figure 3.10: Averages and standard deviations of the peak values of the measured external force in each direction, Setup B. The triple asterisk ('***') and 'ns' stand for the significant difference at $p < 0.1\%$ and no significant difference, respectively, according to Student's t-test.

enhances the backdrivability of the setups.

3.6 Further Improvement for 'Hand-Drivabilization'

3.6.1 Additional algorithm for on-line adjustment of α

Considering applications in which the robot is 'hand-driven,' i.e., is moved by hand, a perfect friction compensation is not always beneficial because it causes unnecessary fluctuation of the robot motion especially when the user intends to stop the motion. In such an application, the friction should be appropriately compensated when the user intends to start moving, but the friction compensation should be weakened when the motion slows down.

As has been briefly explained in Section 3.4.1, the output force decays at the rate α

when the velocity is smaller than $\alpha F/K$. For the static friction state, α should be a nominal value to realize an appropriate friction compensation, but in the kinetic friction state, the compensation force should decay quickly once the speed is sufficiently small. Based on this observation, this chapter proposes a new algorithm to adjust α in realtime, specifically for the 'hand-drivabilization.' This algorithm is a simple extension of the algorithm **algFC** as follows:

$$\begin{aligned}
&\text{Function } \mathbf{algFC2}(p_k) && \text{(3.28a)}\\
&\quad \text{If } |(p_k - p_{k-1})/T| > V_W && \text{(3.28b)}\\
&\quad\quad w_k := \max(w_{k-1} + R_W, 1) && \text{(3.28c)}\\
&\quad \text{Else} && \text{(3.28d)}\\
&\quad\quad w_k := \min(w_{k-1} - R_W, 0) && \text{(3.28e)}\\
&\quad \text{Endif} && \text{(3.28f)}\\
&\quad \alpha := (1 - w_k)\alpha_N + w_k\alpha_H && \text{(3.28g)}\\
&\text{Return } \mathbf{algFC}(p_k, \alpha). && \text{(3.28h)}
\end{aligned}$$

Here, α_N is the nominal value of α, which has been used for the non-adaptive cases, α_H is a value that is much higher than α_N. The constant R_W determines the rate of change of α. The constant V_W is a threshold velocity below which α is decreased and above which increased. This algorithm is intended to avoid discontinuities in the change of α.

3.6.2 Experiments

The algorithm **algFC2** in (3.28) was tested with the two devices, Setup A and Setup B. In the both setups, the parameters were set at $\alpha_N = 20$ s^{-1} (which is the same value as in the experiments in Section 3.5), $\alpha_H = 500$ s^{-1} and $R_W = 0.01$. The value of α_N is chosen so that q_k converges to p_k reasonably quickly (in the experiments in Section 3.5), α_H is chosen to be sufficiently larger than α_N, and R_W is chosen so that the transitions between $\alpha = \alpha_N$ and α_H take place sufficiently quickly. The velocity threshold was set at $V_W = 0.01$ m/s in Setup A and $V_W = 0.005$ rad/s in Setup B. The dither magnitude parameter was set as

$R_d = 0.5$ in Setup A and $R_d = 0.2$ in Setup B, which are lower than those in Section 3.5 because, in an application of the 'hand-drivabilization,' a certain level of friction should be left uncompensated to suppress unnecessary fluctuation. The other parameters were set the same as in Section 3.5.

The following three cases were compared: $\alpha \equiv \alpha_N$, $\alpha \equiv \alpha_H$, and the case with the proposed algorithm **algFC2** in (3.28) with the varying α. With each of the Setup A and Setup B, the experimenter grasped the grip of the end-effector of the setup, and moved it from a point to another point. With Setup B, only the joint 0 was used and the other joints were locked by local angle controllers.

The results with Setup A and B are shown in Figure 3.11. Figure 3.11(a) and Figure 3.11(b) show mostly the same features. With the proposed algorithm **algFC2**, the force peaks were smaller than the other cases and the joint eventually came to stationary. This is in contrast to the case of the nominal α ($\alpha \equiv \alpha_N$), with which the fluctuation continued, and also to the case with the high α ($\alpha \equiv \alpha_H$), with which the force peaks were larger.

3.7 Summary

This chapter has presented an elastoplastic friction compensator with improved static friction behavior. The proposed compensator decays the compensation force in the static friction state by making the internal state variable converge to the input position. The proposed method has been combined with a dither friction compensator and a function of rate-dependent friction. Experimental validation has shown that the proposed method makes the external force smaller for moving the joints of the setups. This indicates that the proposed method enhances the backdrivability of the systems. An algorithm adjusting the decay rate of the friction compensator online has also been presented for the further improvement for an application where robotic joints are moved by a human hand.

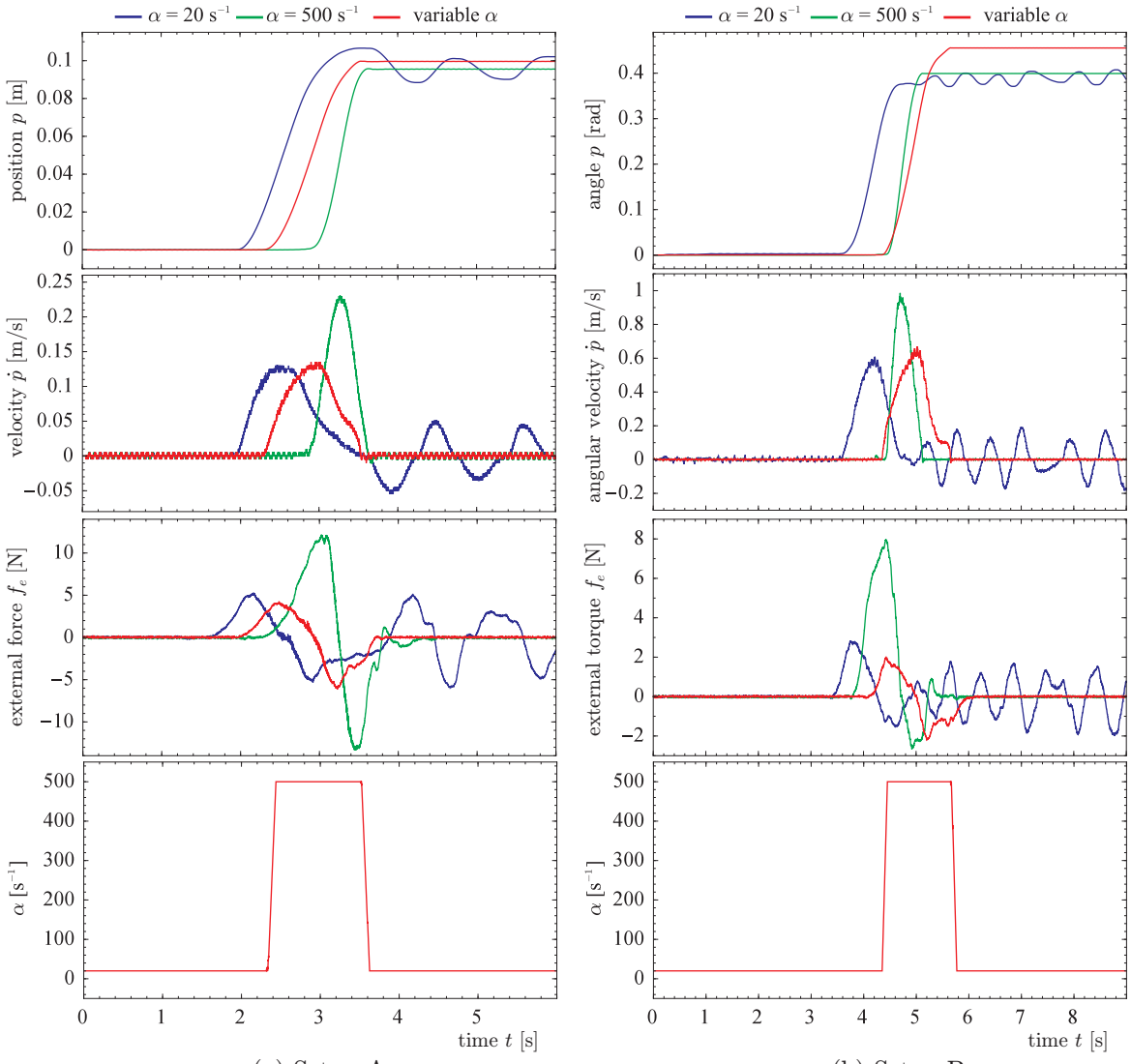

(a) Setup A (b) Setup B

Figure 3.11: Experimental result of friction compensation.

Chapter 4

Estimation of Joint Friction Force: Elastoplastic Friction Force Estimator for External Force Estimation

4.1 Introduction

Estimating joint friction of robotic systems, not compensating the friction, is also important. What is required for the friction force estimation is only position sensors such as encoders, and in some cases, only estimating the friction is beneficial. One application of estimation of joint friction force is external force estimation in which force acting on a robot is estimated based on the equation of motion that includes a joint friction term. This technique is useful in situation where robots make interaction with external environments, and can eliminate the necessity for force sensors, which are fragile and expensive.

The relation between the motion of a robot and the forces acting on the robot is represented by the equation of motion based on the inertia and the forces. In the case of an

★ The content of this chapter is partially published in [41], namely, M. Iwatani and R. Kikuuwe. An External Force Estimator Using Elastoplastic Friction Model With Improved Static Friction Behavior. In *Proceedings of 14th International Conference on Control, Automation, Robotics and Vision*, Tu42.6, 2016. and in [39], namely, M. Iwatani and R. Kikuuwe. An Elastoplastic Friction Force Estimator and Its Application to External Force Estimation and Force-Sensorless Admittance Control. In *Proceedings of the 2016 IEEE/SICE International Symposium on System Integration*, pages 45–50, 2016.

actuator system of one degree of freedom especially, the equation is constructed by the inertia term, the actuator force, the friction force and the external force, with assuming that the gravity force can be ignored by the configuration of the system or applying gravity compensation. In such a situation, the external force can be estimated by calculating values of the inertia force, the actuator force and the friction force.

The accuracy of external force estimation largely depends on the accuracy of the friction term. Katsura et al. [48] have proposed an external force estimation method based on a disturbance observer with Coulomb and viscous friction model. Kamezaki et al. [47] have proposed an external force estimation method using Coulomb and viscous friction model for a hydraulic-driven constructing manipulator. Because Coulomb friction model includes discontinuity, implementation of such a model needs a modification as setting a dead zone, which is a cause of the estimation error.

Besides the Coulomb friction model, many friction models have been proposed. One of simplest models is perhaps Hayward and Armstrong's elastoplastic friction model [32], which is constructed by a serial connection of a Coulomb friction element and a compliant element. Dupont et al. [21] have proposed an extended model with a refined presliding behavior. Kikuuwe et al.'s visco-elastoplastic friction model [56] is a generalization of Hayward and Armstrong's model with non-zero viscosity. Xiong et al. [96] have presented a multi-state friction model, which consists of a parallel connection of visco-elastoplastic elements.

As far as the author is aware, elastopalstic friction models have not been employed for external force estimation despite their advantages to representing friction phenomena. There is one drawback of straightforward application of the elastoplastic friction model to external force estimation. The drawback is that the elastoplastic friction model continues producing non-zero output force in the static friction state. This non-zero output force causes steady-state error in external force estimation.

This chapter proposes a new friction force estimator with improved static friction behavior. The estimator is inspired by the friction compensator proposed in Chapter 3 for friction compensation of robotic joints including compliant mechanisms. This chapter shows the proposed estimator is advantageous compared with a Coulomb friction model and a conven-

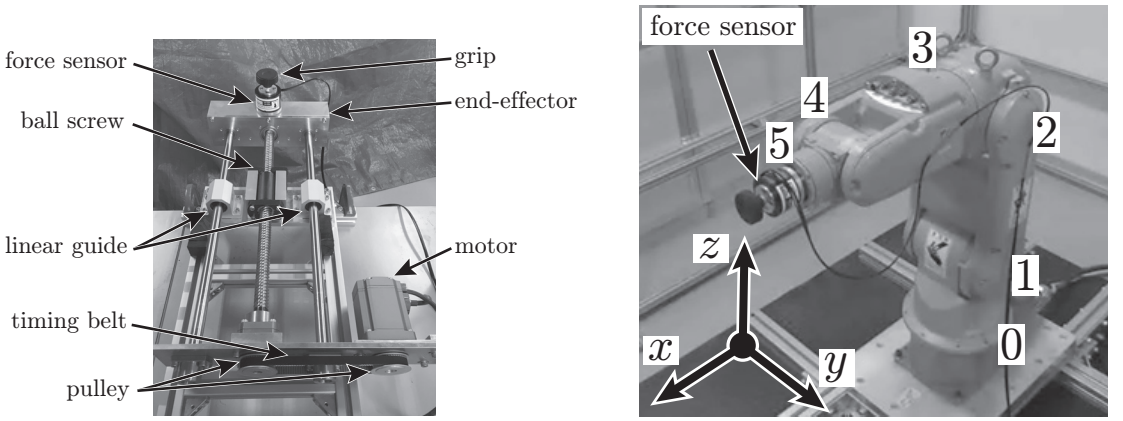

(a) Setup A: Linear Actuator (b) Setup B: Yaskawa MOTOMAN-HP3J

Figure 4.1: Experimental setups.

tional elastoplastic friction model.

The proposed method was validated using a linear actuator system with a ball screw and a six-axis industrial manipulator. It is shown that the proposed estimator softens the problem mentioned above, i.e., the proposed estimator is convenient for external force estimation more than a simple Coulomb friction model and a conventional elastoplastic friction model.

The reminder of this chapter is organized as follows. Section 4.2 describes the experimental setup. Section 4.3 proposes the external force estimator. Section 4.6 shows experimental validation of the proposed estimator. Section 4.7 presents a further improved algorithm for admittance control, and also shows some experimental results. Section 4.8 provides concluding remarks.

4.2 Experimental Setups

4.2.1 Overview

Here, an overview of an experimental setups used in this chapter is provided. Figure 4.1 shows the setups. The Setup A (Figure 4.1(a)) is composed of an AC servo motor integrated with an optical encoder, a ball screw, linear guides, pulleys and a timing belt. The end-

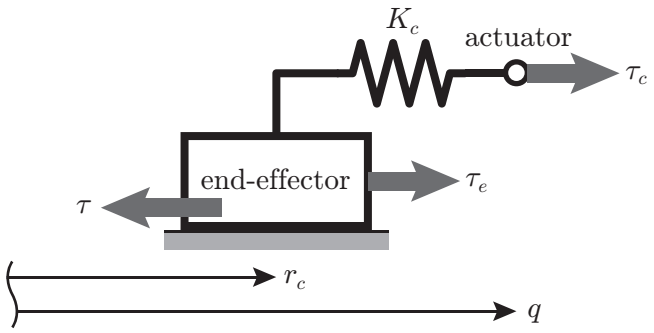

Figure 4.2: Schematic illustration of each joint of the setups.

effector is connected to the actuator through a compliant transmission (the timing belt). The Setup B (Figure 4.1(b)) is a six-axis industrial manipulator MOTOMAN-HP3J produced by Yaskawa Electric Corporation. In each joint of Setup B, an AC servo motor, an optical encoder and a harmonic drive transmission are embedded, where the transmission has compliance. For these setups, there is joint friction on the side of the end-effector rather than on the side of the actuator. Because the encoder is attached to the actuator, the position of the end-effector cannot be measured directly.

The schematic illustration of each joint of the setups can be drawn as Figure 4.2. Here, q and r_c are the position of the actuator and the end-effector, respectively, K_c is the compliance of the elastic element, τ is the joint friction force acting on the side of the end-effector, and τ_e is external forces on the end-effector. The force acting on the end-effector is transmitted to the actuator through the elastic element.

4.2.2 Rate-dependent friction

Rate-dependent friction in the joints of the setups was investigated by the identification procedure proposed in Chapter 2 with a slight change for handling different magnitudes of friction with respect to the direction of motion. The identification results are shown in Figure 4.3. Each point is a sampled velocity-friction force pair, and the points are connected by the linear interpolation and extrapolation.

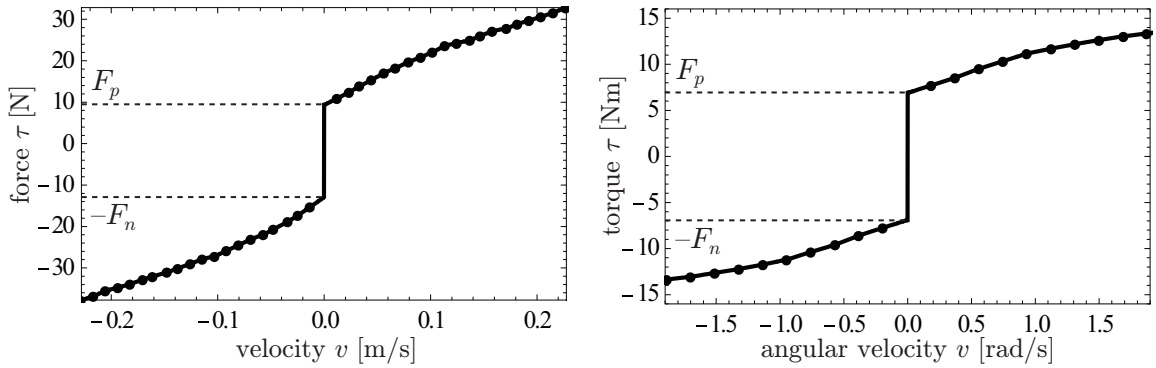

(a) Setup A (b) Joint 0 of Setup B

Figure 4.3: Identification result of rate-dependent friction.

The curves in Figure 4.3 can be described by the following form:

$$f \in \mathrm{gsgn}(-F_n, v, F_p) + \Phi(v) \tag{4.1}$$

where v is the velocity, F_p and F_n are positive constants, $\Phi(\cdot)$ is a continuous function that satisfies $\Phi(0) = 0$, and gsgn is the generalized signum function, which is defined as (3.2) in Chapter 3. Here, F_p and F_n are the intercepts of the curves, and $\Phi(\cdot)$ is obtained by subtracting the values of F_p and F_n from each pairs. In Setup A as shown in Figure 4.3(a), the magnitudes of the friction are different with respect to the direction, i.e., $F_p \neq F_n$, and the rate-dependent friction is almost linear. In Setup B as shown in Figure 4.3(b), the curve is almost symmetric with respect to velocity $v = 0$. Identified F_p, F_n and $\Phi(\cdot)$ are used in the proposed estimator.

4.3 Applications of Friction Force Estimator

This chapter discuses applications of a friction force estimator to external force estimation and force-sensorless admittance control. This section describes the framework of the external force estimation and the force-sensorless admittance control.

4.3.1 External force estimation

The equation of motion of the setups are constructed as follows:

$$\boldsymbol{M}(\boldsymbol{q})\ddot{\boldsymbol{q}} + \boldsymbol{h}(\boldsymbol{q}, \dot{\boldsymbol{q}}) + \boldsymbol{g}(\boldsymbol{q}) + \boldsymbol{\tau}(\boldsymbol{q}, \dot{\boldsymbol{q}}) = \boldsymbol{\tau}_c + \boldsymbol{\tau}_e \tag{4.2}$$

where $\boldsymbol{q} \in \mathbb{R}^n$ is the joint position/angle vector, $\boldsymbol{M}(\boldsymbol{q}) \in \mathbb{R}^{n\times n}$ is the inertia matrix, $\boldsymbol{h}(\boldsymbol{q}, \dot{\boldsymbol{q}}) \in \mathbb{R}^n$ is the Coriolis and centrifugal term, $\boldsymbol{g}(\boldsymbol{q}) \in \mathbb{R}^n$ is the gravity term, $\boldsymbol{\tau}_c \in \mathbb{R}^n$ is the control force/torque vector, $\boldsymbol{\tau}_e \in \mathbb{R}^n$ is the force/torque with respect to each joint by the external force, and $\boldsymbol{\tau}(\boldsymbol{q}, \dot{\boldsymbol{q}}) \in \mathbb{R}^n$ is the friction force of the joints. In Setup A, which is a one degree of freedom actuator, the Coriolis and centrifugal term is neglected, i.e., $\boldsymbol{h}(\boldsymbol{q}, \dot{\boldsymbol{q}}) \equiv 0$, and the gravity term also can be ignored by the configuration, i.e., $\boldsymbol{g}(\boldsymbol{q}) \equiv 0$. Therefore, for Setup A, (4.2) can be simply rewritten as follows:

$$M\ddot{q} + \tau = \tau_c + \tau_e \tag{4.3}$$

where $M \in \mathbb{R}$ is the inertia, and q, τ_c, τ_e and $\tau \in \mathbb{R}$ are the position, the actuator force, the external force and the friction force, respectively.

Based on (4.2), the external force can be estimated as follows:

$$\hat{\boldsymbol{\tau}}_e = \hat{\boldsymbol{M}}(\boldsymbol{q})\ddot{\hat{\boldsymbol{q}}} + \hat{\boldsymbol{h}}(\boldsymbol{q}, \dot{\boldsymbol{q}}) + \hat{\boldsymbol{g}}(\boldsymbol{q}) + \hat{\boldsymbol{\tau}} - \boldsymbol{\tau}_c \tag{4.4}$$

where $\hat{\boldsymbol{\tau}}$ is force obtained from a friction force estimator. Note that the acceleration term $\ddot{\boldsymbol{q}}$ is replaced by $\ddot{\hat{\boldsymbol{q}}}$. The description $\ddot{\hat{\boldsymbol{q}}}$ is intended to indicate the filtered value of $\ddot{\boldsymbol{q}}$. The acceleration signal $\ddot{\boldsymbol{q}}$ is generally noisy, because it is obtained by the second order derivative of the encoder signal $\boldsymbol{q}$. In order to smoothen the acceleration signal, a noise reduction sliding mode filter [53] is utilized during the differentiation from $\boldsymbol{q}$. The property of this filter is determined by two parameters $G > 0$ and $H > 1$. Note that for Setup A, (4.4) is rewritten as follows:

$$\hat{\tau}_e = \hat{M}\ddot{\hat{q}} + \hat{\tau} - \tau_c. \tag{4.5}$$

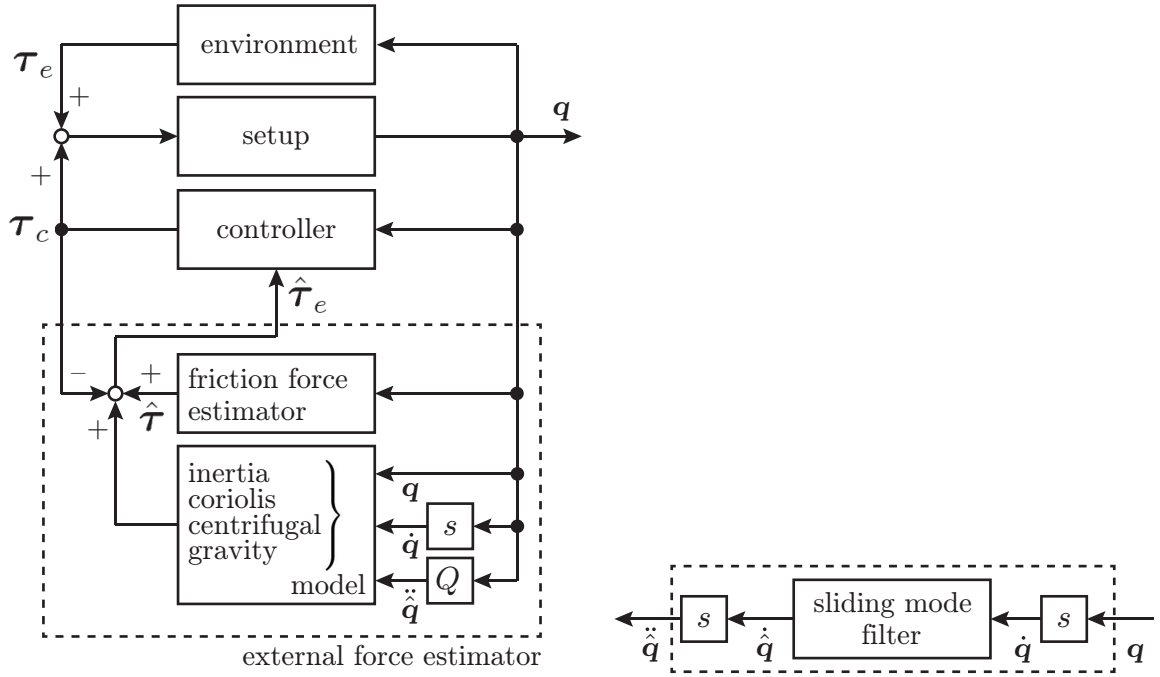

(a) Whole system. (b) Details of Q in (a).

Figure 4.4: Block diagram of a system including external force estimator (4.4).

Figure 4.4 shows the block diagram of the system containing the external force estimator. The accuracy of the external force estimation highly depends on the accuracy of the friction force estimator.

4.3.2 Admittance control

The admittance control scheme used in this chapter includes the external force estimation mentioned above, which contains a friction force estimator, and the scheme is constructed by a virtual object dynamics and a PD position controller as follows:

$$\ddot{q}_d = \frac{\hat{\tau}_e - b\dot{q}_d}{m} \tag{4.6a}$$

$$\tau_c = K_p(q_d - q) + K_d(\dot{q}_d - \dot{q}) \tag{4.6b}$$

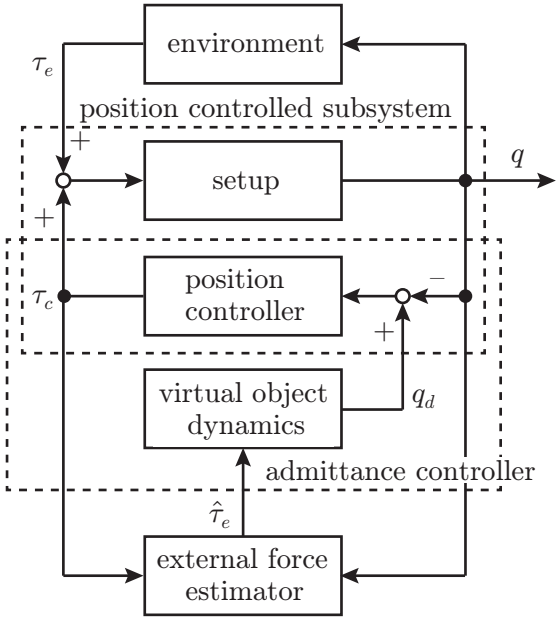

Figure 4.5: Block diagram of a system controlled by the admittance controller (4.6) with the external force estimator. It is assumed that the admittance controller is applied to each joint independently.

where $\tau_c \in \mathbb{R}$ is the output force/torque, $\hat{\tau}_e \in \mathbb{R}$ is the estimated external force/torque as the input, $q_d \in \mathbb{R}$ is the desired position/angle, $q \in \mathbb{R}$ is the input position/angle, and K_p and $K_d \in \mathbb{R}$ are the proportional and derivative gains of the PD controller, respectively. The constants m and $b \in \mathbb{R}$ are the inertia and the viscosity of the virtual object. Note that it is assumed that the admittance controller is applied to each joint of robots independently.

4.4 Conventional Elastoplastic Friction Model

4.4.1 Overview

Hayward and Armstrong's elastoplastic friction model [32] is constructed by a serial connection of a Coulomb friction element and a compliant element. As shown in Section 3.3, Hayward and Armstrong's elastoplastic friction model can be written in Kikuuwe et al.'s

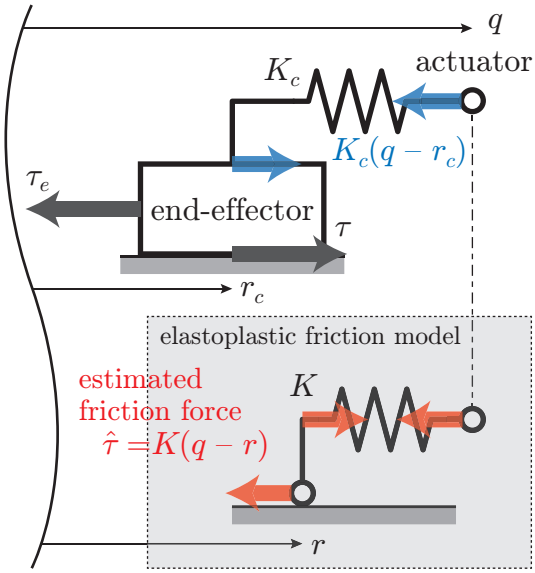

Figure 4.6: Schematic illustration of the setup and an elastoplastic friction model.

manner [56] as follows:

$$K(p - q) \in F\mathrm{sgn}(\dot{q}) \tag{4.7a}$$

$$\hat{\tau} = K(q - r) \tag{4.7b}$$

where q is the input position, r is the internal state variable that represents the position of the Coulomb friction element, K is the compliance, F is the magnitude of Coulomb friction force. The output $\hat{\tau}$ is the force balancing with the spring force $K(q - r)$. Here, function $\mathrm{sgn}(\cdot)$ is the set-valued function defined as (3.4) in Chapter 3. A discrete-time algorithm to obtain the output force of model (4.7) is represented as follows:

$$r_k = q_k - \frac{F}{K}\mathrm{sat}\left(\frac{K}{F}(q_k - r_{k-1})\right) \tag{4.8a}$$

$$\hat{\tau}_k = K(q_k - r_k) \tag{4.8b}$$

where the definition of the function $\mathrm{sat}(\cdot)$ and the details of the derivation are shown in Section 3.3.

4.4.2 Problem in the application to external force estimation

The friction model (4.7a) is a $stictional$ friction model, which has the static friction state. When the input position is constant, such a model reaches an equilibrium where the both of the controlled object and the internal model are in the static friction state at different positions. This indicates that the model produces non-zero output force in the static friction state. Usage of this model for external force estimation causes steady-state error on the estimated force.

The relation of joints of the setups and the friction model can be illustrated as Figure 4.6. The equilibrium mentioned above can be considered to be the situation where the position r does not coincide on q in the static friction state. This positional relation is not desirable because the estimated friction force caused by the displacement results in estimation error of the external force.

4.5 Proposed Friction Force Estimator

In order to resolve the problem mentioned above, (4.7) must be modified so that r converges to q in the static friction state. For achieving this, this chapter proposes a new friction force estimator as follows:

$$K(q-r) \in F\mathrm{sgn}\left(\dot{r} + \alpha\left(r-q\right)\right) \tag{4.9a}$$

$$\hat{\tau} = K(q-r). \tag{4.9b}$$

The form of this estimator is the same as the friction compensator (3.12) in Chapter 3.

The behavior of the estimator is described as follows. Under the condition of the static friction state

$$\left|K\left(q-r\right)\right| < F, \tag{4.10}$$

equation (4.9a) implies the following equation:

$$\dot{r} + \alpha\left(r-q\right) = 0. \tag{4.11}$$

The solution of this equation is as follows:

$$r = q + Ce^{-\alpha t} \tag{4.12}$$

where C is a constant of integration. This equation means that r converges to q exponentially under the condition (4.10). Here, α determines the rate of the convergence. On the other hand, when (4.10) is not satisfied,

$$r = \begin{cases} q - F/K & \text{if } \dot{r} + \alpha\,(r - q) > 0 \\ q + F/K & \text{if } \dot{r} + \alpha\,(r - q) < 0. \end{cases} \tag{4.13}$$

This equation indicates that $q - r$ is constant in the kinetic friction state.

A discrete-time algorithm of the estimator (4.9) can be obtained in the similar way to obtain (3.10), and the algorithm is as follows:

$$r_k = q_k - \frac{F}{K}\mathrm{sat}\left(\frac{K(q_k - r_{k-1})}{F\,(1 + T\alpha)}\right) \tag{4.14a}$$

$$\hat{\tau}_k = K(q_k - r_k), \tag{4.14b}$$

and the algorithm is modified taking account of the direction-dependent Coulomb friction force and the rate-dependent friction, which are seen in (4.1) and Figure 4.3, as follows:

$$r_k = q_k - \frac{1}{K}\mathrm{gsat}\left(-F_n, \frac{K(q_k - r_{k-1})}{1 + T\alpha}, F_p\right) \tag{4.15a}$$

$$\hat{\tau}_k = K(q_k - r_k) + \Phi\left(\frac{r_k - r_{k-1}}{T}\right) \tag{4.15b}$$

where the function gsat is a generalized saturation function defined as (3.22) in Chapter 3. From the above derivation, the consequent algorithm is represented as follows:

$$\text{Function } \mathbf{algFE}(q_k, \alpha) \tag{4.16a}$$

$$\tau_m^* := \frac{K(q_k - r_{k-1})}{1 + T\alpha} \tag{4.16b}$$

$$r_k := q_k - \frac{1}{K}\mathrm{gsat}(-F_n, \tau_m^*, F_p) \tag{4.16c}$$

$$\tau_m := K(q_k - r_k) \tag{4.16d}$$

$$\hat{\tau} := \tau_m + \Phi((r_k - r_{k-1})/T) \tag{4.16e}$$

$$\text{Return } \hat{\tau}. \tag{4.16f}$$

4.6 Experiments

4.6.1 External force estimation

The proposed friction force estimator was tested in experiments of external force estimation using Setup A shown in Figure 4.1(a). In these experiments, the following three cases were compared:

- **CT**: simple Coulomb friction model with velocity threshold.
- **HA**: the friction force estimator (4.16) with $\alpha = 0$. The friction force estimator is a trivial extension of the conventional Hayward and Armstrong's friction model.
- **P**: the friction force estimator (4.16), i.e., the proposed method.

Here, the friction model used in **CT** is represented as follows:

$$\hat{\tau}(\dot{q}) = \begin{cases} F_p + \Phi(\dot{q}) & \text{if } \dot{q} > V \\ 0 & \text{if } |\dot{q}| \leq V \\ -F_n + \Phi(\dot{q}) & \text{if } \dot{q} < -V \end{cases} \tag{4.17}$$

where V is the velocity threshold of the dead zone to avoid non-zero estimated force around zero velocity. In this experiment, the threshold was set at $V = 0.01$ rad/s, which is corresponding to two counts of the encoder step per a sampling interval. Throughout all experiments in this chapter, the sampling interval was set as $T = 0.001$ s.

In this experiment, the experimenter grasped the grip of the end-effector and moved it without any actuator force. The estimator with each case was applied to the experimental data at the same time. Here, the compliance K of the friction model was set at $K =$

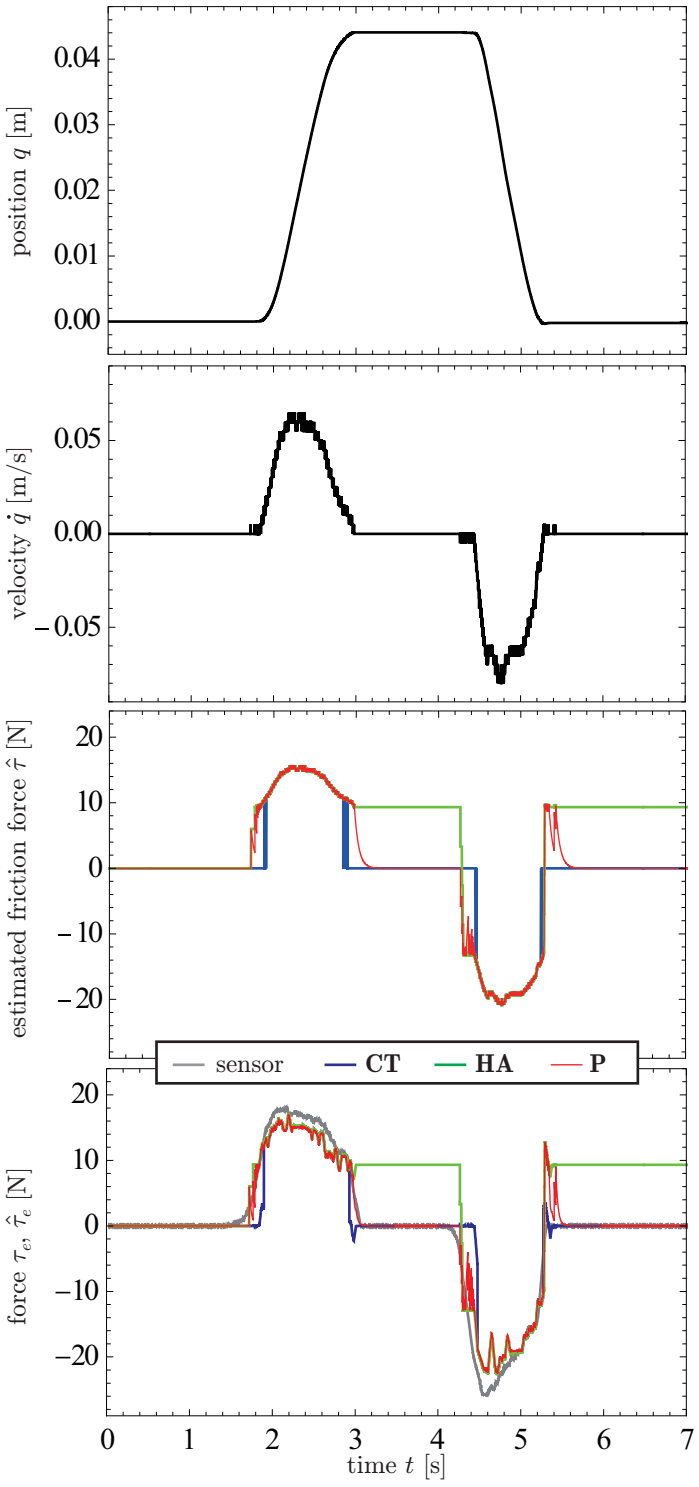

Figure 4.7: Experimental results of external force estimation, Setup A.

1.2×10^6 N/m, which is estimated as the compliance of the setup by an advance experiment. The inertia of the estimator was set at $\hat{M} = 10.0$ kg, which is close to the mass of the moving part of the setup. The constant α was selected so that the convergence of r_k to q_k is sufficiently quick, and the value was $\alpha = 20.0$ s^{-1}. The parameters G and H of the filter were set by the trade-off between the noise reduction and the delay caused by the filter, and the values were $G = 10.0$ and $H = 2.0$.

The result is shown in Figure 4.7. This figure shows that the curve in the estimator **P** is the closest to the curve of the force sensor. In the estimator **CT**, the response of the estimator was delayed due to the dead zone of the friction model (4.17). In the estimator **HA**, there is steady state error in the estimation after the motion stops. This result shows that the proposed estimator is advantageous to the estimator **CT** and **HA**.

4.6.2 Admittance control

In order to test the proposed friction force estimator, experiments of admittance control were performed with Setup A shown in Figure 4.1(a). In this experiment, the experimenter grasped the grip attached on the force sensor of the end-effector and moved it with the setup controlled by the admittance controller (4.6) with the three different estimators: **CT**, **HA** and **P**. The experimenter tried to move the end-effector as the position trajectory draws square wave-like form, being paced by a metronome with the frequency 0.667 Hz. Visible markers were attached to the frame of the setup as indicators of the locations between which the movement should be made. The parameters m and b of the virtual object were selected as the experimenter moves the end-effector with as small force as possible within the range in which oscillation does not occur, and the values were $m = 1.0$ m/s^2 and $b = 15.0$ m/s. The gains K_p and K_d of the position controller were set as high as possible to make the tracking performance high, and the values were $K_p = 1.0 \times 10^5$ N/m and $K_d = 1.0 \times 10^3$ Ns/m.

The experimental results are shown in Figure 4.8. This figure shows that the external force measured by the force sensor is smallest with the estimator **P**, while the position trajectories are similar to each other. This indicates that the device reacted to the external force more sensitively with the estimator **P**. In the case **CT**, larger force is required due to estimation errors of friction force caused by the velocity threshold. In the case **HA** also,

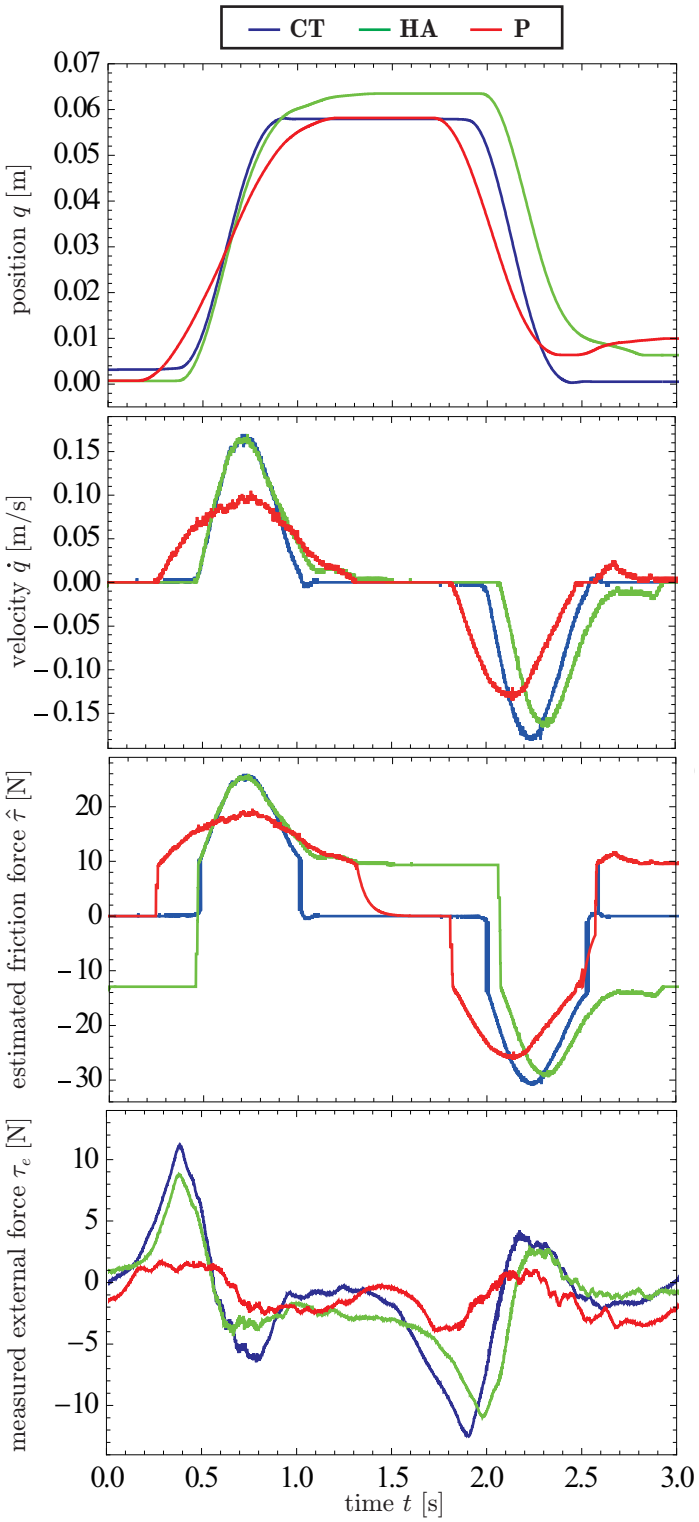

Figure 4.8: Experimental result of admittance control, Setup A.

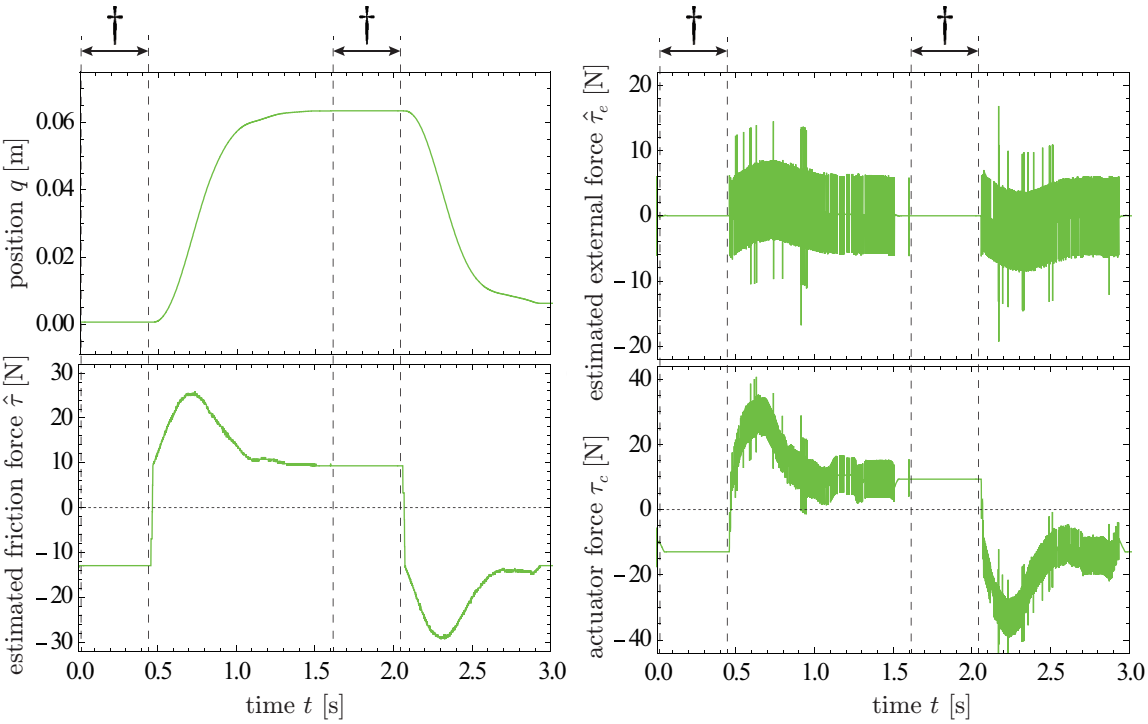

(a) Experimental results of admittance control with **C**, Setup A. The symbol † indicates periods of equilibrium.

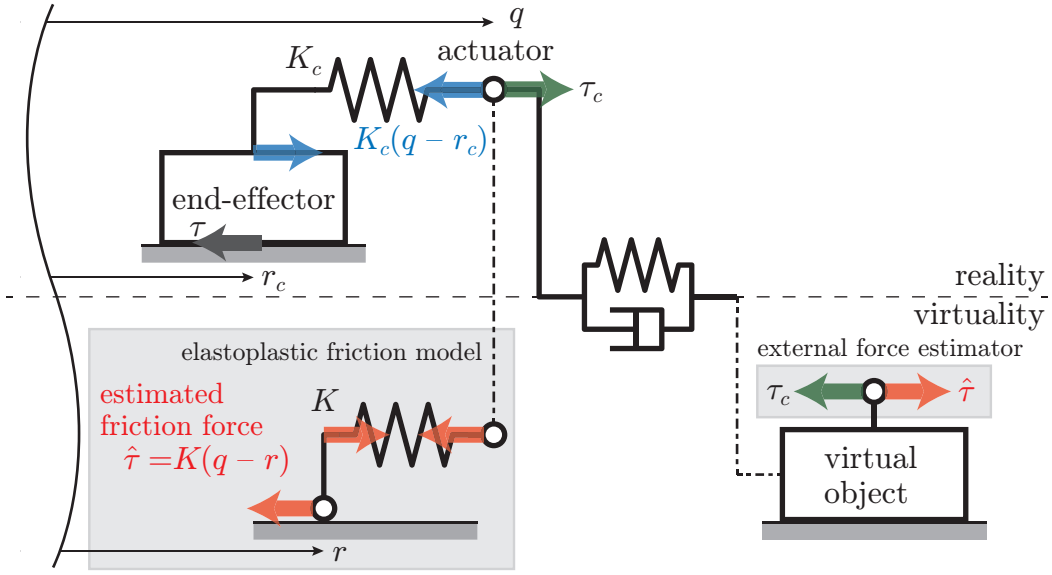

(b) Schematic illustration of equilibrium

Figure 4.9: Experimental results and schematic illustration that indicate equilibrium of an admittance controlled robotic system including an external force estimator with a conventional elastoplastic friction model. Here, the estimated external force $\hat{\tau}_e$ is zero but the actuator force τ_c is not zero.

larger force is required due to resistive force by an equilibrium of the admittance controlled system with the conventional elastoplastic friction model.

Figure 4.9 shows the experimental results with **HA** and the illustration of the equilibrium. In Figure 4.9(a), the estimated external force is almost zero in the static friction state (e.g., 1.5-2.0 s), while the estimated friction force and the actuator force are not zero. Considering this figure and (4.5), we can guess that the following equation is satisfied:

$$\hat{\tau}_e = \hat{\tau} - \tau_c \simeq 0 \tag{4.18}$$

with ignoring the acceleration $\ddot{\hat{q}}$, and the equilibrium is illustrated as Figure 4.9(b). Due to the zero value of external force estimation, the virtual object is in the static friction state. The actuator is also in the static friction state due to the balance between the actuator force and the actual friction force. Therefore, the system is in an equilibrium with producing non-zero actuator force, which hampers the sensitivity to the external force.

The experimental results have been investigated by another analysis as Figure 4.10. This figure shows comparisons between the force measured by the force sensor and the following criterion:

$$\hat{\tau}_a = m\ddot{\hat{q}} + b\dot{\hat{q}} \tag{4.19}$$

where $\dot{\hat{q}}$ and $\ddot{\hat{q}}$ are obtained from the position signal through the operator Q in Figure 4.4(b). This equation represents the estimated force acting on the virtual object. From Figure 4.10, we can see that the magnitude of the measured force is closer to the trajectories of the value of (4.19) with the estimator **P**, while we can see phase lags in (4.19) due to the filter in Q in all three conditions. This figure indicates that the higher accuracy in the estimator **P** made the property of the controlled system closer to that of the virtual object, of which the mass and the viscosity were set by the user. From these results, it can be said that the proposed friction force estimator is beneficial to the admittance control with the external force estimation.

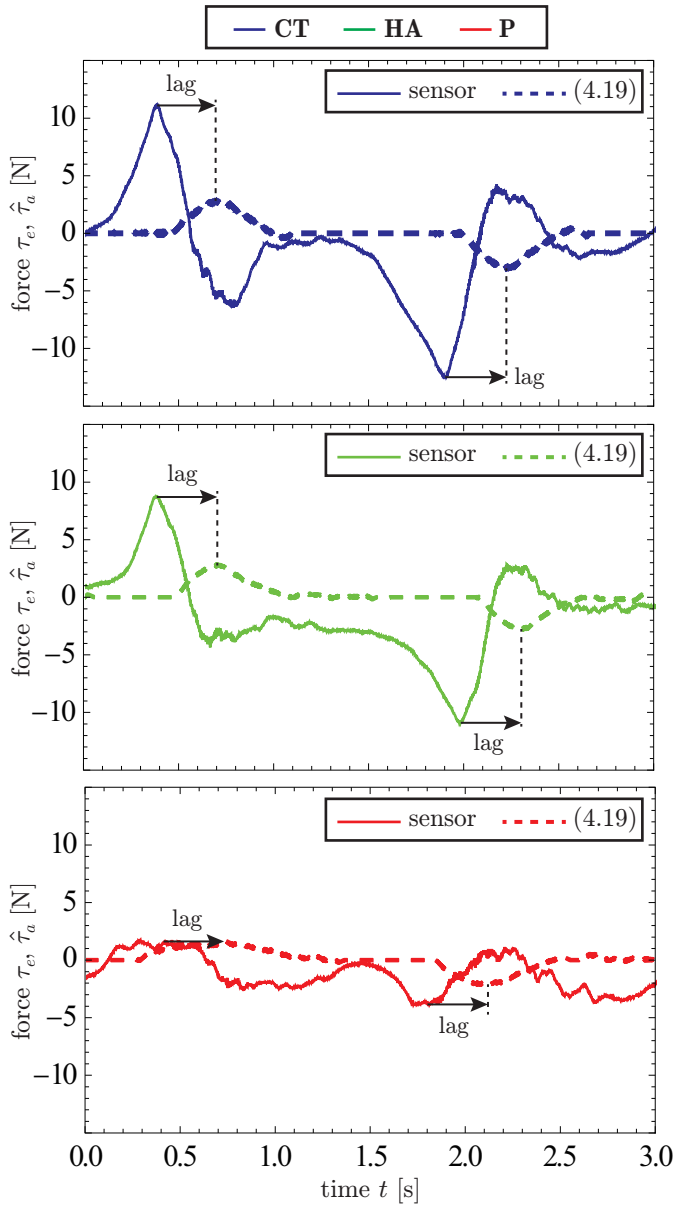

Figure 4.10: Comparison between the value measured by the force sensor and the value obtained from (4.19).

4.7 Further Improvement for Admittance Control

4.7.1 Algorithm

In a situation where the robot is admittance-controlled with external force estimation including the friction force estimator and is moved by human user's hand, slow convergence of the friction force estimation may cause one problem. The problem is that it may leads to fluctuation of the virtual object, which results in fluctuation of the admittance-controlled joint. Such behavior is problematic especially when the user intends to stop the motion. In such a situation, output of the friction force estimator should be weakened more quickly to suppress the fluctuation.

The decay rate of the friction force estimator is dominated by the constant α. In the static friction state, α should be the nominal value as used in Section 4.6.2 for appropriate estimation. On the other hand in the kinetic friction state, α value should be higher than the nominal one so that the estimated friction force decays more quickly and the motion of the virtual object is suppressed. From mentioned above, this chapter proposes a new algorithm adjusting the value of α online as follows:

$$\text{Function } \textbf{algFE2}(q_k) \tag{4.20a}$$
$$\quad \text{If } |(q_k - q_{k-1})/T| > V_W \tag{4.20b}$$
$$\quad\quad w_k := \max(w_{k-1} + R_W, 1) \tag{4.20c}$$
$$\quad \text{Else} \tag{4.20d}$$
$$\quad\quad w_k := \min(w_{k-1} - R_W, 0) \tag{4.20e}$$
$$\quad \text{Endif} \tag{4.20f}$$
$$\quad \alpha := (1 - w_k)\alpha_N + w_k\alpha_H \tag{4.20g}$$
$$\text{Return } \mathbf{algFE}(q_k, \alpha). \tag{4.20h}$$

Here, α_N is the nominal value of α, α_H is a value that is much higher than α_N. The constant V_W is a threshold velocity below which α is decreased and above which increased. This algorithm is intended to avoid the discontinuous change in the α value.

4.7.2 Experiments

For testing the new algorithm, experiments of the admittance control were performed using two devices, Setup A and Setup B shown in Figure 4.1. In these experiments, the experimenter grasped the grip of the end-effector and moved it from one point to another. For Setup B, the experiments were performed with respect to only the base joint (Joint 0) and the other joints were locked by local position controllers. These experiments compared the following three cases: $\alpha \equiv \alpha_N$ =20 s^{-1}, $\alpha \equiv \alpha_H$ =500 s^{-1}, and the proposed algorithm **algFE2** in (4.20) with α varying between α_N =20 s^{-1} and α_H =500 s^{-1}.

The rate of the transition of α was set at $R_W = 0.01$ for the two setups. The velocity thresholds were set at $V_W = 0.01$ for Setup A and $V_W = 0.001$ rad/s for Setup B. The other parameters for Setup A were set the same as in Section 4.6. For Setup B, the compliance of the friction estimator was set at $K = 50000$ Nm/rad, the magnitude of the Coulomb friction torque was set at $F = 6.85$ Nm, which is the intercept of Figure 4.3, and the parameters and the terms used in the system model such as $\boldsymbol{M}(\boldsymbol{q})$, $\boldsymbol{h}(\boldsymbol{q}, \dot{\boldsymbol{q}})$ and $\boldsymbol{g}(\boldsymbol{q})$ were determined through some experiments in advance.

The experimental results are shown in Figure 4.11. Here, the final displacements produced by the experimenter vary among conditions but it is only because he was given no visual indicator for the end point of the motion. We can see mostly the same features in Setup A and Setup B. In the case with the variable α, the force peaks were smallest, and after removing the external torque, the joint were in stationary state. In the case with nominal value α_N (20 s^{-1}), once the joints began to move, it was difficult to stop the joints by hand, although the force peaks were almost equivalent to the case with the variable α. In the case with high value α_H (500 s^{-1}), the force peaks were larger than the other cases, although it was easy to stop the joints.

The above results indicate that the proposed method achieved the both of the sensitivity of the joints to the external force and the suppression of the fluctuation. From this, it can be said that the proposed method enhances the performance of the admittance control with the external force estimation.

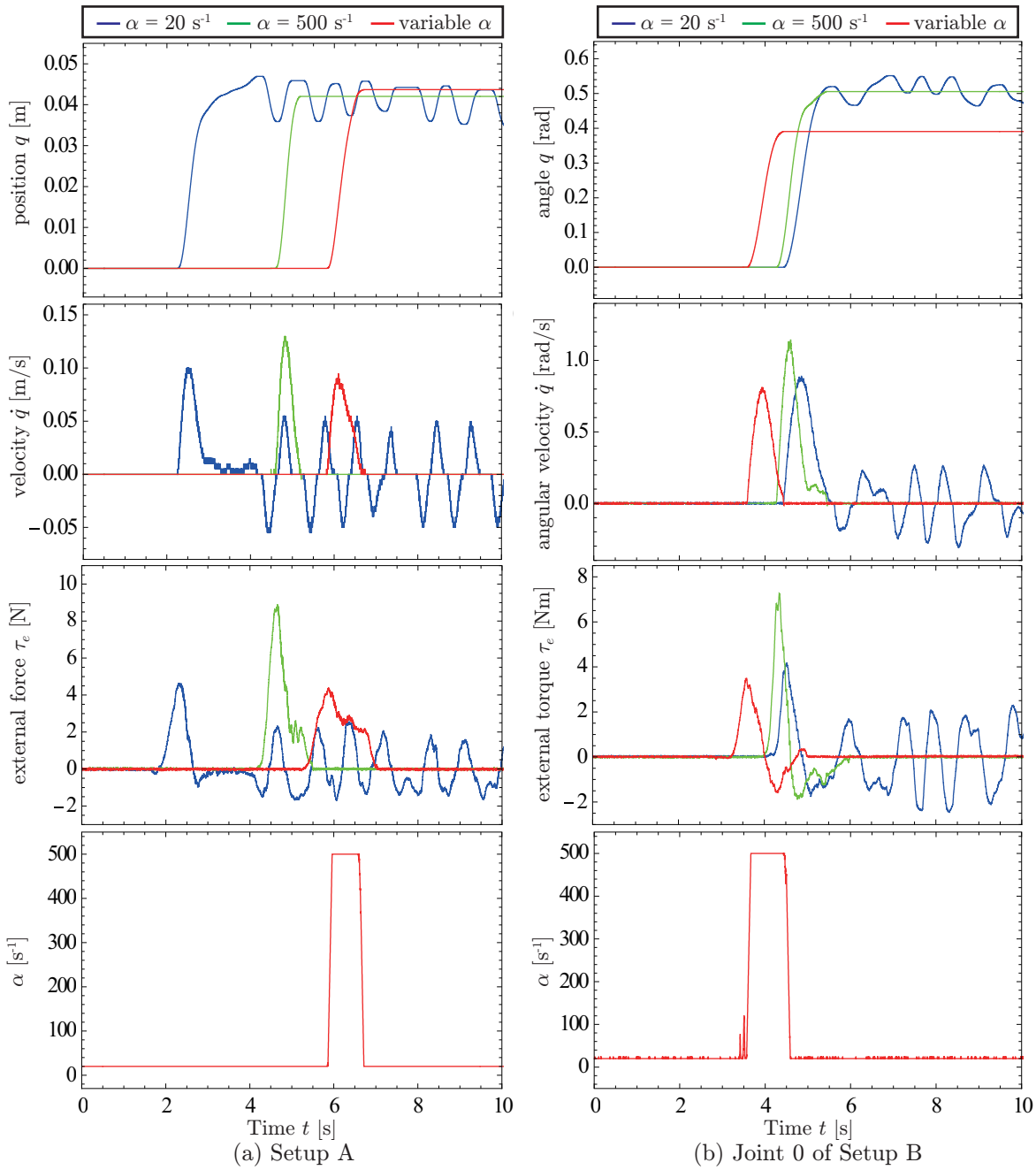

(a) Setup A (b) Joint 0 of Setup B

Figure 4.11: Experimental result of the admittance control with Setup A and Joint 0 of Setup B.

4.8 Summary

This chapter has presented a friction force estimator with an improved static friction behavior. The proposed friction force estimator is applied to an external force estimation method. The friction force estimator used in the external force estimation decays the output force in the static friction state, and enhances the accuracy of the external force estimation. Experimental validation with a linear actuator system shows that the proposed estimator causes smaller errors in the external force estimation, and that the estimator is advantageous in admittance control with the external force estimation. The friction force estimator has been further improved with an algorithm varying the decay rate.

Chapter 5

Conclusions and Future Work

5.1 Concluding remarks

Joint friction has been one of main factors that affect the control of robotic systems. This dissertation has presented some techniques for identification, compensation and estimation of joint friction of robotic systems.

Chapter 2 has presented an identification procedure for rate-dependent friction of robotic joints with limited motion ranges. The procedure is characterized by the following three features. (i) The rate dependency is represented by line sections connecting sampled velocity-force pairs, (ii) the robot is position-controlled to track desired trajectories that are some cycles of sinusoidal motion with different frequencies, and (iii) each velocity-force pair is sampled from one cycle of the motion with subtracting the effects of the gravity and the inertia. Chapter 3 and 4 use parameters and functions identified by this procedure. The time required for the identification of each joint in this dissertation was a few minutes. Even when the property of the joint friction varies by the environment such as temperature, a new feasible identification result is obtained by one more execution with a few minutes.

Chapter 3 has presented an elastoplastic friction compensator with improved static friction behavior. Here, the purpose of friction compensation is to remove the influence of friction from robotic joints and to realize high backdrivability. A conventional elastoplastic friction compensator produces non-zero output force in the static friction state and it

hampers the sensitivity to external force. The output force of the proposed compensator exponentially decays to zero so that the compensator does not hamper the sensitivity. It has been shown that backdrivability of robotic joints is enhanced by the new compensator. This chapter has also presented a further improved algorithm with varying decay rate for a situation where the joints are moved by human hand.

Chapter 4 has presented an elastoplastic friction force estimator for external force estimation. The new friction force estimator has a form similar to the friction compensator in Chapter 3 and decays its output force exponentially in the static friction state to improve the estimation accuracy. A further improved algorithm of friction force estimation has also been presented for the application to admittance control. This chapter has provided a new point of view for enhancing external force estimation, i.e. the enhancement by a method explicitly estimating friction force, while what have been studied so far are methods implicitly estimating friction force such as disturbance observers or sliding mode approaches.

Throughout dissertation, it has been discussed how to deal with joint friction of robotic systems. So far, researchers have proposed many theoretically sophisticated control schemes, but joint friction usually causes a huge gap between theory and practice. It can be expected that the methods developed in this dissertation will facilitate the mitigation of the gap. Enhancement of the control accuracy and stability will be indeed their potential effects. More importantly, the proposed techniques will contribute to better implementation of force control schemes. The force control of manipulators, which is still costly and cumbersome in the current industrial scenes, has vast area of potential applications if it is realized with a reasonable cost and a guaranteed safety. The techniques in this dissertation will contribute to robotic tasks involving physical interactions, such as polishing, assembly and cellular manufacturing. Moreover, gentle physical interaction that would be realized by friction compensation and external force estimation will benefit better human-robot interaction, which will be useful for, e.g., teaching-by-demonstration of industrial manipulators, and will also be beneficial in realizing non-industrial robotic devices such as those for power assisting and nursing care.

5.2 Future work

The proposed identification procedure assumes that the rate-dependent friction laws in joints are symmetric with respect to the origin in order to deal with the effect of gravity. Future study should clarify how to reduce the effect of gravity to identification results without employing the assumption.

Future work should also clarify some guidelines for the choice of the parameters in the new friction compensator and the new friction estimator. Theoretical properties of the compensator and the estimator, each of which is described as a differential algebraic inclusion in the continuous-time domain, is also an open problem.

References

[1] F. Al-Bender, V. Lampaert, and J. Swevers. The Generalized Maxwell-Slip Model: a Novel Model for Friction Simulation and Compensation. *IEEE Transactions on Automatic Control*, 50(11):1883–1887, 2005.

[2] B. Armstrong, D. Neevel, and T. Kusik. New Results in NPID Control: Tracking, Integral Control, Friction Compensation and Experimental Results. *IEEE Transactions on Control Systems Technology*, 9(2):399–406, 2001.

[3] B. Armstrong-Hélouvry. *Control of Machines With Friction*. Springer US, 1991.

[4] B. Armstrong-Hélouvry, P. Dupont, and C. Canudas de Wit. A Survey of Models, Analysis Tools and Compensation Methods for the Control of Machines With Friction. *Automatica*, 30(7):1083–1138, 1994.

[5] M. T. S. Aung, R. Kikuuwe, and M. Yamamoto. Friction Compensation of Geared Actuators With High Presliding Stiffness. *ASME Journal of Dynamic Systems, Measurement, and Control*, 137(1):011007, 2015.

[6] M. Boegli, T. De Laet, J. De Schutter, and J. Swevers. A Smoothed GMS Friction Model for Moving Horizon Friction State and Parameter Estimation. In *Proceedings of 2012 12th IEEE International Workshop on Advanced Motion Control*, pages 1–6, 2012.

[7] M. Boegli, T. De Laet, J. De Schutter, and Jan Swevers. A Smoothed GMS Friction Model suited for Gradient-Based Friction State Estimation. In *Proceedings of 2012 American Control Conference*, pages 2627–2632, 2012.

[8] B. Bona and M. Indri. Friction Compensation in Robotics: an Overview. In *Proceedings of the 44th IEEE Conference on Decision and Control, and the European Control Conference 2005*, pages 4360–4367, 2005.

[9] C. Canudas de Wit and P. Lischinsky. Adaptive Friction Compensation With Partially Known Dynamic Friction Model. *International Journal of Adaptive Control and Signal Processing*, 11:65–80, 1997.

[10] C. Canudas de Wit, H. Olsson, K. J. Åström, and P. Lischinsky. A New Model for Control of Systems With Friction. *IEEE Transactions on Automatic Control*, 40(3):419–425, 1995.

[11] W.-H. Chen. Disturbance Observer Based Control for Nonlinear Systems. *IEEE/ASME Transactions on Mechatronics*, 9(4):706–710, 2004.

[12] W.-H. Chen, D. J. Ballance, P. J. Gawthrop, and J. O'Reilly. A Nonlinear Disturbance Observer for Robotic Manipulators. *IEEE Transactions on Industrial Electronics*, 47(4):932–938, 2000.

[13] X. Chen, F. Fang, and X. Luo. A Friction Identification Approach Based on Dual-Relay Feedback Configuration With Application to an Inertially Stabilized Platform. *IEEE Transactions on Automatic Control*, 40(3):419–425, 1995.

[14] J. J. Choi, J. S. Kim, and S. I. Han. Pre-Sliding Friction Control Using the Sliding Mode Controller With Hysteresis Friction Compensator. *KSME International Journal*, 18(10):1755–1762, 2004.

[15] A. Colomé, D. Pardo, G. Alenyà, and C. Torras. External Force Estimation During Compliant Robot Manipulation. In *Proceedings of the 2013 IEEE International Conference on Robotics and Automation*, pages 3535–3540, 2013.

[16] P. R. Dahl. A Solid Friction Model. Technical Report TOR-0158(3107-18)-1, Aerospace Corporation, 1968.

[17] J. M. Daly and D. W. L. Wang. Time-Delayed Output Feedback Bilateral Teleoperation With Force Estimation for n-DOF Nonlinear Manipulators. *IEEE Transactions on Control Systems Technology*, 22(1):299–306, 2014.

[18] A. De Luca, A. Albu-Schäffer, S. Haddadin, and G. Hirzinger. Collision Detection and Safe Reaction With the DLR-III Lightweight Manipulator Arm. In *Proceedings of the 2006 IEEE/RSJ International Conference on Intelligent Robots and Systems*, pages 1623–1630, 2006.

[19] A. De Luca and R. Mattone. Sensorless Robot Collision Detection and Hybrid Force/Motion Control. In *Proceedings of the 2005 IEEE International Conference on Robotics and Automation*, pages 999–1004, 2005.

[20] R. Dhaouadi and F. H. Ghorbel. Modeling and Analysis of Nonlinear Stiffness, Hysteresis and Friction in Harmonic Drive Gears. *International Journal of Modeling and Simulation*, 28(3):329–336.

[21] P. Dupont, V. Hayward, B. Armstrong, and F. Altpeter. Single State Elastoplastic Friction Models. *IEEE Transactions on Automatic Control*, 47(5):787–792, 2002.

[22] M. S. Erden and T. Tomiyama. Human-Intent Detection and Physically Interactive Control of a Robot Without Force Sensors. *IEEE Transactions on Robotics*, 26(2):370–382, 2010.

[23] L. Freidovich, A. Robertsson, A. Shiriaev, and R. Johansson. Friction Compensation Based on LuGre Model. In *Proceedings of the 45th IEEE Conference on Decision and Control*, pages 3837–3842, 2006.

[24] E. Garcia, P. Gonzalez de Santos, and C. Canudas de Wit. Velocity Dependence in the Cyclic Friction Arising With Gears. *The International Journal of Robotics Research*, 21(9):761–771, 2002.

[25] M. Gautier and W. Khalil. Direct Calculation of Minimum Set of Inertial Parameters of Serial Robots. *IEEE Transactions on Robotics and Automation*, 6(3):368–373, 1990.

[26] M. Goldfarb and N. Celanovic. A Lumped Parameter Electromechanical Model for Describing the Nonlinear Behavior of Piezoelectric Actuators. *ASME Journal of Dynamic Systems, Measurement, and Control*, 119:478–485, 1997.

[27] S. Grami and H. Aissaoui. Filtering Approaches for Online Identification of GMS Friction Model. In *Proceedings of the 2011 IEEE EUROCON - International Conference on Computer as a Tool*, pages 1–4, 2011.

[28] S. Haddadin, A. Albu-Schäffer, A. De Luca, and G. Hirzinger. Collision Detection and Reaction: a Contribution to Safe Physical Human-Robot Interaction. In *Proceedings of the 2008 IEEE/RSJ International Conference on Intelligent Robots and Systems*, pages 3356–3363, 2008.

[29] T. Hägglund. A Friction Compensator for Pneumatic Control Valves. *Journal of Process Control*, 12:897–904, 2002.

[30] J. Han. From PID to Active Disturbance Rejection Control. *IEEE Transactions on Industrial Electronics*, 56(3):900–906, 2009.

[31] A. Harnoy, B. Friedland, and S. Cohn. Modeling and Measuring Friction Effects. *IEEE Control Systems*, 28(6):82–91, 2008.

[32] V. Hayward and B. Armstrong. A New Computational Model of Friction Applied to Haptic Rendering. In P. Corke and J. Trevelyan, editors, *Experimental Robotics VI*, volume 250 of *Lecture Notes in Control and Information Sciences*, pages 404–412. Springer-Verlag, 2000.

[33] N. Hogan. Impedance Control–an Approach to Manipulation. I–Theory. II–Implementation. III–Applications. *ASME Journal of Dynamic Systems, Measurement, and Contol*, 107:1–24.

[34] M. Indri, I. Lazzero, A. Antoniazza, and A. M. Bottero. Friction Modeling and Identification for Industrial Manipulators. In *Proceedings of 2013 IEEE 18th Conference on Emerging Technologies Factory Automation*, pages 1–8, 2013.

[35] J. Ishikawa, S. Tei, D. Hoshino, M. Izutsu, and N. Kamamichi. Friction Compensation Based on the LuGre Friction Model. In *Proceedings of the SICE Annual Conference 2010*, pages 9–12, 2010.

[36] W. D. Iwan. A Distributed-Element Model for Hysteresis and Its Steady-State Dynamic Response. *Journal of Applied Mechanics*, 33(4):893–900, 1966.

[37] M. Iwatani and R. Kikuuwe. An Identification Procedure for Rate-Dependent Friction Laws of Robotic Manipulator With Limited Motion Range. In *Proceedings of the 10th Asian Control Conference 2015*, pages 526–530, 2015.

[38] M. Iwatani and R. Kikuuwe. An Elastoplastic Friction Compensator With Improved Static Friction Behavior. In *Proceedings of SICE Annual Conference 2016*, pages 1091–1097, 2016.

[39] M. Iwatani and R. Kikuuwe. An Elastoplastic Friction Force Estimator and Its Application to External Force Estimation and Force-Sensorless Admittance Control. In *Proceedings of the 2016 IEEE/SICE International Symposium on System Integration*, pages 45–50, 2016.

[40] M. Iwatani and R. Kikuuwe. An Identification Procedure for Rate-Dependency of Friction in Robotic Joints With Limited Motion Ranges. *Mechatronics*, 36:36–44, 2016.

[41] M. Iwatani and R. Kikuuwe. An External Force Estimator Using Elastoplastic Friction Model With Improved Static Friction Behavior. In *Proceedings of 14th International Conference on Control, Automation, Robotics and Vision*, Tu42.6, 2016.

[42] M. Iwatani, R. Kikuuwe, and M. Yamamoto. Friction Compensation of Harmonic Drive Gearing Based on Parallel Viscoelasto-Plastic Friction Model. *Journal of Robotics Society of Japan*, 32(5):445–455, 2014 (in Japanese).

[43] Z. Jamaludin, H. Brussel, G. Pipeleers, and J. Swevers. Accurate Motion Control of xy High-Speed Linear Drives Using Friction Model Feedforward and Cutting Forces Estimation. *CIRP Annals–Manufacturing Technology*, 57(1):403–406, 2008.

[44] Z. Jamaludin, H. Brussel, and J. Swevers. Friction Compensation of an XY Feed Table Using Friction-Model-Based Feedforward and an Inverse-Model-Based Disturbance Observer. *IEEE Transactions on Industrial Electronics*, 56(10):3848–3853, 2009.

[45] C. F. Jenkin. A Mechanical Model Illustrating the Behaviour of Metals under Static and Alternating Loads. *Engineering*, 114:603, 1922.

[46] Furuta K. Sliding Mode Control of a Discrete System. *Systems and Control Letters*, 14(2):145–152, 1990.

[47] M. Kamezaki, H. Iwata, and S. Sugeno. Relative Accuracy Enhancement System Based on Internal Error Range Estimation for External Force Measurement in Construction Manipulator. In *Proceedings of IEEE/RSJ International Conference on Intelligent Robots and Systems*, pages 3734–3739, 2011.

[48] S. Katsura, Y. Matsumoto, and K. Ohnishi. Modeling of Force Sensing and Validation of Disturbance Observer for Force Control. *IEEE Transactions on Industrial Electronics*, 54(1):530–538, 2007.

[49] C. J. Kempf and S. Kobayashi. Disturbance Observer and Feedforward Design for a High-Speed Direct-Drive Positioning Table. *IEEE Transactions on Control Systems Technology*, 7(5):513–526, 1999.

[50] C. W. Kennedy and J. P. Desai. Modeling and Control of the Mitsubishi PA-10 Robot Arm Harmonic Drive System. *IEEE/ASME Transactions on Mechatronics*, 10(3):263–274, 2005.

[51] M. R. Kermani, R. V. Patel, and M. Moallem. Friction Identification and Compensation in Robotic Manipulators. *IEEE Transactions on Instrumentation and Measurement*, 56(6):2346–2353, 2007.

[52] R. Kikuuwe. A Sliding-Mode-Like Position Controller for Admittance Control With Bounded Actuator Force. *IEEE/ASME Transactions on Mechatronics*, 19(5):1489–1500.

[53] R. Kikuuwe, K. Kanaoka, T. Kumon, and M. Yamamoto. Phase-Lead Stabilization of Force-Projecting Master-Slave System With a New Sliding Mode Filter. *IEEE Transactions on Control Systems Technology*, 23(6):2182–2194, 2015.

[54] R. Kikuuwe, N. Takesue, and H. Fujimoto. A Control Framework to Generate Nonenergy-Storing Virtual Fixtures: Use of Simulated Plasticity. *IEEE Transactions on Robotics*, 24(4):781–793, 2008.

[55] R. Kikuuwe, N. Takesue, A. Sano, H. Mochiyama, and H. Fujimoto. Fixed-Step Friction Simulation: From Classical Coulomb Model To Modern Continuous Models. In *Proceedings of IEEE/RSJ International Conference on Intelligent Robots and Systems*, pages 1009–1016, 2005.

[56] R. Kikuuwe, N. Takesue, A. Sano, H. Mochiyama, and H. Fujimoto. Admittance and Impedance Representations of Friction Based On Implicit Euler Integration. *IEEE Transactions on Robotics*, 22(6):1176–1188, 2006.

[57] V. Lampaert, J. Swevers, and F. Al-Bender. Modification of the Leuven Integrated Friction Model Structure. *IEEE Transactions on Automatic Control*, 47(4):683–687, 2002.

[58] V. Lampaert, J. Swevers, and F. Al-Bender. A Generalized Maxwell-Slip Friction Model Appropriate for Control Purposes. In *Proceedings of the 2003 International Conference of Physics and Control*, pages 1170–1177, 2003.

[59] V. Lampaert, J. Swevers, and F. Al-Bender. Comparison of Model and Non-Model Based Friction Compensation Techniques in the Neighbourhood of Pre-Sliding Friction. In *Proceedings of the 2004 American Control Conference*, pages 1121–1126, 2004.

[60] H. S. Lee and M. Tomizuka. Robust Motion Controller Design for High-Accuracy Positioning Systems. *IEEE Transactions on Industrial Electronics*, 43(1):48–55, 1996.

[61] H. Li, K. Kawashima, K. Tadano, S. Ganguly, and S. Nakano. Achieving Haptic Perception in Forceps' Manipulator Using Pneumatic Artificial Muscle. *IEEE Transactions on Mechatronics*, 18(1):74–85, 2013.

[62] C.-S. Liu and H. Peng. Disturbance Observer Based Tracking Control. *ASME Journal of Dynamic Systems, Measurement, and Control*, 122:332–335, 1997.

[63] L. Ljung. Recursive Identification Algorithm. *Circuits, Systems and Signal Processing*, 21(1):57–68, 2002.

[64] Y. Maeda and M. Iwasaki. Improvement of Settling Performance by Initial Value Compensation Considering Rolling Friction Characteristic. In *Proceedings of IECON 2010-36th Annual Conference on IEEE Industrial Electronics Society*, pages 1902–1907, 2010.

[65] Y. Maeda and M. Iwasaki. Initial Friction Compensation Using Rheology-Based Rolling Friction Model in Fast and Precise Positioning. *IEEE Transactions on Industrial Electronics*, 60(9):3865–3876, 2013.

[66] M. Mahvash and A. M. Okamura. Friction Compensation for Enhancing Transparency of a Teleoperator With Compliant Transmission. *IEEE Transactions on Robotics*, 23(6):1240–1246, 2007.

[67] N. Marcassus, P. O. Vandanjon, A. Janot, and M. Gautier. Minimal Resolution Needed for an Accurate Parametric Identification Application to an Industrial Robot Arm. In *Proceedings of the 2007 IEEE/RSJ International Conference on Intelligent Robots and Systems*, pages 2455–2460, 2007.

[68] N. Marcassus, P. O. Vandanjon, A. Janot, and M. Gautier. Experimental Identification of the Inverse Dynamic Model: Minimal Encoder Resolution Needed Application to an Industrial Robot Arm and a Haptic Interface. *Robot Manipulators*, pages 313–330, 2008.

[69] T. Murakami, F. Yu, and K. Ohnishi. Torque Sensorless Control in Multidegree-of-Freedom Manipulator. *IEEE Transactions on Industrial Electronics*, 40(2):259–265, 1993.

[70] M. Nakao, K. Ohnishi, and K. Miyachi. A Robust Decentralized Joint Control Based on Interference Estimation. In *Proceedings of the 1987 IEEE International Conference on Robotics and Automation*, pages 326–331, 1987.

[71] A. Nikoobin and R. Haghight. Lyapunov-Based Nonlinear Disturbance Observer for Serial n-Link Robot Manipulators. *Journal of Intelligent and Robotic Systems*, 55(2):135–153, 2009.

[72] Y. Ohba, M. Sazawa, K. Ohishi, T. Asai, K. Majima, and Y. Yoshizawa. Sensorless Force Control for Injection Molding Machine Using Reaction Torque Observer Considering Torsion Phenomenon. *IEEE Transactions on Industrial Electronics*, 56(8):2955–2960, 2009.

[73] K. Ohnishi, M. Shibata, and T. Murakami. Motion Control for Advanced Mechatronics. *IEEE/ASME Transactions on Mechatronics*, 1(1):56–67, 1996.

[74] H. Olsson, K. J. Åström, C. Canudas de Wit, M. Gäfvert, and P. Lischinsky. Friction Models and Friction Compensation. *European Journal of Control*, 4(3):176–195, 1998.

[75] A. A. Pervozvanski and C. Canudas de Wit. Asymptotic Analysis of the Dither Elect in Systems With Friction. *Automatica*, 38:105–113, 2002.

[76] L. D. Phong, J. Choi, and S. Kang. External Force Estimation Using Joint Torque Sensors for a Robot Manipulator. In *Proceedings of the 2012 IEEE International Conference on Robotics and Automation*, pages 4507–4512, 2012.

[77] D. D. Rizos and S. D. Fassois. Friction Identification Based Upon the LuGre and Maxwell Slip Models. *IEEE Transactions on Control Systems Technology*, 17(1), 2009.

[78] D. D. Rizos and S. D. Fassois. A-Posteriori Identifiability of the Maxwell Slip Model of Hysteresis. *International Federation of Automatic Control Proceedings Volumes*, 44(1):10788–10793, 2011. 18th International federation of Automatic Control World Congress.

[79] M. Ruderman. Discrete-Time Series Identification of Sliding Dynamic Friction in Industrial Robotic Joints. In *Proceedings of the 2013 IEEE/RSJ International Conference on Intelligent Robots and Systems*, pages 5809–5814, 2013.

[80] W. J. Rugh. Design of Nonlinear PID Controllers. *AICbE Journal*, 33(10):1738 – 1742, 1987.

[81] E. Schrijver and J. van Dijk. Disturbance Observers for Rigid Mechanical Systems: Equivalence, Stability, and Design. *ASME Journal of Dynamic Systems, Measurement, and Control*, 124(4):539–548, 2002.

[82] H. Seraji. A New Class of Nonlinear PID Controllers for Robotic Applications. *Journal of Robotic Systems*, 15(3):161–181, 1998.

[83] L. Sidhom, M. T. Pham, F. Thévenoux, and M. Gautier. Identification of a Robot Manipulator Based on an Adaptive Higher Order Sliding Modes Differentiator. In *Proceedings of the 2010 IEEE/ASME International Conference on Advanced Intelligent Mechatronics*, pages 1093–1098, 2010.

[84] Z. Situm, D. Pavkovic, and B. Novakovic. Servo Pneumatic Position Control Using Fuzzy PID Gain Scheduling. *ASME Journal of Dynamic Systems, Measurement, and Control*, 126(2):376–387, 2004.

[85] J. J. Slotine and S. S. Sastry. Tracking Control of Non-Linear Systems Using Sliding Surfaces, With Application to Robot Manipulators. *International Journal of Control*, 38(2):465–492, 1983.

[86] A. Stolt, A. Robertsson, and R. Johansson. Robotic Force Estimation using Dithering to Decrease the Low Velocity Friction Uncertainties. In *Proceedings of the 2015 IEEE International Conference on Robotics and Automation*, pages 3896–3902, 2015.

[87] J. Swevers, F. Al-Bender, C. G. Ganseman, and T. Prajogo. An Integrated Friction Model Structure With Improved Presliding Behavior for Accurate Friction Compensation. *IEEE Transactions on Automatic Control*, 45(4):675–686, 2000.

[88] Y. Tan and I. Kanellakopoulos. Adaptive Nonlinear Friction Compensation with Parametric Uncertainties. In *Proceedings of the American Control Conference*, pages 2511–2515, 1999.

[89] T. Tjahjowidodo, F. Al-Bender, and H. Brussel. Nonlinear Modeling and Identification of Torsional Behavior in Harmonic Drives. In *Proceedings of International Conference on Noise and Vibration Engineering*, pages 2785–2796, 2006.

[90] T. Tjahjowidodo, F. Al-Bender, and H. Van Brussel. Friction Identification and Compensation in a DC Motor. *IFAC Proceedings Volumes*, 38(1):554 – 559, 2005.

[91] T. Tjahjowidodo, F. Al-Bender, H. Van Brussel, and W. Symens. Friction Characterization and Compensation in Electro-Mechanical Systems. *Journal of Sound and Vibration*, 308(3):632–646, 2007.

[92] V. I. Utkin. Survey Paper: Variable Structure Systems with Sliding Modes. *IEEE Transactions on Automatic Control*, 22(2):212–222, 1977.

[93] V. I. Utkin. Sliding Mode Control Design Principles and Applications to Electric Drives. *IEEE Transactions on Industrial Electronics*, 40(1):23–36, 1993.

[94] M. Vakil, R. Fotouhi, and P. N. Nikiforuk. Energy-Based Approach for Friction Identification of Robotic Joints. *Mechatronics*, 21(3):614–624, 2011.

[95] N. D. Vuong and M. H. Jr Ang. Dynamic Model Identification for Industrial Robots. *Acta Polytechnica Hungarica*, 6(5):51–68, 2009.

[96] X. Xiong, R. Kikuuwe, and M. Yamamoto. A Multistate Friction Model Described by Continuous Differential Equations. *Tribology Letters*, 51(3):513–523, 2013.

[97] X. Xiong, R. Kikuuwe, and M. Yamamoto. A Differential-Algebraic Method to Approximate Nonsmooth Mechanical Systems by Ordinary Differential Equations. *Journal of Applied Mathematics*, 2013, Article, 320276, 2013.

[98] T. Yang. A New Control Framework of Electric Power Steering System Based on Admittance Control. *IEEE Transactions on Control Systems Technology*, 23(2):762–769.

[99] W. Yu, J. Rosen, and X. Li. PID Admittance Control for an Upper Limb Exoskeleton. In *Proceedings of the 2011 American Control Conference*, pages 1124–1129, 2011.

[100] C. Zhou, Z. Li, J. Castano, H. Dallali, N. G. Tsagarakis, and D. G. Caldwell. A Passivity Based Compliance Stabilizer for Humanoid Robots. In *Proceedings of the 2014 International Conference on Robotics and Automation*, pages 1487–1492, 2014.

[101] S. Zschäck, S. Buchner, A. Amthor, and C. Ament. Maxwell Slip based Adaptive Friction Compensation in High Precision Applications. In *Proceedings of the 38th Annual Conference on IEEE Industrial Electronics Society*, pages 2331–2336, 2012.